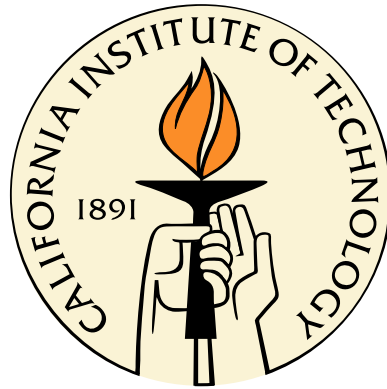


# Brownian Thermal Noise in Interferometric Gravitational Wave Detectors and Single Photon Optomechanics

Thesis by  
Ting Hong

In Partial Fulfillment of the Requirements  
for the Degree of  
Doctor of Philosophy



California Institute of Technology  
Pasadena, California

2013  
(Defended July 16, 2012)



# Acknowledgements

First and most, I would like to thank Yanbei Chen, my advisor, for supporting and encouraging me on my research, for suggesting projects and guiding me with the problems, and for his kind and consistent help in both my work and life.

I would also like to thank Rana Adhikari, for his advice and suggestion on the details of my research, for teaching me how to write a scientific paper, for many helpful discussions, for giving support on my thermal noise projects, and for giving up his travel to Vienna for my defense.

I would like to thank all the people who collaborated and assisted me in my research; they are Huan Yang, Haixing Miao, Eric Gustafson, John Miller, and Hiro Yamamoto.

Keith Schwab and Julia Greer have my thanks for serving on my thesis committee.

I am grateful to JoAnn Boyd, Shirley Hampton, and Christy Jenstad for helping me with administrative matters.

Finally, I would like to thank my family and friends. Without their support, and encouragement, I'd never have made it this far. I thank my husband, Guoqiang, for all the love and care I enjoyed, for being with me through the good times and bad times.

The research presented in this thesis was supported by NSF Grant PHY-0555406, PHY-1068881 and CAREER Grant PHY-0956189, the David and Barbara Groce Startup Fund, and the David and Barbara Research Assistantship at the California Institute of Technology. Funding has also been provided by the Institute for Quantum Information and Matter, an NSF Physics Frontiers Center with support of the Gordon and Betty Moore Foundation.

# Abstract

The Laser Interferometric Gravitational-Wave Observatory (LIGO) is designed to detect the Gravitational Waves (GW) predicted by Albert Einstein's general theory of relativity. The advanced LIGO project is ongoing an upgrade to increase the detection sensitivity by more than a factor of 10, which will make the events detection a routine occurrence. In addition to using higher power lasers, heavier test mass, and better isolation systems, several new designs and techniques are proposed in the long-term upgrade, such as modifying the optics configuration to reduce the quantum noise, active noise cancellation of the Newtonian noise, optimizing the coating structure, and employing non-Gaussian laser beams etc.

In the first part of my thesis (Chapters 2 and 3), I apply statistical mechanics and elastostatics to the LIGO coated mirrors, and study the thermal fluctuations that dominate advanced LIGO's most sensitive frequency band from 40 Hz to 200 Hz.

In particular, in Chapter 2, I study the so-called coating Brownian noise, fluctuations of mirrors coated with multiple layers of dielectrics due to internal friction. Assuming coating materials to be isotropic and homogeneous, I calculate the cross spectra of Brownian fluctuations in the bulk and shear strains of the coating layers, as well as fluctuations in the height of the coating-substrate interface. The additional phase shifting and back-scattering caused by photo elastic effects are also considered for the first time.

In Chapter 3, I study whether it is realistic to adopt higher-order Laguerre-Gauss modes in LIGO, in order to mitigate the effect of mirror thermal noise. We investigate the effect on the detector's contrast defect caused by the mode degeneracy. With both analytical calculation and numerical simulation, we show that with this approach, the detector's susceptibility to mirror figure errors is reduced greatly compared to using the nondegenerate modes, therefore making it unacceptable for LIGO requirements.

For the future GW detectors, with much lower noises and higher sensitivity, this might be used to investigate the quantum behaviors of macroscopic mechanical objects. In recent years the linear optomechanical systems with cavity modes coupling to a mechanical oscillator have been studied extensively. In the second part of my thesis (Chapter 4), I study the interaction between a single photon and a high-finesse cavity with a movable mirror, in the so-called strong coupling regime, where

the recoil of the photon can cause significant change in the momentum of the mirror. The results are applied to analyze the case with a Fabry-Perot cavity. We also present that with engineering the photon wave function, it is possible to prepare the oscillator into an arbitrary quantum state.

# Contents

<b>Acknowledgements</b>	<b>iii</b>
<b>Abstract</b>	<b>iv</b>
<b>List of Figures</b>	<b>x</b>
<b>List of Tables</b>	<b>xv</b>
<b>1 Introduction</b>	<b>1</b>
1.1 Laser Interferometer Gravitational-Wave Detectors: An Overview . . . . .	2
1.1.1 Gravitational Waves . . . . .	2
1.1.2 Laser Interferometry . . . . .	3
1.1.3 Major Noise Sources of LIGO . . . . .	4
1.2 Coating Thermal Noise in Interferometric Gravitational Wave Detectors . . . . .	6
1.2.1 Fluctuation Dissipation Theorem . . . . .	6
1.2.2 Multilayer Dielectric Coatings . . . . .	7
1.3 Light Beams and Mirror Shapes in Interferometric Gravitational Wave Detectors . . . . .	8
1.3.1 Dependence of Thermal Noise on Beam Profile: Scaling Laws . . . . .	8
1.3.2 Why Modified Beams? . . . . .	9
1.3.3 Mode Degeneracy . . . . .	10
1.4 Quantum Dynamics of Optomechanical Systems . . . . .	10
1.4.1 Linear Systems . . . . .	11
1.4.2 The Simplest Nonlinear Systems . . . . .	12
Bibliography . . . . .	14
<b>2 Coating Thermal Noise in Interferometric Gravitational Wave Detectors</b>	<b>15</b>
2.1 Introduction . . . . .	16
2.2 Components of the Coating Thermal Noise . . . . .	18
2.2.1 Complex Reflectivity . . . . .	18
2.2.2 Thermal Phase and Amplitude Noise . . . . .	20

2.2.3	Fluctuations $\delta\phi_j$ and $\delta r_p$ . . . . .	21
2.2.4	Mode Selection for Phase Noise . . . . .	24
2.2.5	Conversion of Amplitude Noise into Displacement . . . . .	25
2.3	Thermal Noise Assuming No Light Penetration into the Coating . . . . .	26
2.3.1	The Fluctuation-Dissipation Theorem . . . . .	26
2.3.2	Mechanical Energy Dissipations in Elastic Media . . . . .	27
2.3.3	Thermal Noise of a Mirror Coated with one Thin Layer . . . . .	28
2.3.4	Discussions on the Correlation Structure of Thermal Noise . . . . .	31
2.4	Cross Spectra of Thermal Noise Components . . . . .	31
2.4.1	Coating-Thickness Fluctuations . . . . .	32
2.4.2	Fluctuations of Coating-Substrate Interface and Their Correlations with Coating Thickness . . . . .	34
2.4.3	The Anatomy of Coating Thermal Noise . . . . .	36
2.4.4	Full Formula for Thermal Noise . . . . .	39
2.5	Effect of Light Penetration into the Coating . . . . .	40
2.5.1	Optics of Multilayer Coatings . . . . .	40
2.5.2	Levels of Light Penetration in advanced LIGO ETM Coatings . . . . .	42
2.5.3	Thermal Noise Contributions from Different Layers . . . . .	44
2.6	Dependence of Thermal Noise on Material Parameters . . . . .	44
2.6.1	Dependence on Ratios Between Loss Angles . . . . .	45
2.6.2	Dependence on Young's moduli and Poisson's ratios . . . . .	46
2.6.3	Dependence on Photoelastic Coefficients . . . . .	48
2.6.4	Optimization of Coating Structure . . . . .	49
2.7	Measurements of Loss Angles . . . . .	51
2.7.1	Bending Modes of a Thin Rectangular Plate . . . . .	51
2.7.2	Torsional Modes of a Coated Hollow Cylinder . . . . .	53
2.8	Conclusions . . . . .	54
2.9	Appendix A: Fluctuations of the Complex Reflectivity due to Refractive index fluctuations . . . . .	57
2.9.1	The Photoelastic Effect . . . . .	57
2.9.2	Fluctuations in an Infinitesimally Thin Layer . . . . .	58
2.9.3	The Entire Coating Stack . . . . .	60
2.9.4	Unimportance of Transverse Fluctuations . . . . .	61
2.10	Appendix B: Elastic Deformations in The Coating . . . . .	62
2.11	Appendix C: Definition of loss angle . . . . .	65
2.12	Appendix D: Advanced LIGO Style Coating [25] . . . . .	66

Bibliography . . . . .	67
<b>3 Effects of Mirror Aberrations on Laguerre-Gaussian Beams in Interferometric Gravitational-Wave Detectors</b>	<b>70</b>
3.1 Introduction . . . . .	71
3.2 Mirror Figure Errors . . . . .	72
3.3 Degenerate Perturbation-Theory Analysis . . . . .	73
3.3.1 Laguerre-Gauss modes . . . . .	73
3.3.2 Application of Degenerate Perturbation Theory to the Perturbed Fabry-Perot Cavity . . . . .	76
3.3.2.1 Mode Splitting . . . . .	76
3.3.2.2 The Modal Input-Output Equation . . . . .	78
3.4 Contrast Defect . . . . .	79
3.4.1 Analytic Calculation . . . . .	81
3.4.2 Numerical Calculation . . . . .	82
3.5 Contrast Defect Improvement . . . . .	85
3.5.1 Better Polishing . . . . .	85
3.5.2 Arm Cavity Detuning . . . . .	86
3.5.3 Mirror Corrections . . . . .	86
3.5.4 Mode Healing . . . . .	87
3.6 Conclusions . . . . .	87
3.7 Appendix: Contrast Defect . . . . .	88
Bibliography . . . . .	91
<b>4 Open Quantum Dynamics of Single-photon Optomechanical Devices</b>	<b>93</b>
4.1 Introduction . . . . .	94
4.2 A Single Cavity with one Movable Mirror . . . . .	96
4.2.1 The Hamiltonian . . . . .	96
4.2.2 Structure of the Hilbert Space . . . . .	98
4.2.3 Initial, Final States and Photodetection . . . . .	99
4.2.4 Evolution of the Photon-mirror Quantum State . . . . .	100
4.2.4.1 Free Evolution . . . . .	101
4.2.4.2 Junction Condition . . . . .	102
4.2.4.3 Coupled Evolution . . . . .	102
4.2.4.4 Full Evolution . . . . .	104
4.3 Single-photon Interferometer: Visibility . . . . .	104
4.3.1 The Configuration . . . . .	105

4.3.2	The Role of the Beamsplitter and a Decomposition of Field Degrees of Freedom	105
4.3.3	Interactions Between Light and Cavities . . . . .	106
4.3.4	The Final State . . . . .	108
4.3.5	Examples . . . . .	109
4.4	Conditional Quantum-state Preparation . . . . .	111
4.4.1	The Configuration . . . . .	111
4.4.2	Preparation of a Single Displaced-Fock State . . . . .	113
4.4.3	Preparation of an Arbitrary State . . . . .	117
4.5	Practical Considerations . . . . .	120
4.6	Conclusions . . . . .	121
	Bibliography . . . . .	122

# List of Figures

1.1	The noise curve for aLIGO baseline design . . . . .	4
1.2	The amplitude profiles of Gaussian (black), Mesa (blue), Conical (purple) and LG <sub>3,3</sub> (red) modes . . . . .	10
2.1	Schematic plot of a mirror coated with multiple dielectric layers. Shown here are the various fluctuations that contribute to coating noise, i.e., fluctuations in the amplitude and phase of the returning light caused by fluctuations in the geometry (e.g., layer thickness $\delta l_j$ , layer area stretch $(\delta A/A)_j$ and interface height $z_s$ ) of the coating-substrate configuration and in refractive indices $[\delta n_j(x, y, z)]$ of the layers. . . . .	17
2.2	Illustrations of forces applied onto various interfaces within the coating. Each of Layers I and III in the coating are assumed to be uniform (but they might each contain a different kind of material); region II denotes the entire gap between them, which may well contain many different dielectric layers. A pair of force distribution $f_1$ ( $f_3$ ) in opposite directions is exerted on opposite sides of Layer I (III), while $f_s$ is exerted on the coating-substrate interface. The three distributions may well have different profiles (as also illustrated in the figure). . . . .	34
2.3	Illustration of the correlations between coating thickness $\delta l_j$ and the height of the coating-substrate interface, $z_s$ . On the left, for a bulk deformation: when a coating element is expanding, its expansion along the $x$ - $y$ plane lifts the coating-substrate interface upwards, causing additional motion of the coating-air interface correlated to that caused by the increase in coating thickness. On the right, a a particular shear mode: when a coating element is expanding, its contraction along the $x$ - $y$ plan pushes the coating-substrate interface downwards, causing addition motion of the coating-air interface anticorrelated to that caused by the increase in coating thickness. . . . .	37
2.4	Two basic transformations involved in solving for optical fields in a multilayer coating	40
2.5	Real (solid curves) and imaginary (dashed curves) parts of $\partial \log \rho / \partial \phi_j$ (upper panel) and $\partial \log \rho / \partial r_j$ (lower panel), for conventional (red curve) and Advanced LIGO (blue curve) coatings. [Note that $\text{Re}(\partial \log \rho / \partial \phi_j) = 0$ for conventional coating.] . . . . .	41

2.6	Light penetration into the first 10 layers of a 38-layer coating (left panel for conventional coating and right panel for Advanced LIGO coating). We plot the non-photoelastic part of $\mathcal{T}_j$ in black solid curves, the photoelastic part of $\mathcal{T}_j^s$ in long-dashed red curves, as well as $\mathcal{T}_j^s$ (scaled by rms value of $\delta l_j^c$ with respect to the rms value of $\delta l_j$ , shown in short-dashed blue curves) and $T_j^s$ (scaled by rms value of $\delta l_j^s$ , shown in dotted purple curves). These plots indicate that for both structures, light penetration is restricted within the first 10 layers. . . . .	42
2.7	A break-down of thermal noise contributions from silica (upper panels) and tantala (lower panels) layers, from bulk (left panels) and shear (right panels) losses. Blue curves correspond to $\beta = -1$ , black $\beta = 0$ and red $\beta = 1$ . Dashed curves indicate results calculated without including back-scattering effects. . . . .	43
2.8	(color online) Variations in thermal noise contributions when $\phi_B/\phi_S$ is varied. Contributions from tantala layers is shown in blue, those from silica layers are shown in red. The total thermal noise is in black. Bulk contributions are shown in dotted curves, while shear contributions are shown in dashed curves. . . . .	45
2.9	(color online) Variations in total noise when $\phi_B/\phi_S$ is varied: (solid) total noise, (dotted) total bulk noise, (dashed) total shear noise. The red (blue) curve corresponds to only varying $\phi_B/\phi_S$ for tantala (silica). With $\phi_B/\phi_S$ of tantala or silica varying from 0.2 to 5, the change in total noise is 58.1% and 10.6%, respectively. . . . .	46
2.10	Thermal noise contribution from tantala, as its Young's modulus deviates from baseline value, for $\phi_B/\phi_S=5$ (blue dashed), 2 (blue dotted), 1 (black solid), 1/2 (red dotted), and 1/5 (red dashed) . . . . .	47
2.11	Thermal noise contribution from tantala, as its Poisson's ratio deviates from baseline value, for $\phi_B/\phi_S=5$ (blue dashed), 2 (blue dotted), 1 (black solid), 1/2 (red dotted), and 1/5 (red dashed) . . . . .	47
2.12	Fractional change in the contribution to thermal noise from all silica layers (left panel) and all tantala layers (right panel), due to bulk (blue) and shear (red) loss. Dashed lines indicate results calculated without including back-scattering terms. . . . .	48
2.13	Optimized thermal noise versus transmissivity at 1064 nm, for a coating of 38 (red), 40 (blue), and 42 (purple) layers . . . . .	50
2.14	Rectangular shaped thin plate ( $a \times b \times c$ ) with thin coating (thickness $d$ ): $c \ll a, b; d \ll c$ . The transverse vibration mode is considered in this case. . . . .	52
2.15	Thin cylindrical shell with thin coating outside. The first torsional eigenmodes of such a shell can be used to measure the shear loss angle of the coating. . . . .	53

2.16	Light propagation across a thin layer (thickness of $\Delta l$ ) with fluctuating refractive index (from a uniform $n_2$ to an average of $n_2 + \delta n_2$ within this thin layer). The propagation matrix corresponding to this structure is given by Eq. (2.122). . . . .	59
2.17	Sample with single layer coating. Force is applied perpendicular to the air/coating interface. . . . .	63
2.18	Solid cube with two pairs of forces applied on the side: $f \ll F$ . . . . .	66
3.1	Power spectral densities of uncoated mirror surface roughness. The dashed lines are the measured spectra of three Advanced LIGO arm cavity mirrors. A model approximating these spectra (black trace, see (3.2)) was created to generate the random maps used in our work. . . . .	72
3.2	Surface figure (in nm) of a typical generated phase map with Piston, tilt, power and astigmatism terms subtracted . . . . .	74
3.3	Normalized intensity distribution of the LG <sub>3,3</sub> mode at the mirror position ( $\omega_0 = 0.021$ m, $z = 1997.25$ m) . . . . .	75
3.4	Fabry-Perot cavity with a perturbation $\delta h(x, y)$ on the end mirror . . . . .	76
3.5	Frequency shift of LG modes introduced as a result of realistic mirror perturbations . . . . .	78
3.6	Intensity distributions of the total field reflected from an arm cavity whose end mirror was perturbed by the reference map. These distributions were calculated independently via two different techniques. Top—Analytic method described in Section 3.3.2. Bottom—FFT-based numerical simulation (see Section 3.4.2) . . . . .	80
3.7	Contrast defect with the ETM of one cavity perturbed by rescaling the reference phase map: Solid red is from the analytical calculation, blue marker is from the FFT calculation. . . . .	82
3.8	Ratio, numerical/analytical, of single-cavity contrast defects calculated with the end mirror perturbed by a 0.3 nm RMS figure error . . . . .	83
3.9	Interferometer contrast defect as a function of test mass surface roughness (all 4 mirrors are perturbed with random phase map at the same level of RMS). Solid markers report mean values of numerical results with the corresponding shaded regions illustrating one standard deviation (see 3.4.2), which is roughly four times higher than the trace in Fig. 3.7 . . . . .	84
3.10	Analytic calculation with different conditions for reducing the contrast defect: solid curve is the original contrast defect; dashed line has corrective rings added to the phase map; dotted curve is with detuned injecting laser frequency . . . . .	85
3.11	Frequency shift in LG modes introduced by adding rings to the reference phase map. . . . .	87

4.1 (color online) A schematics showing the single-photon interferometer. The external single photon excites the cavity mode which in turn interacts with the movable end mirror via radiation pressure. This is adapted from Fig. 1 of Ref. [7] with small modifications. . . . . 95

4.2 (color online) A schematics showing a single-photon interferometer with Fabry-Perot cavity and a movable mirror. The displacement of the mirror-endowed mechanical oscillator  $y$  is parametrically coupled to the cavity mode  $a$ , which has an eigenfrequency  $\omega_0$  with  $y = 0$ . The cavity mode in turn couples to the ingoing continuous filed  $c(x)$  and outgoing continuous field  $d(x)$ . . . . . 96

4.3 (color online) Three regions of the  $t$ - $x$  plane and the free evolutions of  $|\psi_1\rangle$ . In region (i), the photon has not yet entered the cavity; the joint quantum state of the system is a simple free evolution of the initial quantum state, specified on  $t = 0, x < 0$  (green horizontal half line), see Eq. (4.25). In region (ii), the photon and the oscillator evolve freely after propagates after the photon emerges from the cavity; the joint wave function depends on the wave function along  $x = 0, t > 0$  (green vertical half line). The red line dividing regions (i) and (ii) corresponds to the  $\delta$ -function in Eq. (4.23), which embodies the interaction between the outside photon and the in-cavity photon. Region (iii) is causally irrelevant to our experiment. . . . . 101

4.4 We illustrate the fields entering and exiting each of the four ports of the interferometer. We use arrows to define the positive sense of the coordinate used to label their locations. For each of them  $x = 0$  corresponds to the location of the beamsplitter. . . . . 107

4.5 (color online) (left) Probability density and (right) fringe visibility for the photon to come out with different  $\beta$ : (Top-to-bottom: first row,  $\beta = 0.5$ ; second row,  $\beta = 1.2$ ; third row,  $\beta = 2$ ). For each  $\beta$ , three different values of  $\Gamma$  are considered for comparison:  $\Gamma = 0.2$  (red dotted), 1(blue dashed), 2(black solid). All the calculation assume  $\gamma = 1, \omega_m = 1$ . For probability density plot, the upper line of the same color is the maximum value of the probability density, the lower one is the minimum value. . . . . 112

4.6 (color online) The sample device which uses single photon to prepare mechanical oscillator quantum state. Here the the detuning phase for the mirror on the east arm is adjusted such that the promptly reflected photon will come out from west port, with 0 probability coming out from south port. . . . . 113

4.7 A sketch of the phase-space trajectory of the mechanical oscillator. The Wigner function of the initial state  $|0\rangle$  is represented by the shaded disk, the dot marked with  $\beta$  on the real axis is the new equilibrium position of the oscillator when the photon is in the cavity, while the dashed circle is the trajectory of the oscillator's Wigner function when the photon is inside the cavity. Detection of the out-going photon at  $t = 2n\pi/\omega_m$  corresponds to superimposing all mechanical-oscillator quantum states along the dashed trajectory, weighted by the photon's wave function. . . . . 114

4.8 Probability for obtaining displaced Fock states  $|\tilde{1}\rangle$  (red solid),  $|\tilde{2}\rangle$  (blue dashed),  $|\tilde{5}\rangle$  (magenta dotted) and  $|\tilde{10}\rangle$  (black dash-dotted), a range of  $\beta$  and minimum state overlap of  $1 - \epsilon$ . Vertical gridlines are draw for  $\beta = 1, \sqrt{2}, \sqrt{5}$  and  $\sqrt{10}$ ; these are the locations where maxima of  $P_{1,2,5,10}$  are reached. . . . . 116

4.9 Minimum success probability for states in Hilbert spaces  $\mathcal{H}_{1,2,\dots,7}$  (solid curves with markers), together with success probability for producing single displaced Fock states,  $P_{0,1,2,\dots,7}$  (dashed curves without markers). Fidelity is fixed at 10%. Note that  $P_0$  would become greater than 1 at low values of  $\beta$ —but in this case our approximation in obtaining  $\Delta\tau$  breaks down. . . . . 118

# List of Tables

2.1	Transfer functions from bulk and shear noise fields to layer thickness and surface height	37
2.2	Baseline material parameters . . . . .	41
2.3	Results of coating-structure optimization. We list optimized coating structures for $T_{1064} = 5$ ppm and $T_{532} = 5\%$ , for three target values of $\phi_B/\phi_S$ while fixing the measured effective loss angle $\phi_D$ <a href="#">[[Eq. (2.56)]]</a> and other baseline material parameters [Table 2.2]. Thickness of coating layers are given in units of wavelength (for 1064 nm light). For each optimized coating structure, thermal noise is calculated separately for all three values of $\phi_B/\phi_S$ , and given in units of $10^{-21}$ m/ $\sqrt{\text{Hz}}$ (thermal noise for the target $\phi_B/\phi_S$ is given in boldface, and boldface numbers should be the minimum within its column); thermal noise spectra of the 38-layer $\lambda/4$ stack assuming the target $\phi_B/\phi_S$ are also listed for comparison. . . . .	50
2.4	Example parameters of a thin, uniformly coated cylindrical shell ( $\text{SiO}_2$ ) . . . . .	54
2.5	Levels of thermal noise uncertainty caused by parameter uncertainties . . . . .	55
2.6	Comparison of thermal noise spectral density (assuming $\phi_B = \phi_S$ and evaluated at 200 Hz, in units of $10^{-21}$ m/ $\sqrt{\text{Hz}}$ ) between different works . . . . .	57
2.7	Structure of an advanced LIGO-like coating optimized jointly for dichroic operation and thermal noise. Thickness of each layer is given in units of wavelength (for light with vacuum-wavelength of 1064 nm) are listed here for the 38 layers. Note that $l_{1,3,5,\dots}$ are $\text{SiO}_2$ layers, while $l_{2,4,6,\dots}$ are $\text{Ta}_2\text{O}_5$ layers. . . . .	67
3.1	Beam shapes that have been considered for use in gravitational-wave detectors, mirror shapes that support them and their thermal-noise suppression factors (in power) for advanced LIGO parameters (cavity length $L = 4$ km, mirror radius of 17 cm) . . . . .	71
3.2	Suppression factors of thermal noise (in power spectral density) for LG modes with a fixed clipping loss of 1 ppm . . . . .	75
3.3	Cavity parameters used in the numerical simulations. All three resonators had a length of 3994.5 m. The mesa radii of curvature refer to the fiducial sphere from which the mesa correction profile is subtracted (cf. <a href="#">[11]</a> ). Cavity g factor is not well defined for mesa modes. . . . .	83

# Chapter 1

## Introduction

General relativity describes gravity in terms of the interaction between matter and space-time geometry. The existence of gravitational waves is an important feature of general relativity. Observations of relativistic binary pulsars has indirectly confirmed the existence of gravitational waves.

The effort to directly detect gravitational waves started in the 1960s when Joseph Weber constructed resonant bars and attempted to read out the excitations of the bars by gravitational-wave bursts [1]. Since the last decade, an array of kilometer scale, laser interferometer gravitational-wave detectors have been constructed, and put into operation. Among these are the detectors of the Laser Interferometer Gravitational-wave Observatory (LIGO) [2], VIRGO [3], GEO600 [4] and TAMA300 [5]. A first round of observations at the initial detectors' design sensitivity has been performed since 2007, but no detections has been made. The absence of detections is compatible with astrophysical estimates of event rate at the strength accessible to these detectors. As planned, LIGO and VIRGO are now being upgraded into second-generation detectors, while the KAGRA detector in Japan are being constructed [6]. These second-generation detectors will have a sensitivity roughly 10 times the initial detectors—and will thereby reach out 10 times farther into the universe. While the second-generation detectors are being constructed, third-generation detectors are being planned. Those detectors will have even better sensitivity, and therefore make possible a fruitful observational program of gravitational-wave astronomy. In Chapters 2 and 3 of this thesis, I will discuss coating Brownian noise, the dominant noise source of advanced LIGO in its most sensitive band of 40 Hz – 200 Hz. In Chapter 2, we assumes coating materials to be homogeneous and isotropic, and calculates the level of bulk and shear fluctuations, accounting for light penetration into the coating layers; Chapter 3 evaluates the feasibility of using a higher-order Laguerre-Gauss optical mode to mitigate thermal noise.

Future gravitational-wave detectors will be operating very close to the so-called Standard Quantum Limit, where quantum fluctuations in the motions of the mirrors will be at the same level of the interferometer's sensitivity; these detectors can be used to explore macroscopic quantum mechanics. In Chapter 4 of this thesis, I will study quantum mechanical interaction between light and matter

by calculating the effect of a single photon on the movable mirror of a Fabry-Perot cavity.

The rest of the introductory chapter is devoted to providing some background for Chapters 2, 3, and 4. Sec. 1.2 gives an overview of the LIGO interferometer, including a simple description of the detection mechanism and a brief review of the main noise sources. In Sec. 1.3, I focus especially on the thermal noise of the detectors. Sec. 1.4 gives a description of a simple linear and nonlinear quantum system.

## 1.1 Laser Interferometer Gravitational-Wave Detectors: An Overview

### 1.1.1 Gravitational Waves

Gravitational waves are propagations of space-time perturbations. One way to describe these waves on a Minkowski background is to write the space-time metric as

$$g_{\mu\nu} = \eta_{\mu\nu} + h_{\mu\nu} \quad (1.1)$$

namely the Minkowski metric plus a perturbation. The trace-reversed perturbation,

$$\bar{h}_{\mu\nu} = h_{\mu\nu} - \frac{1}{2}\eta_{\mu\nu}h \quad (1.2)$$

when setting the Lorenz gauge,

$$\partial^\nu \bar{h}_{\mu\nu} = 0 \quad (1.3)$$

satisfies a wave equation:

$$\square \bar{h}_{\nu\sigma} = -\frac{16\pi G}{c^4} T_{\nu\sigma} \quad (1.4)$$

where  $T_{\nu\sigma}$  is the momentum tensor of matter energy.

For a single plane wave, it is often convenient to adopt the so-called transverse traceless (or TT) gauge. Assuming the wave to propagate along the  $z$  direction, then the only non-vanishing metric perturbations in the TT gauge reads

$$h_{xx} = -h_{yy} = h_+(t - z), \quad h_{xy} = h_{yx} = h_\times(t - z). \quad (1.5)$$

One way to appreciate the physical effect of the GW is to consider geodesic motion in the TT gauge. It is not difficult to show that masses staying at constant coordinate locations are in fact following geodesics. However, the *proper spatial distance* between these objects oscillate due to GW.

Another point of view applies better to a detector whose size is much less compared with the

reduced wavelength of the gravitational wave. In this case, we can go into the Local Lorenz Frame of the detector, in which test masses moving at low speeds are influenced by a tidal gravitational field,

$$M\ddot{x}_k = \frac{M}{2}h_{jk}^{\text{TT}}x^j + F_k \quad (1.6)$$

where  $F_k$  is the nongravitational force acting on the test mass. Light propagation, on the other hand, is not affected. In this way, the problem of gravitational-wave detection simplifies into one of measuring a weak classical tidal force field. In a gravitational-wave detector, the force  $F_k$  acting on the test mass contains a conservative force that provides confinement of the test mass near its zero-point position as well as an inevitable fluctuating force. The latter will be a source of noise.

For free mass (as is approximately the case for LIGO mirrors, which are hung as low-frequency pendulums), we can easily integrate Eq. (1.6) and obtain

$$\delta x_k = \frac{h_{jk}^{\text{TT}}}{2}x^k. \quad (1.7)$$

This means an array of free masses will be distorted by a strain field with size comparable to  $h$ .

### 1.1.2 Laser Interferometry

LIGO detectors are Michelson interferometers with Fabry-Perot cavities in the arms (which are orthogonal to each other and equal in length). Because the arm length  $L$  is 4 km, and the detection band is up to several kHz, Eq. (1.6) is a good approximation. If we consider LIGO arms to be along the  $x$  and  $y$  axes of a Cartesian coordinate system, and consider an incoming gravitational wave along the  $z$  direction, with  $+$  polarization, then  $h_+$  should be proportional to the differential cavity length. More precisely, in absence of noise, we have

$$h_+ = \frac{(q_1 - q_2) - (q_3 - q_4)}{L} \quad (1.8)$$

where  $q_1$  is the displacement of the center of mass of the end mirror of the  $x$  arm,  $q_2$  is the displacement of the center of mass of the input mirror of the  $x$  arm, while  $q_{3,4}$  are the end- and input-mirror displacements of the  $y$  arm.

In reality, LIGO's noises arise from: (i) in presence of force noise, the combination on the right-hand side of (1.8) is not only driven by  $h_+$ , but also by force noise, and (ii) that combination cannot be sensed without extra noise. Nevertheless, LIGO detectors are very sensitive devices; initial LIGO detectors achieved a strain noise spectrum of  $\sqrt{S_h} \approx 2 \times 10^{-23}/\sqrt{\text{Hz}}$  at around 150 Hz, while the second-generation detectors will reach  $\sqrt{S_h} \approx 2 \times 10^{-24}/\sqrt{\text{Hz}}$  [7].

### 1.1.3 Major Noise Sources of LIGO

In general, for ground-based detectors, the most important limitations to sensitivity result from quantum noise, thermal noise, seismic noise and Newtonian noise. Fig. 1.1 shows the anticipated noise curve of the advanced LIGO detector with an input laser power of 125W [8]. Here we review each of these important noises briefly.

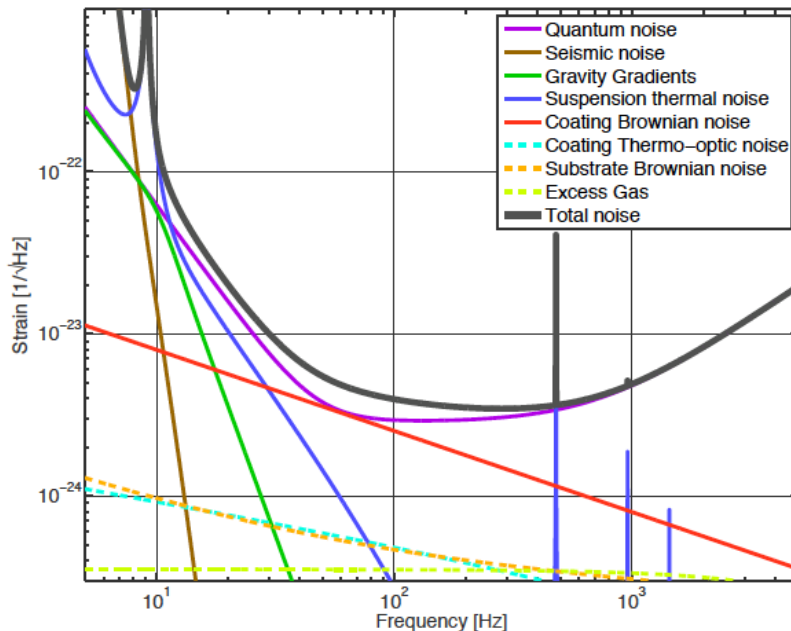


Figure 1.1: The noise curve for aLIGO baseline design

1. *Quantum noise*. This noise arises from quantum fluctuations of light and in the center of mass motion of the test masses, driven by radiation pressure. This is the noise that survives even when we idealize the interferometer to the simplest level. This noise can often be divided into two components, with opposite scaling with laser power.

The first component of quantum noise is *shot noise*, which arises from the discreteness of photons, which limits the resolution power of interferometry. For a simple Michelson interferometer without arm cavities driven by a laser with power  $I_0$  and angular frequency  $\omega_0$ , the shot noise spectrum for displacement measurement is then

$$S_{\text{sh}}^x = \frac{\hbar c^2}{I_0 \omega_0}. \quad (1.9)$$

Here  $x$  is the differential arm length.

The second component is *radiation-pressure noise*, which is caused by the fluctuating radiation pressure noise acting on the mirrors. The fluctuation in radiation pressure is in turn caused

by photon number fluctuations in the arm. For free test masses,

$$S_{\text{rp}}^x \approx \frac{I\omega_0}{c^2} \frac{\hbar}{m^2\Omega^4}. \quad (1.10)$$

When a Fabry-Perot cavity (on resonance with the carrier light) with input-mirror power transmissivity  $T$  is inserted into the arms, photons stay in the cavity for a longer time before leaving, and the interferometer’s sensitivity is boosted by a factor of  $2/T$  in frequencies below the cavity bandwidth. The insertion of Fabry-Perot cavities also causes *higher* radiation-pressure noise—photons staying in the cavity for a longer time causes noisily radiation-pressure force on the mirror to be coherent during the cavity storage time, leading to a higher level of fluctuations at frequencies below the cavity bandwidth. More specifically, with cavities, we have the total quantum noise as

$$S^h(\Omega) = \left[ \frac{1}{\kappa} + \kappa \right] \frac{4\hbar}{m\Omega^2 L^2}. \quad (1.11)$$

Here  $\kappa = \frac{8I_0\omega_0}{mL^2\Omega^2(\Omega^2+\gamma^2)}$ ,  $\gamma$  is the cavity bandwidth.

Note that the shot noise and the radiation-pressure noise have exactly the opposite scalings with laser power, as well as cavity improvement. If we assume the two types of noise to be independent, the sum of these noises in power will lead to a total noise spectrum that is always greater than the so-called standard quantum limit (SQL) [9]. For Fabry-Perot Michelson (with four movable mirrors with identical mass  $m$ ), the SQL for  $h$  is given by

$$S_{\text{SQL}}^h = \frac{8\hbar}{m\Omega^2 L^2}. \quad (1.12)$$

The SQL can also be derived from various models of continuous position measurement; it characterizes the level of sensitivity at which quantum measurement induced back action becomes an important factor in determining a device’s sensitivity.

In initial LIGO, radiation-pressure noise is much lower than suspension and internal thermal noise. For advanced LIGO, with increased laser power and lower level of other noise sources (see below), quantum noise is an important noise source in the entire observation frequency band of 10 Hz to several kHz.

2. *Internal thermal noise.* This noise arises from thermal fluctuations in the position of the mirror surface sensed by the reflected light—with respect to the center of mass of the mirror [10, 11]. This noise can be further classified as either arising from *isothermal* fluctuations of elastic stress distributions in the test mass (Brownian noise), or from shape (thermoelastic noise) and refractive index (thermo-optical noise) fluctuations driven by temperature fluctuations [12].

According to the fluctuation-dissipation theorem, each thermal noise corresponds to a mechanism of damping. The Brownian noise corresponds to internal frictions in the mirror coating and substrate, while thermo-optical noise corresponds to damping due to heat transfer. The internal thermal noise dominates advanced LIGO's noise budget from 40 Hz to 240 Hz.

3. *Suspension thermal noise.* This is the noisy motion of the center of mass of the test mass driven by thermal fluctuations in the suspension system. This corresponds to energy loss in the bulk and surface of the suspension wire, as well as the attachment points. This noise dominates advanced LIGO's noise spectrum at low frequencies (below  $\sim 40$  Hz) [13, 14].
4. *Seismic noise.* This refers to the noisy motion of the mirrors driven by ground vibration, after being filtered through the multistage seismic isolation system. This dominates initial LIGO's noise below 40 Hz (serving as a low-frequency cutoff of sensitivity), and advanced LIGO's noise below 10 Hz.
5. *Newtonian noise.* This noise, also called the *gravity gradient noise*, is the mirror motion driven by fluctuations in Newtonian gravitational field, which are in turn caused by mass density fluctuations (usually seismic in nature) in vicinity to the test mass. Unlike the (vibrational) seismic noise, the Newtonian noise cannot be shielded by isolation systems, although it might be suppressed by monitoring ground motion and predicting the gravity field caused by that motion [15].

## 1.2 Coating Thermal Noise in Interferometric Gravitational Wave Detectors

### 1.2.1 Fluctuation Dissipation Theorem

The near equilibrium thermal noise spectrum could be related to the dissipation of the system by fluctuation dissipation theorem [16]. Yuri Levin developed an approach to calculate the spectral density of the internal thermal noise [17, 18]: For a generalized coordinate  $q$  (usually an average longitudinal position of points on the mirror surface), we *imagine* applying an oscillating generalized force force, conjugate to  $q$ , with single frequency  $f$  and amplitude  $F$ , onto the mirror and calculate the dissipation rate  $W_{\text{diss}}$  during this process. The thermal noise spectrum of the mirror, in absence of that driving, is then given by:

$$S_q = \frac{2k_B T}{\pi^2 f^2} \frac{W_{\text{diss}}}{F^2}. \quad (1.13)$$

Here  $k_B$  is the Boltzmann's constant, and  $T$  is the temperature. If this  $q$  is associated with one of the four LIGO mirrors, then this converts into a strain noise of

$$S_h = (4/L^2)S_q. \quad (1.14)$$

### 1.2.2 Multilayer Dielectric Coatings

Due to the low internal friction and wide commercial availability, fused silica is used in the current LIGO optics, such as test mass, beam splitter, etc. In order to use the fused silica as the mirrors in arm cavities, multilayer dielectric coatings must be applied on the surface to achieve high reflectivity. In all present operating GW interferometric detectors, the quarter-wave length (QWL) multi layer coatings, specifically, alternating  $\text{Ta}_2\text{O}_5$  and  $\text{SiO}_2$  layers are used to satisfy the designed reflectivity requirements without inducing high optical loss. Although the QWL coating could achieve the largest reflectivity with fixed number of coating layers, it does not necessarily yield the minimum thermal noise for a prescribed reflectivity, therefore it is not *optimal*.

A considerable amount of scientific research has been done, both theoretically and experimentally, to optimize the coating structure, such as using the repeating  $\text{Ta}_2\text{O}_5$  and  $\text{SiO}_2$  doublets with different ratio or even non-periodic configurations [19], injecting different dopants in the materials and replacing the end mirror with an anti-resonant cavity, [20] etc.

In Chapter 2, we calculated the coating Brownian noise by separately considering each type of fluctuations: thickness and transverse deformations of the coating layers, fluctuations in the height of the coating-substrate interface, and fluctuations in refractive index, which causes both an additional phase shift and back-scattering for light propagating within the layers. For each type of fluctuation, we have incoherent contributions arising separately from shear and bulk losses of the coating material—which we have assumed to be homogeneous and isotropic.

Compared with previous studies [10], we have newly introduced the two possible loss angles, and the fact that they may not be equal to each other; we have also treated more rigorously effects associated with light penetration into the coating layers. What we have found is that in the case of advanced LIGO mirrors, because the most lossy coating material,  $\text{Ta}_2\text{O}_5$ , has a much higher Young's modulus compared with the substrate, the combination of the two loss angles that affect the Brownian thermal noise is very similar to the one already being measured by existing experimental programs, which measures the loss induced to a oscillating coated cantilever by a coating that is compression free across its thickness. Nevertheless, information about both loss angles would be important for a precise prediction of the coating Brownian noise, as well as in situations where the balance of Young's moduli is different. We have also found that light penetration effects in coating Brownian noise is not very significant, and this seems to preclude tricks that try to cancel coating Brownian noise by carefully arranging coating thickness.

## 1.3 Light Beams and Mirror Shapes in Interferometric Gravitational Wave Detectors

### 1.3.1 Dependence of Thermal Noise on Beam Profile: Scaling Laws

The reason why LIGO can measure mirror displacement with an accuracy much higher than the position uncertainty of individual atoms is because of averaging—fluctuations of mirror surface are often incoherent at different transverse locations on the mirror surface across the beam, while the center-of-mass motion induces a coherent displacement at different transverse locations. As it turns out, when the mirror is approximated as a half-infinite space, and coating a thin infinite plate (with thickness much less than the beam spot size), a simple set of *scaling laws*, which relate thermal noise spectrum to the intensity profile of the beam (when the thermal, optical and mechanical properties of the mirror remain constant), was developed by Lovelace, O’Shaughnessy and Vytachanin, [21, 22]. The scaling law states:

$$S_{\text{th}} \propto \int_0^\infty dk k^n \tilde{p}^2(k). \quad (1.15)$$

Here the index  $n$  is 0 for Brownian noise, 1 for both coating Brownian and thermoelastic noise, and 2 for substrate thermoelastic noise. Here  $\tilde{p}(k)$  is the 2-D Fourier transform of the intensity profile of the beam  $p(r)$  over the mirror surface, with

$$\tilde{p}(k) = \int_0^\infty dr r J_0(kr) p(r) \quad (1.16)$$

$$p(r) = \int_0^\infty dk k J_0(kr) \tilde{p}(k). \quad (1.17)$$

$J_0(kr)$  is the  $0^{\text{th}}$  Bessel function of the first kind. These definitions have assumed the beam to be axisymmetric.

As we focus on the thermal noise of coating, we find the more specific form of

$$S_{\text{coating}} \propto \int_0^\infty dr r p^2(r) \quad (1.18)$$

This in fact corresponds to having uncorrelated fluctuations at different locations across the mirror surface; the interpretation is that because coating is very thin (in particular, when compared with the beam spot size), thermal fluctuations are all local. We can rewrite Eq. (1.18) into

$$S_{\text{coating}} \propto \frac{\int_0^\infty dr r p^2(r)}{\left[\int_0^\infty dr r p(r)\right]^2}. \quad (1.19)$$

such that this new formula does not depend on the normalization of the intensity profile  $p(r)$ . If we were to choose  $p(r)$  to be approximately uniform within an area  $\mathcal{A}$ , and approximately zero outside

this area, then we will have coating thermal noise inversely proportional to the area:

$$S_{\text{coating}} \propto \frac{1}{\mathcal{A}}. \quad (1.20)$$

This means, even for  $p(r)$  that is non-uniform, we can still regard the coating noise as inversely proportional to the *effective area* of the beam.

The scaling laws, strictly speaking, only apply to infinite mirrors with large beam spot and very thin coating. However, for the dimensions of test masses and optical beams used in advanced LIGO, Lovelace has estimated that the scaling laws cause errors not more than 15%.

### 1.3.2 Why Modified Beams?

According to the scaling law, the power spectrum of the coating Brownian noise is inversely proportional to the effective area of the optical mode. Currently the baseline design of LIGO is using Gaussian beams in the arm cavities, supported with spherical mirrors. The Gaussian beam is easy to generate and could meet the strict requirement of low diffraction loss in the measurements, while its steeply sloping profile also generates more thermal fluctuations on the mirror surface, therefore lead to significant thermal noise. According to this, Thorne and O’Shaughnessy proposed the flat-topped beams supported by nearly-at Mexican-hat-shaped mirrors, so called mesa beams, which have more uniform amplitude profiles (see Fig. 1.2) with steep edges. They also proposed a way to construct this kind of beam in experiments by superimposing a series of narrow Gaussian beams. With this beam, the thermal fluctuations throughout the mirror surface would be more average, therefore give lower thermal noise than the conventional Gaussian beams. Theoretical calculation shows it could reduce the thermal noise of coatings by a factor of 1.5 in noise amplitude than the Gaussian beams.

Bondarescu and Chen also proposed a *optimal* beam noted as *conical beam*, which could maximally reduce the thermal noise with a factor of 2.3 in theory calculation [23]. While to employ this beam, the optical system of the detector needs to be redesign, so that it could have good coupling with the beam.

One big problem with both the mesa and conical beam is that they demand nonstandard optics, which leads to the proposal of the higher-order Laguerre Gauss (LG) modes, more specifically, the  $LG_{3,3}$  mode [24]. This mode is compatible with the current optical cavities employing standard spherical mirrors, meanwhile, it can also reduce the coating thermal noise by a factor of  $\sim 1.6$  in amplitude. Recent research also shows that the behavior of high order LG modes is similar to the standard Gaussian beam [25], which makes it a promising alternative to the current Gaussian beam.

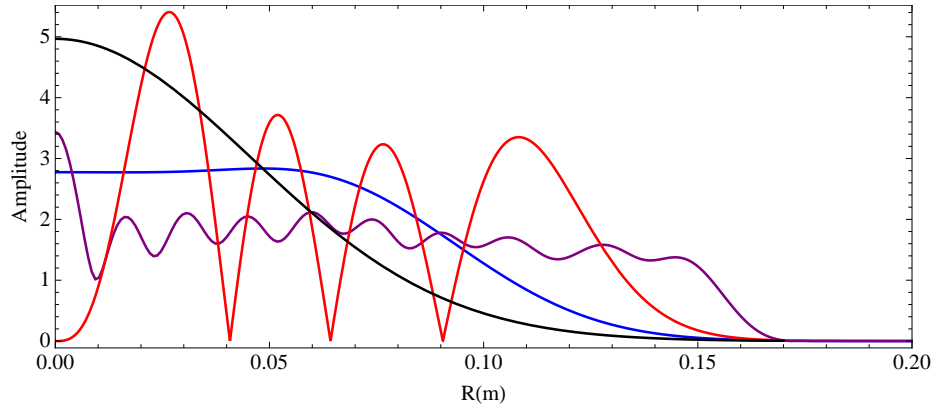


Figure 1.2: The amplitude profiles of Gaussian (black), Mesa (blue), Conical (purple) and  $LG_{3,3}$  (red) modes

### 1.3.3 Mode Degeneracy

However, one issue with using high-order LG modes is that any nonfundamental LG mode is only one member of a degeneracy mode space. For example, the mode (3,3) is ten fold degenerate. This on its own is fine, except when we consider errors of the mirror surface: depending on how the mirror deviates from a perfect spherical shape, the 10-fold space splits into 10 closely modes with profiles that depend on the details of the deviation, which is often called the *mirror figure error*.

In Chapter 3, we consider the consequence of mirror figure error on the application of higher LG modes in advanced interferometric gravitational-wave detectors. In particular, we note that the four mirrors in the arm cavities will all have different figure errors from the manufacturer. This means the two arm cavities will tend to have slightly different optical mode structures, and leading to a degradation of contrast defect.

As we plug in state-of-the art levels of mirror figure error, we find the contrast defect of the interferometer with injecting  $LG_{3,3}$  mode is around  $10^{-2}$ , which is way too big for the effective detection (require contrast defect to be  $\sim 10^{-4}$ ) of GW.

## 1.4 Quantum Dynamics of Optomechanical Systems

As has been mentioned before, the standard quantum limit marks the regime in which quantum measurement induced back action significantly affects the sensitivity of the measuring device. This means gravitational-wave detectors and prototype experiments may also be used to study quantum mechanical behaviors of their macroscopic mirrors. More recently, optomechanical and electromechanical systems at smaller mass scales have been demonstrated at the quantum limit [26–28].

In all quantum opto- and electro-mechanics experiments, the mechanical object (either an oscillator or a nearly free mass) is coupled to light (or microwave), but well isolated to the rest of

the environment. During the experiment, the mechanical object is prepared into quantum states by interacting with light; quantum state of the mechanical object is also read out throughout light.

### 1.4.1 Linear Systems

Most optomechanical systems realized so far operate in the linear regime, in which linear Heisenberg equations of motion can be written for the mechanical object and the optical field. This dramatically simplifies the theoretical treatment of such systems.

As an example, for a Fabry-Perot cavity with a movable mirror, driven by light with  $\omega_0$ , near one particular eigenfrequency  $\omega_c$  of the cavity, we can write down a Hamiltonian of [29]

$$\hat{H} = \hbar\omega_c\hat{a}^\dagger\hat{a} + \frac{\hat{p}^2}{2m} + \frac{1}{2}m\omega_m^2\hat{x}^2 + \hbar G_0\hat{a}^\dagger\hat{a}\hat{x} + i\hbar\sqrt{2\gamma}(\hat{a}_{in}e^{-i\omega_0 t}\hat{a}^\dagger - H.c.). \quad (1.21)$$

Here  $\hat{a}$  and  $\hat{a}_{in}$  is the annihilation operator for the cavity mode and the ingoing optical field;  $\hat{x}$  and  $\hat{p}$  denote the position and momentum of the movable mirror;  $m$  is the mirror mass;  $G_0$  is the optomechanical coupling constant.

The interaction Hamiltonian is proportional to

$$\hat{a}^\dagger\hat{a}\hat{x}. \quad (1.22)$$

In the case the number of photons inside the cavity is large, we can linearize the annihilation (and creation) operator  $\hat{a}$  for the cavity mode by replacing it with the sum of an averaged term and a perturbation term, then deduce a set of linear equations of motion.

Gaussian quantum states (those whose Wigner functions are Gaussian functions of  $x$  and  $p$ ) are the easiest to generate in linear systems, because linear dynamics makes sure that Gaussian states always evolve into Gaussian ones, also because the most easily generated optical states, e.g., coherent states, and squeezed states, are Gaussian. Macroscopic quantum mechanics of linear systems at Gaussian states, in the context of gravitational-wave detectors, has been extensively studied, see, e.g., [30, 31].

If we would like to demonstrate quantum mechanics in less trivial contexts, we will have to prepare non-Gaussian quantum states. This can be done for linear systems, if light can be prepared, via nonlinear means, into non-Gaussian states—and if the transfer of non-Gaussianity from light to mass is efficient. Because non-Gaussianity is almost always a feature of a low number of photons, such an efficient transfer requires a few photons to create enough change in a macroscopic mirror. One way to facilitate this transfer is by “beating” the few photons with a high-amplitude coherent pumping, as has been proposed by Khalili et al. [32].

### 1.4.2 The Simplest Nonlinear Systems

However, in Chapter 4 of this thesis, my collaborators and I consider directly the interaction between a single photon and the movable mirror of a Fabry-Perot cavity—when this interaction is sufficient to modify the momentum of the mirror by a level comparable to its initial quantum uncertainty:

$$\mathcal{F} \frac{\hbar\omega_0}{c} \gtrsim \Delta p \sim \sqrt{\hbar m \omega_m} \quad (1.23)$$

where  $\mathcal{F}$  is the finesse of the cavity; it roughly measures the number of times the photon bounces inside the cavity before leaving. The requirement (1.23) can also be rewritten as

$$\Delta x \sim \sqrt{\frac{\hbar}{m\omega_m}} \gtrsim \frac{\lambda}{2\pi\mathcal{F}} \quad (1.24)$$

which has the interpretation that the linear range of the cavity (around resonance) must be less than the quantum uncertainty in the position of the movable mirror. These equivalent conditions are often referred to as determining the “strong-coupling regime”, although this notion has also been used in a different context, when optical rigidity substantially shifts the frequency of a mechanical oscillator (in practice the latter seems much easier to realize). Recent experimental progress shows that the strong-coupling regime may eventually be accessible by nanomechanical oscillators—although it seems rather hopeless for experiments involving gram or kilogram-scale test masses.

In Chapter 4, we consider the simplest way of driving a strongly coupled optomechanical system: by injecting a single photon with wave function nearly matching the resonant frequency of a high-finesse cavity with a movable mirror. This is neither linear nor Gaussian, yet the simplicity of this problem lies in the fact that there is only one photon in the entire picture, and hence the dimension of the dynamical system one needs to consider is rather low. This has been analyzed by Marshall et al. [33], as a possible experimental scheme that tests the gravity decoherence theory proposed by Penrose [34]. In that experimental proposal, a Michelson interferometer is proposed, with one fixed cavity, and another cavity with a movable mirror.

However, in that previous analysis, the photon was assumed as starting off from within the cavity, instead of being injected from outside. Our calculations shows agreement with Ref. [33] when the photon has a short duration compared with cavity storage time—however, when if the injected photon has an extended duration, the visibility evolution of the interferometer differs significantly from the previous work. In addition, we have found that engineering the photon’s wave function and conditioning on photon’s arrival can be used to prepare the movable mirror into specific quantum states.

## Bibliography

- [1] J. Weber, *Phys. Rev.* **117**, 306 (1960).
- [2] B. Abbott et al., *Rep. Prog. Phys.* **72** 076901 (2009).
- [3] T. Accadia et al., *Journal of Instrumentation*, **7**, P03012 (2012).
- [4] H. Grote and the LIGO Scientific Collaboration, *Class. Quantum Grav.* **27** 084003 (2010).
- [5] M. Ando et al., *Phys. Rev. Lett.* **86**, 3950 (2001).
- [6] K. Kuroda (on behalf of the LCGT Collaboration), *Status of LCGT*, *Class. Quantum Grav* **27**, 084004 (2010).
- [7] G. M. Harry (for the LIGO Scientific Collaboration) *Class. Quantum Grav.* **27** 084006 (2010).
- [8] LIGO Scientific Collaboration, LIGO-T1100309-v5, (2011).
- [9] V. B. Braginsky and F. Ya Khalili, *Quantum Measurements* (Cambridge University Press, Cambridge, (1992).
- [10] G. M. Harry, A. M. Gretarsson, P. R. Saulson, S. E. Kittelberger, S. D. Penn, W. J. Startin, S. Rowan, M. M. Fejer, D. R. M. Crooks, G. Cagnoli, J. Hough and N. Nakagawa, *Class. Quantum Grav.* **19**, 897 (2002).
- [11] M. Evans et al., *Phys. Rev. D* **78**, 102003 (2008).
- [12] V. B. Braginsky, M. L. Gorodetsky, and S. P. Vyatchanin, *Phys. Lett. A* **271**, 303 (2000).
- [13] V. B. Braginsky, Y. Levin and S. P. Vyatchanin, *Meas. Sci. Technol.* **10**, 598 (1999).
- [14] G. González, *Class. Quantum Grav.* **17**, 4409 (2000).
- [15] J. Harms, R. DeSalvo, S. Dorsher, and V. Mandic, arXiv:0910.2774, (2009)
- [16] H. B. Callen and T. A. Welton, *Phys. Rev.* **83**, 34 (1951).
- [17] Y. Levin, *Phys. Rev. D* **57**, 659 (1998).
- [18] Y. Levin, *Phys. Lett. A* **372**, 1941 (2008).
- [19] J. Agresti, G. Castaldi, R. DeSalvo, V. Galdi, V. Pierro, and I. M. Pinto, LIGO-P060027-00-Z.
- [20] A. G. Gurkovsky et al., *Phys. Lett. A* **375**, 4147 (2011).
- [21] G. Lovelace, *Class. Quant. Gravity* **24**, 4491 (2007).

- [22] E. D'Ambrosio, R. O'Shaughnessy, K. Thorne, S. Strigin, and S. Vyatchanin, *Class. Quant. Gravity* **21**, S867 (2004).
- [23] M. Bondarescu, O. Kogan, and Y. Chen, *Phys. Rev. D* **78**, 082002 (2008).
- [24] B. Mours, E. Tournefier, and J.-Y. Vinet, *Class. Quant. Gravity* **23**, 5777 (2006).
- [25] S. Chelkowski, S. Hild and A. Freise, *Phys. Rev. D* **79**, 122002 (2009).
- [26] J. D. Teufel, T. Donner, Dale Li, J. W. Harlow, M. S. Allman, K. Cicak, A. J. Sirois, J. D. Whittaker, K. W. Lehnert, and R. W. Simmonds, *Nature* **475**, 359 (2011).
- [27] A. H. Safavi-Naeini, J. Chan, J. T. Hill, T. P. M. Alegre, A. Krause, and O. Painter, arXiv:1108.4680 [quant-ph].
- [28] S. Gupta, K.L. Moore, K.W. Murch, and D.M. Stamper-Kurn, *Phys. Rev. Lett.* **99**, 213601 (2007).
- [29] H. Miao, S. Danilishin, H. Mller-Ebhardt and Y. Chen, *New J. Phys.* **12**, 083032 (2010).
- [30] C. Genes, D. Vitali and P. Tombesi, *New J. Phys.* **10**, 095009 (2008).
- [31] F. Marquardt, J. P. Chen, A. A. Clerk, and S. M. Girvin, *Phys. Rev. Lett.* **99**, 093902 (2007).
- [32] F. Khalili, S. Danilishin, H. Miao, H. Mller-Ebhardt, H. Yang, and Y. Chen, *Phys. Rev. Lett.* **105**, 070403 (2010).
- [33] W. Marshall, C. Simon, R. Penrose, and D. Bouwmeester, *Phys. Rev. Lett.* **91**, 130401 (2003).
- [34] R. Penrose, *Gen. Rel. Grav.* **28** 581 (1996).

## Chapter 2

# Coating Thermal Noise in Interferometric Gravitational Wave Detectors

We analyze the structure of the Brownian thermal noise of a multilayer dielectric coating, used in high-precision optical measurements, e.g., interferometric gravitational-wave detectors. We assume the coating material to be isotropic, and therefore study thermal noises as arising from shear and bulk losses of coating materials. We show that coating noise arises not only from layer thickness fluctuations, but also from fluctuations of the interface between the coating and substrate, driven by internal fluctuating stresses of the coating. In addition, the nonzero photoelastic coefficients of the thin films modifies the influence of the thermal noise on the laser field. Among different layers, thickness fluctuations are statistically independent. However, coherence exists between layers and the substrate-coating interface. Taking into account uncertainties in material parameters, we show that significant uncertainties still exist in estimating coating Brownian noise.

---

Originally published as T. Hong, H. Yang, E. Gustafson, R. Adhikari, and Y. Chen, LIGO Document P1200012 (2012), will submit to Physics Review D.

## 2.1 Introduction

Brownian thermal noise in the dielectric coatings of mirrors limits some high precision experiments which use optical metrology. This thermal noise is currently a limit for fixed spacer Fabry-Perots used in optical clock experiments [1] and is estimated to be the dominant noise source in the most sensitive band of modern gravitational wave detectors (e.g., advanced LIGO, GEO, advanced VIRGO and LCGT) [2–6]. Recent work has indicated the possibility of suppressing the various kinds of thermal noise by redesigning the shape of the substrate and the structure of the multi-layer coating [7, 8]. In this paper, we seek a comprehensive understanding of coating Brownian noise, by identifying individual sources of fluctuations, calculating their cross spectra using the fluctuation dissipation theorem [9, 10, 13], and finally evaluating how each of the sources and their correlations add up to the total noise.

As a starting point, we will assume each coating layer to be isotropic, and hence completely characterized by its complex bulk modulus  $K$  and shear modulus  $\mu$ —each with small imaginary parts related to energy loss in bulk and shear motions. The complex arguments of these moduli are often referred to as *loss angles*. While values of  $K$  and  $\mu$  are generally known, loss angles vary significantly according to the details of how coating materials are applied onto the substrate and their composition. Since the loss angles are small, we will still use  $K$  and  $\mu$  to denote the real parts of the bulk and shear moduli, and write the complex bulk and shear moduli,  $\tilde{K}$  and  $\tilde{\mu}$  as

$$\tilde{K} = K(1 + i\phi_B), \quad \tilde{\mu} = \mu(1 + i\phi_S). \quad (2.1)$$

Here we have used subscripts  $B$  and  $S$  to denote bulk and shear, because these will be symbols for bulk strain and shear strain. Note that this definition differs from previous literature and measurements, which used  $\phi_{\parallel}$  and  $\phi_{\perp}$  to denote losses induced by elastic deformations parallel and orthogonal to the coating-substrate interface [11]. We argue in Appendix 2.11 that  $\phi_{\parallel}$  and  $\phi_{\perp}$  cannot be consistently used as the loss angles of a material.

Brownian thermal fluctuations of a multilayer coating can be divided as follows: (i) thickness fluctuation of the coating layers, (ii) fluctuation of the coating-substrate interface, and (iii) refractive index fluctuations of the coating layers associated with longitudinal (thickness) and transverse (area) elastic deformations—as illustrated in Figure 2.1. Using what is sometimes referred to as the Levin’s direct approach [10] (based on the fluctuation dissipation theorem), one can lump all three contributions into one quantity, and calculate its noise spectral density by calculating the mechanical dissipation rate when a distribution of mechanical forces are applied at various locations on the coated mirror [as has been done by Vyatchanin et al. [12]]. However, in order to obtain insights into coating noise that have proven useful we have chosen to calculate the cross spectral densities for each of (i), (ii), and (iii), and provide intuitive interpretations of each. We will show, that (i)

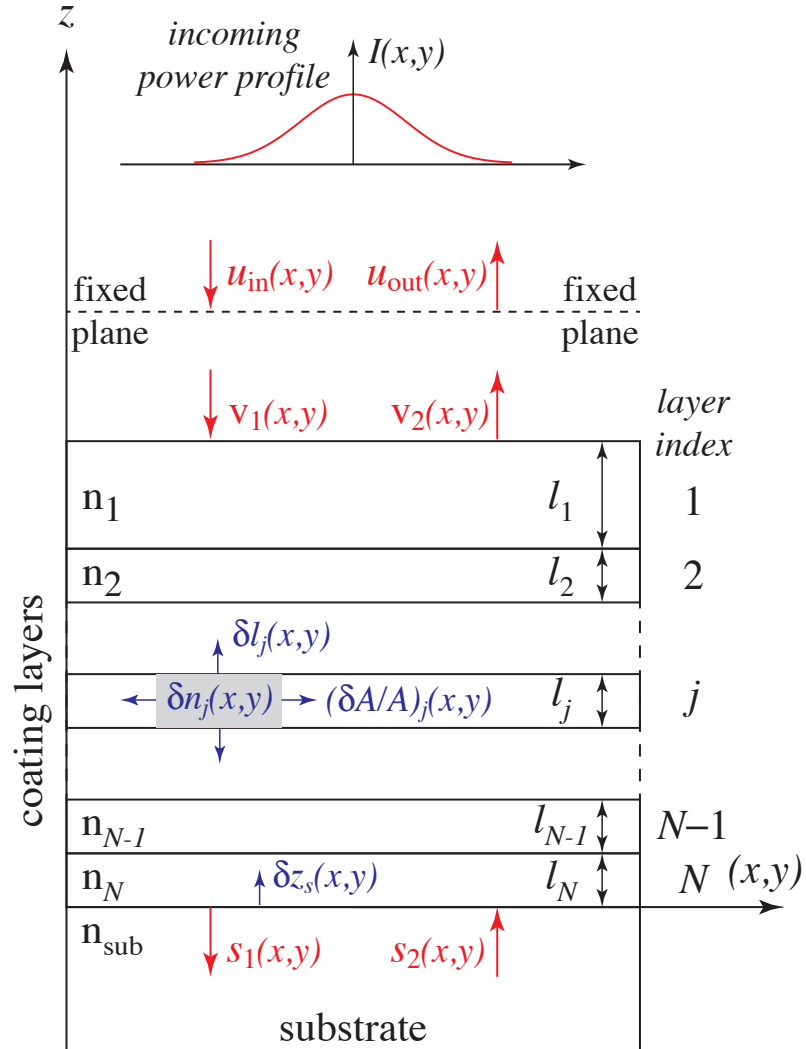


Figure 2.1: Schematic plot of a mirror coated with multiple dielectric layers. Shown here are the various fluctuations that contribute to coating noise, i.e., fluctuations in the amplitude and phase of the returning light caused by fluctuations in the geometry (e.g., layer thickness  $\delta l_j$ , layer area stretch  $(\delta A/A)_j$  and interface height  $z_s$ ) of the coating-substrate configuration and in refractive indices  $[\delta n_j(x, y, z)]$  of the layers.

and (ii) above are driven by both bulk and shear fluctuations in the coating, in such a way that thickness fluctuations of the  $j$ -th layer  $\delta l_j$ , or in transverse locations separated by more than coating thickness, are mutually statistically independent, yet each  $\delta l_j$  is correlated with the fluctuation of the coating-substrate interface  $z_s$ —because  $z_s$  is driven by the *sum* of thermal stresses in the coating layers. We will also show that when coating thickness is much less than the beam spot size, the only significant contribution to (iii) arises from longitudinal (thickness) fluctuations.

This paper is organized as follows. In Sec. 2.2, we express the amplitude and phase of the out-going field in terms of fluctuations in the coating structure, thereby identifying the various components of coating thermal noise. In Sec. 2.3, we introduce the loss angles of isotropic coating materials, and use the Fluctuation-Dissipation Theorem to calculate the cross spectral densities of the coating thermal noise ignoring light penetration into the multi-layer coating. In Sec. 2.4, we discuss in detail the cross spectra of all the components of the coating structure fluctuation, thereby obtaining the full formula for coating thermal noise, taking light penetration into account. In Sec. 2.5, we discuss the effect of light penetration on coating thermal noise, using typical optical coating structures. In Sec. 2.6, we discuss the dependence of thermal noise on the material parameters, and optimize the coating structure in order to lower the thermal noise. In Sec. 2.7, we discuss how only one combination of the two loss angles have been measured in past experiments, and how other different combinations can be measured using a new experimental geometry. Finally, we summarize our main conclusions in Sec. 2.8.

## 2.2 Components of the Coating Thermal Noise

In this section, we express the coating thermal noise in terms of the elastic deformations of the coated substrate.

### 2.2.1 Complex Reflectivity

As illustrated in Figure 2.1, we consider a laser field normally incident (along the  $-z$  direction) onto the mirror, with complex amplitude profile  $u_{\text{in}}(x, y)$  at a fixed reference plane (dashed line in the figure) and intensity profile  $I(x, y) = |u_{\text{in}}(x, y)|^2$ . Henceforth in the paper, we shall use arrows (e.g.,  $\vec{x}$ ) to denote the 2-dimensional vector  $(x, y)$  in the *transverse plane*, and boldface letters (e.g.,  $\mathbf{x}$ ) to denote 3-dimensional vectors.

Because coating thickness is much less than the beam spot size, the reflected field (traveling along the  $+z$  direction) at transverse location  $\vec{x}$  has an amplitude given by

$$u_{\text{out}}(\vec{x}) = \rho_{\text{tot}}(\vec{x})u_{\text{in}}(\vec{x}), \quad (2.2)$$

which only depends on the complex reflectivity  $\rho_{\text{tot}}(\vec{x})$  and the complex amplitude of the incident field  $u_{\text{in}}(\vec{x})$ , at the same location  $\vec{x}$ —assuming no incident light from the substrate (i.e.,  $s_2 = 0$ ). Here  $\rho_{\text{tot}}(\vec{x})$  can be separated into three factors, as

$$\rho_{\text{tot}}(\vec{x}) = \frac{u_{\text{out}}(\vec{x})}{u_{\text{in}}(\vec{x})} = \left[ \frac{u_{\text{out}}(\vec{x})}{v_2(\vec{x})} \right] \left[ \frac{v_1(\vec{x})}{u_{\text{in}}(\vec{x})} \right] \left[ \frac{v_2(\vec{x})}{v_1(\vec{x})} \right] \quad (2.3)$$

in which  $v_1(\vec{x})$  is the incident complex amplitude at the coating-air interface, while  $v_2(\vec{x})$  is the reflected complex amplitude at that interface.

The first two phase factors on the right-hand side of Eq. (2.3) are gained by the light when traveling across the gap between the fixed reference plane (see Fig. 2.1) and the coating-air interface; we therefore obtain, up to a constant phase factor,

$$\left[ \frac{u_{\text{out}}(\vec{x})}{v_2(\vec{x})} \right] \left[ \frac{v_1(\vec{x})}{u_{\text{in}}(\vec{x})} \right] = e^{-2ik_0[\delta z_s(\vec{x}) + \sum_{j=1}^N \delta l_j(\vec{x})]} \quad (2.4)$$

where  $k_0 = \omega_0/c$  is the wave number of the laser ( $\omega_0$  its angular frequency) in vacuum,  $z_s(\vec{x})$  is the vertical displacement of the coating-substrate interface (from its zero point), and  $l_j(\vec{x})$  is the thickness of the  $j$ -th coating layer—both evaluated at a transverse location  $\vec{x}$ .

The remaining complex reflectivity  $v_2(\vec{x})/v_1(\vec{x})$  can be determined as a function of the phase shift experienced by the field in each layer, as well as the reflectivity of each interface, as described in detail in Sec. 2.5. We can write:

$$v_2/v_1 = \rho[\phi_1(\vec{x}), \dots, \phi_N(\vec{x}); r_{01}(\vec{x}), \dots, r_{Ns}(\vec{x})]. \quad (2.5)$$

Here  $\rho$  is the complex reflectivity of a multilayer coating, measured at the coating-air interface, which in turn depends on the optical thickness  $\phi_j(\vec{x})$  of each layer ( $j = 1, \dots, N$ ) and the reflectivity  $r_{p,p+1}(\vec{x}) \equiv r_p(\vec{x})$  of each interface, ( $p = 0, \dots, N$ , with  $p = N + 1$  representing the substrate, and  $p = 0$  the vacuum outside the coating). Assembling the above equations (2.3)–(2.5), we obtain:

$$\rho_{\text{tot}}(\vec{x}) = e^{-2ik_0[\delta z_s(\vec{x}) + \sum_{j=1}^N \delta l_j(\vec{x})]} \rho[\{\phi_j(\vec{x})\}; \{r_p(\vec{x})\}]. \quad (2.6)$$

Brownian thermal forces lead to fluctuations in both the real and imaginary parts of this complex reflectivity. Fluctuations in the argument of the complex reflectivity phase modulates the out-going light and directly produces sensing noise. Fluctuations in the magnitude, on the other hand, amplitude modulate the out-going light, and produces a ponderomotive force noise.

### 2.2.2 Thermal Phase and Amplitude Noise

Brownian thermal fluctuations in coating geometry and refractive index modify the total reflectivity  $\rho_{\text{tot}}(\vec{x})$  defined in Eq. (2.6). The real and imaginary parts of

$$\delta \log \rho_{\text{tot}}(\vec{x}) = \frac{\delta \rho_{\text{tot}}(\vec{x})}{\rho_{\text{tot}}(\vec{x})} \quad (2.7)$$

encode the amplitude/intensity and phase fluctuations of the reflected light at position  $\vec{x}$  on the mirror surface. In particular, intensity fluctuation of the reflected light is given by

$$\frac{\delta I(\vec{x})}{I(\vec{x})} = 2 \frac{\delta |\rho_{\text{tot}}(\vec{x})|}{|\rho_{\text{tot}}(\vec{x})|} = 2 \text{Re} [\delta \log \rho_{\text{tot}}(\vec{x})] \quad (2.8)$$

while phase fluctuation is given by

$$\delta \phi(\vec{x}) = \delta \arg [\rho_{\text{tot}}(\vec{x})] = \text{Im} [\delta \log \rho_{\text{tot}}(\vec{x})] . \quad (2.9)$$

In this way, if we further write

$$\xi(\vec{x}) - i\zeta(\vec{x}) = -\frac{i}{2k_0} \delta [\log \rho_{\text{tot}}] , \quad (2.10)$$

with both  $\xi$  and  $\zeta$  real-valued functions of  $\vec{x}$ , with the dimensionality of displacement; they will represent phase and amplitude noise, respectively. In particular, from Eq. (2.9), we have

$$2k_0 \xi(\vec{x}) = \delta \phi(\vec{x}) , \quad (2.11)$$

and this means  $\xi(\vec{x})$  corresponds to the spurious displacement measured by the reflected light due to phase fluctuations caused by the coating.

The quantity  $\zeta$  is connected to amplitude/intensity noise via

$$2k_0 \zeta(\vec{x}) = \text{Re} [\delta \log \rho_{\text{tot}}] = \frac{\delta I(\vec{x})}{2I(\vec{x})} . \quad (2.12)$$

As we shall discuss in Sec. 2.2.5,  $\zeta$  will cause a fluctuating force on the mirror, and contribute to measurement noise, although the effect will be small for gravitational-wave detectors.

Inserting the dependence of  $\rho_{\text{tot}}$  on  $\rho$ ,  $l_j$  and  $z_s$ , we obtain

$$\begin{aligned} \xi(\vec{x}) - i\zeta(\vec{x}) &= -\delta z_s(\vec{x}) - \sum_{j=1}^N \delta l_j(\vec{x}) \\ &\quad - \sum_{j=1}^N \frac{i}{2k_0} \left[ \frac{\partial \log \rho}{\partial \phi_j} \cdot \delta \phi_j(\vec{x}) \right] \\ &\quad - \sum_{p=0}^N \frac{i}{2k_0} \left[ \frac{\partial \log \rho}{\partial r_p} \cdot \delta r_p(\vec{x}) \right]. \end{aligned} \quad (2.13)$$

The first two terms are due to the motion of the coating-air interface at location  $\vec{x}$  and thickness fluctuations of the layers, while the last two terms are due to light penetration into the coating layers. In particular, the third term is due to fluctuations in the total phase the light gains when propagating within the  $j$ -th layer, while the fourth term is due to the (effective) reflectivity of the  $p$ -th interface (with  $p = 0$  indicating the coating-air interface), whose origin will be explained below.

### 2.2.3 Fluctuations $\delta \phi_j$ and $\delta r_p$

Light propagating within the coating layers are affected by the *photoelastic* effect, namely an *isothermal* fluctuation in  $\delta n_j(\mathbf{x})$  (note here that  $\mathbf{x}$  is a 3-D vector) due to fluctuating Brownian stresses exerted onto the coating materials. Assuming *isotropy* of the coating materials, we can write

$$\delta n_j(\mathbf{x}) = \beta_j^L S_{zz}(\mathbf{x}) + \beta_j^T [S_{xx}(\mathbf{x}) + S_{yy}(\mathbf{x})] \quad (2.14)$$

with

$$\beta_j^L \equiv \left( \frac{\partial n_j}{\partial \log l} \right)_{A_j}, \quad \beta_j^T \equiv \left( \frac{\partial n_j}{\partial \log A} \right)_{l_j}. \quad (2.15)$$

Here  $L$  stands for longitudinal, and  $T$  stands for transverse, and the subscript  $A_j$  and  $l_j$  indicate fixing transverse area and longitudinal length, respectively. We have also used the usual strain definition

$$S_{ij} \equiv \frac{1}{2} \left[ \frac{\partial u_i}{\partial x_j} + \frac{\partial u_j}{\partial x_i} \right] \quad (2.16)$$

where  $u_i(\mathbf{x})$ ,  $i = 1, 2, 3$  are components of the displacement vector of the mass element at position  $\mathbf{x}$ . Please refer to Appendix 2.10 for more details in defining the elasticity quantities, and Appendix 2.9.1 for more details on the photo elastic effect.

We note that in Eq. (2.14)  $S_{zz}$  is the fractional increase in length (i.e., linear expansion) in the longitudinal direction, while  $S_{xx} + S_{yy}$  is the fractional increase in the transverse area. According to Appendix 2.9.4, we can ignore the second term representing area fluctuations in Eq. (2.14) when the beam spot size is much larger than the coating thickness. In this case, we write  $\beta_j$  in place for  $\beta_j^L$ , whose value can be expressed in terms of a particular component of the photo elastic tensor, see

Eq. (2.119).

As we discuss in Appendix 2.9.2, the (surviving) first term of Eq. (2.14) causes two effects for light propagating along each direction (i.e.,  $+z$  and  $-z$ ): it adds an additional phase shift onto the light, and it back-scatters a fraction of the light into the opposite direction. As we show in Appendix 2.9.3 [c.f. Eqs. (2.130)–(2.132)], these effects can be described by modifying the phase shift  $\delta\phi_j$  of each coating layer and the reflectivity  $\delta r_j$  of interface:

$$\delta\phi_j = k_0 \left[ (n_j + \beta_j)\delta l_j - \frac{1 - r_j^2}{2r_j} \beta_j \delta l_j^c + \frac{1 + r_{j-1}^2}{2r_{j-1}} \beta_{j-1} \delta l_{j-1}^c \right], \quad (2.17)$$

$$\delta r_j = k_0 t_j^2 \beta_j \delta l_j^s. \quad (2.18)$$

Here we have defined

$$\delta l_j^c = - \int_0^{l_j} S_{zz}(z_{j+1} + z) \cos(2k_0 n_j z) dz \quad (2.19)$$

$$\delta l_j^s = - \int_0^{l_j} S_{zz}(z_{j+1} + z) \sin(2k_0 n_j z) dz \quad (2.20)$$

for  $j \geq 1$ ,  $\delta l_0^s = \delta l_0^c = 0$ , and

$$z_j \equiv \sum_{n=j}^N l_n \quad (2.21)$$

marks the  $z$ -coordinate of the top surface of the  $j$ -th layer. We can also write

$$\delta l_j = \int_0^{l_j} S_{zz}(z_{j+1} + z) dz. \quad (2.22)$$

Note that

$$\begin{array}{l} \text{total coating} \\ \text{thickness} \end{array} = z_1 > z_2 > \dots > z_{N+1} = 0. \quad (2.23)$$

Note that  $\delta r_j$ , as well as the last two terms in  $\delta\phi_j$  are due to back-scattering, and have not been considered by previous authors.

Inserting Eqs. (2.17), (2.18) into Eq. (2.13), we obtain:

$$\xi(\vec{x}) - i\zeta(\vec{x}) = -z_s(\vec{x}) - \sum_{j=1}^N \int_{z_{j+1}}^{z_j} \left[ 1 + \frac{i\epsilon_j(z)}{2} \right] u_{zz}(\vec{x}, z) dz \quad (2.24)$$

where

$$\begin{aligned}
\epsilon_j(z) &= (n_j + \beta_j) \frac{\partial \log \rho}{\partial \phi_j} \\
&- \beta_j \left[ \frac{1 - r_j^2}{2r_j} \frac{\partial \log \rho}{\partial \phi_j} \right. \\
&\quad \left. - \frac{1 + r_j^2}{2r_j} \frac{\partial \log \rho}{\partial \phi_{j+1}} \right] \cos[2k_0 n_j (z - z_j)] \\
&- t_j^2 \beta_j \frac{\partial \log \rho}{\partial r_j} \sin[2k_0 n_j (z - z_{j+1})], \tag{2.25}
\end{aligned}$$

a term that accounts for all effects associated with light penetration. Here we need to formally define

$$\frac{\partial \log \rho}{\partial \phi_{N+1}} = 0 \tag{2.26}$$

since  $\phi_{N+1}$  does not really exist. Alternatively, we can also write formulas separately for  $\xi$  and  $\zeta$ , using only real-valued quantities. For  $\xi$ , we have,

$$\begin{aligned}
\xi(\vec{x}) &= -z_s(\vec{x}) \\
&- \sum_{j=1}^N \left[ \mathcal{T}_j^\xi \delta l_j(\vec{x}) + \mathcal{T}_j^{\xi c} \delta l_j^c(\vec{x}) + \mathcal{T}_j^{\xi s} \delta l_j^s(\vec{x}) \right], \tag{2.27}
\end{aligned}$$

where

$$\mathcal{T}_j^\xi = 1 - \frac{n_j + \beta_j}{2} \text{Im} \left( \frac{\partial \log \rho}{\partial \phi_j} \right) \tag{2.28}$$

$$\begin{aligned}
\mathcal{T}_j^{\xi c} &= -\frac{\beta_j}{4} \text{Im} \left( \frac{\partial \log \rho}{\partial \phi_j} \right) \left( \frac{1 - r_j^2}{r_j} \right) \\
&+ \frac{\beta_j}{4} \text{Im} \left( \frac{\partial \log \rho}{\partial \phi_{j+1}} \right) \left( \frac{1 + r_j^2}{r_j} \right) \tag{2.29}
\end{aligned}$$

$$\mathcal{T}_j^{\xi s} = -\frac{\beta_j t_j^2}{2} \text{Im} \left( \frac{\partial \log \rho}{\partial r_j} \right) \tag{2.30}$$

are transfer functions from the various  $\delta l$ 's to the displacement-equivalent thermal noise. For  $\zeta$ , we have

$$\zeta(\vec{x}) = \sum_{j=1}^N \left[ \mathcal{T}_j^\zeta \delta l_j(\vec{x}) + \mathcal{T}_j^{\zeta c} \delta l_j^c(\vec{x}) + \mathcal{T}_j^{\zeta s} \delta l_j^s(\vec{x}) \right] \tag{2.31}$$

where

$$\mathcal{T}_j^\zeta = \frac{n_j + \beta_j}{2} \operatorname{Re} \left( \frac{\partial \log \rho}{\partial \phi_j} \right) \quad (2.32)$$

$$\begin{aligned} \mathcal{T}_j^{\zeta c} &= \frac{\beta_j}{4} \operatorname{Re} \left( \frac{\partial \log \rho}{\partial \phi_j} \right) \left( \frac{1 - r_j^2}{r_j} \right) \\ &\quad - \frac{\beta_j}{4} \operatorname{Re} \left( \frac{\partial \log \rho}{\partial \phi_{j+1}} \right) \left( \frac{1 + r_j^2}{r_j} \right) \end{aligned} \quad (2.33)$$

$$\mathcal{T}_j^{\zeta s} = \frac{\beta_j t_j^2}{2} \operatorname{Re} \left( \frac{\partial \log \rho}{\partial r_j} \right). \quad (2.34)$$

Although for an arbitrary stack of dielectrics,  $\zeta$  is comparable to the part of  $\xi$  [c.f. Eq. (2.25)] that involves light penetration into the layers. In practice, for highly reflective stacks, the real parts of  $\partial \log \rho / \partial \phi_j$  and  $\partial \log \rho / \partial r_j$  all turn out to be small, and therefore fluctuations in  $\zeta$  should be much less than fluctuations in  $\xi$ .

## 2.2.4 Mode Selection for Phase Noise

So far we have calculated phase and amplitude noise as functions of location  $\vec{x}$  on the mirror surface. However, there is only one displacement noise that the light will sense. In this and the next subsection, show how  $\xi(\vec{x})$  and  $\zeta(\vec{x})$  should be converted into measurement noise. In doing so, we recognize that only one spatial optical mode is injected on resonance in the optical cavity, and this mode has a complex amplitude of  $u_0(\vec{x})$  at the mirror surface. Now suppose we have  $u_{\text{in}} = u_0(\vec{x})$  incident on the mirror surface, we will then have  $u_{\text{out}}(\vec{x}) = \rho_{\text{tot}}(\vec{x})u_0(\vec{x})$ , which contains not only the resonant mode, but also other modes, which do not resonate in the cavity.

Let us select only the component of  $u_{\text{out}}(\vec{x})$  resonates, then we have a complex reflectivity of

$$\bar{\rho} = \frac{\int u_0^*(\vec{x})u_{\text{out}}(\vec{x})d^2\vec{x}}{\int u_0^*u_0d^2\vec{x}} = \frac{\int \rho_{\text{tot}}(\vec{x})I(\vec{x})d^2\vec{x}}{\int I(\vec{x})d^2\vec{x}}, \quad (2.35)$$

specifically for the resonant mode, and hence independent of  $\vec{x}$ . Here we have defined  $I(\vec{x}) \equiv |u_0(\vec{x})|^2$ . Note that the bar on top of  $\bar{\rho}$  represents averaging over the phase front, instead of averaging over time.

Now, inserting Eq. (2.10) as definitions for  $\xi(\vec{x})$  and  $\zeta(\vec{x})$  into Eq. (2.35), we obtain the fluctuating part of  $\bar{\rho}$

$$\frac{\delta \bar{\rho}}{\bar{\rho}} = 2ik_0(\bar{\xi} - i\bar{\zeta}), \quad (2.36)$$

where

$$\bar{\xi} \equiv \frac{\int \xi(\vec{x})I(\vec{x})d^2\vec{x}}{\int I(\vec{x})d^2\vec{x}}, \quad \bar{\zeta} \equiv \frac{\int \zeta(\vec{x})I(\vec{x})d^2\vec{x}}{\int I(\vec{x})d^2\vec{x}}. \quad (2.37)$$

Note that  $2ik_0\bar{\xi}$  is the additional phase gained by the returning light, while  $2k_0\bar{\zeta}$  is the relative

change in amplitude [see discussions in Sec. 2.2.2]. Focusing first on  $\bar{\xi}$ , we note that this creates the same phase as that gained by the reflected light if the mirror does not deform but instead moves by  $\bar{\xi}$ . In this way,  $\bar{\xi}$  is an error in our measurement of the mirror's displacement.

### 2.2.5 Conversion of Amplitude Noise into Displacement

The amplitude thermal noise produces spurious GW signal by modulating the radiation pressure acting on the mirror, which in turn drives spurious mirror motion. Let us first consider a single-bounce scenario, in which an incoming beam with intensity profile  $I(\vec{x})$ , unaffected by thermal noise, is reflected with an intensity profile  $I(\vec{x}) + \delta I(\vec{x})$ , with  $\delta I(\vec{x})$  induced by amplitude thermal noise. In this case, the mirror feels a thermal-noise-induced recoil force of

$$F_{\text{th}}^{\text{single}} = \int \frac{\delta I(\vec{x})}{c} d^2\vec{x}. \quad (2.38)$$

Using Eqs. (2.12) and (2.37), we obtain

$$F_{\text{th}}^{\text{single}} = \frac{4I_0 k_0}{c} \bar{\zeta} \quad (2.39)$$

with  $I_0$  the power incident on the mirror. If the mirror is within a cavity, then we need to consider both the increase in the circulating power (which we denote by  $I_c$ ) with respect to the input power, and the coherent build-up of amplitude modulation within the cavity. We also note that now both the incident and reflected beam contains amplitude modulation, and that we must also consider the effect of this amplitude modulation on the input mirror.

If we restrict ourselves to a single optical cavity on resonance, then the force thermal noise below the cavity bandwidth is given by

$$F_{\text{th}}^{\text{cav}} = \frac{16k_0 I_c}{c\sqrt{T_1}} \bar{\zeta}. \quad (2.40)$$

Here  $I_c$  is the circulating power in the arm cavity. Suppose both input and end mirrors have the same mass  $M$ , then the spectrum of cavity length modulation driven by the amplitude thermal noise is given by

$$\sqrt{S_{\text{th}}^{\text{amp}}} = \frac{2}{m\Omega^2} \sqrt{S_{F_{\text{th}}^{\text{cav}}}} = \frac{32\omega_0 I_c}{m\Omega^2 c^2 \sqrt{T_1}} \sqrt{S_{\bar{\zeta}}}. \quad (2.41)$$

Note that  $\bar{\zeta}$  has the units of displacement, and therefore the prefactor in front of  $\sqrt{S_{\bar{\zeta}}}$  in Eq. (2.41) is a dimensionless conversion factor from  $\bar{\zeta}$  to displacement noise. For Advanced LIGO, this cannot be completely dismissed at this stage, because

$$\frac{32\omega_0 I_c}{m\Omega^2 c^2 \sqrt{T_1}} = 18 \cdot \frac{I_c}{800 \text{ kW}} \cdot \frac{40 \text{ kg}}{m} \cdot \left[ \frac{10 \text{ Hz}}{\Omega/(2\pi)} \right]^2 \sqrt{\frac{0.03}{T_1}}. \quad (2.42)$$

Nevertheless, as we will show in Sec. 2.5.2, the minor amplification factor here is not enough in

making amplitude noise significant, because  $\zeta$  tend to be much less than  $\xi$ , for the coatings we consider.

## 2.3 Thermal Noise Assuming No Light Penetration into the Coating

In this section, we compute the coating Brownian noise assuming that the incident light does not penetrate into the coating. This means light is promptly reflected at the coating-air interface, and therefore we should only keep the first two terms on the right-hand side of Eq. (2.13), which leads to  $\zeta = 0$ . We therefore consider only coating phase noise  $\xi$ , in particular its weights average throughout the mirror surface,  $\bar{\xi}$ , see Eq. (2.37).

### 2.3.1 The Fluctuation-Dissipation Theorem

The fluctuation dissipation theorem relates the near-equilibrium thermal noise spectrum of a generalized coordinate  $q$  to the rate of dissipation in the system when a generalized force acts directly on this coordinate. More specifically, the thermal noise spectrum of  $q$  at temperature  $T$  is given by [13]

$$S_q(f) = \frac{k_B T}{\pi^2 f^2} \text{Re}[Z(f)] \quad (2.43)$$

where  $f$  is frequency,  $Z(f)$  is the mechanical impedance (inverse of admittance), or

$$Z(f) = -2\pi i f q(f) / F(f). \quad (2.44)$$

Alternatively, imagining a sinusoidal force

$$F(t) = F_0 \cos(2\pi f t) \quad (2.45)$$

with amplitude  $F_0$  acting directly on  $q$ , Eq. (2.43) can also be written as

$$S_x(f) = \frac{4k_B T}{\pi f} \frac{W_{\text{diss}}}{F_0^2} = \frac{4k_B T}{\pi f} \frac{U}{F_0^2} \phi \quad (2.46)$$

where  $W_{\text{diss}}$  is the energy dissipated per cycle of oscillation divided by  $2\pi$  (in other words,  $W_{\text{diss}}$  is the average energy loss per radian),  $U$  is the peak of the stored energy in the system, and  $\phi$  is the loss angle, defined by

$$\phi = \text{Re}[Z(f)] / \text{Im}[Z(f)]. \quad (2.47)$$

It is important to note that  $\phi$  is in general frequency dependent. However, for an elastic body, if

the frequency is low enough (much below the first eigenfrequency), then  $U$  can be computed using the quasi-static approximation, because it is equal to the elastic energy stored in the equilibrium configuration when a constant  $F_0$  is applied to the system.

### 2.3.2 Mechanical Energy Dissipations in Elastic Media

It is straightforward to apply Eq. (2.46) to calculate the thermal noise component due to fluctuation of the position of the coating-air interface—the weighted average [c.f. Eq. (2.35)] of the first two terms of Eq. (2.13). This can be obtained by applying a force  $F$  with a pressure profile proportional to  $I(\vec{x})$  on to the mirror surface (coating-air interface). In this case, elastic energy can be divided into bulk energy  $U_B$  and shear energy  $U_S$  [Chapter I of Ref. [14]], with

$$U_{\text{coating}} = U_B + U_S = \int_{\text{coating}} \left( \frac{K}{2} \Theta^2 + \mu \Sigma_{ij} \Sigma_{ij} \right) dV, \quad (2.48)$$

where  $\Theta$  is the expansion, and  $\Sigma_{ij}$  is the shear tensor (see Appendix 2.10 for details). If we give small imaginary parts to  $K$  and  $\mu$ , writing

$$\tilde{K} = K(1 + i\phi_B), \quad \tilde{\mu} = \mu(1 + i\phi_S) \quad (2.49)$$

then  $W_{\text{diss}}$  can be written as

$$W_{\text{diss}} = \phi_B U_B + \phi_S U_S. \quad (2.50)$$

Here we have introduced the loss angles  $\phi_B$  and  $\phi_S$ , which are associated with the dissipation of expansion energy density and the shear energy density, respectively. Note that our way of characterizing loss differs from previous work by Harry, et. al. [11], because for isotropic materials,  $\phi_B$  and  $\phi_S$  are the two fundamentally independent loss angles that characterize the dissipation of bulk and shear elastic energy; were we to literally adopt  $\phi_{\perp}$  and  $\phi_{\parallel}$  as done in Ref. [11], there would be modes of external driving that lead to negative dissipative energy, as shown explicitly in Appendix 2.11.

Once we have introduced  $\phi_B$  and  $\phi_S$ , other elastic moduli also gain small imaginary parts correspondingly. For example, for the most widely used Young's modulus and Poisson ratio, because

$$K = \frac{Y}{3(1-2\sigma)}, \quad \mu = \frac{Y}{2(1+\sigma)} \quad (2.51)$$

we can write

$$\tilde{Y} = Y(1 + i\phi_Y) \quad (2.52)$$

with

$$\phi_Y = \frac{(1 - 2\sigma)\phi_B + 2(1 + \sigma)\phi_S}{3} \quad (2.53)$$

and

$$\tilde{\sigma} = \sigma + \frac{i}{3}(1 - 2\sigma)(1 + \sigma)(\phi_B - \phi_S). \quad (2.54)$$

Since  $-1 < \sigma < 1/2$ , we have  $(1 - 2\sigma)(1 + \sigma) > 0$ , therefore  $\tilde{\sigma}$  has a positive imaginary part as  $\phi_B$  is greater than  $\phi_S$ , and vice versa. To understand the physical meaning of the imaginary part of the Poisson ratio, one has to realize that Young's modulus and Poisson ratio together describe the elastic response of a rod. Suppose we apply an oscillatory tension uniformly along a rod at a very low frequency, whether the area of the rod leads or lags the length of the rod depends on the relative magnitudes of the bulk and shear loss angles. In the situation when the two loss angles  $\phi_B$  and  $\phi_S$  are equal to each other, the Poisson ratio is real, and we only need to deal with one loss angle  $\phi_Y$ —although there is reason to assume the equality of these two angles.

If the coating material is made into the shape of a one-dimensional rod, and if we only consider its elongational, bending or torsional modes, then the Young's modulus is the appropriate elastic modulus associated with these modes, and  $\phi_Y$  is the appropriate loss angle to apply. However, this is not directly relevant for coating thermal noise. An elastic modulus that will actually prove useful is that of the *two-dimensional (2-D) flexural rigidity* of a thin plate made from the coating material,

$$D = \frac{Yh^3}{12(1 - \sigma^2)} = |D|(1 + i\phi_D) \quad (2.55)$$

where  $h$  is the thickness of the plate, with

$$\phi_D = \frac{(1 - \sigma - 2\sigma^2)\phi_B + 2(1 - \sigma + \sigma^2)\phi_S}{3(1 - \sigma)}. \quad (2.56)$$

As we shall see in Sec. 2.7.1, this  $D$  is most easily measured through the quality factor of drum modes of a thinly coated sample—although this will not turn out to be the combination of loss angle that appear in the thermal noise.

### 2.3.3 Thermal Noise of a Mirror Coated with one Thin Layer

In the case where the coating thickness is much less than the size of the mirror substrate and the beam spot size, the elastic deformation of the substrate is not affected by the presence of the coating. As a consequence, if we include the elastic energy stored in the substrate  $U_{\text{sub}}$  with loss angle  $\phi_{\text{sub}}$ ,

we can write

$$\begin{aligned} W_{\text{diss}} &= \phi_{\text{sub}}U_{\text{sub}} + \phi_B U_B + \phi_S U_S \\ &\approx \left[ \phi_{\text{sub}} + \phi_B \frac{U_B}{U_{\text{sub}}} + \phi_S \frac{U_S}{U_{\text{sub}}} \right] U_{\text{sub}}. \end{aligned} \quad (2.57)$$

With the assumption of thin coating and half-infinite substrate, the total strain energy stored in the sample can be considered as  $U_{\text{sub}}$ . In such a way the coating adds on to substrate loss angle as additional, effective angles

$$\phi_{\text{coated}} = \phi_{\text{sub}} + \frac{U_B}{U_{\text{sub}}}\phi_B + \frac{U_S}{U_{\text{sub}}}\phi_S. \quad (2.58)$$

Note that when the total coating thickness  $l$  is much less than beam spot size  $w_0$ , we have  $U_B/U_{\text{sub}} \sim U_S/U_{\text{sub}} \sim l/w_0 \ll 1$ . Unfortunately, however,  $\phi_B$  and  $\phi_S$  are found to be so much larger than the substrate loss angle  $\phi_{\text{sub}}$  that in practice coating thermal noise still dominates over substrate thermal noise.

Now suppose we would like to measure a weighted average of the position of the mirror surface,

$$q = \bar{\xi} = \int d^2\vec{x} w(\vec{x})z(\vec{x}) \quad (2.59)$$

with [cf. Eq. (2.37)]

$$w(\vec{x}) = \frac{I(\vec{x})}{\int I(\vec{x})d^2\vec{x}} \quad (2.60)$$

and  $z(\vec{x})$  the position of the coating-air interface at transverse location  $\vec{x}$ .

According to Sec. 2.3.1, we need to apply a pressure profile of

$$f(\vec{x}) = F_0 w(\vec{x}) \quad (2.61)$$

onto the upper surface of the coating, which we shall also refer to as the coating-air interface. Straightforward calculations give

$$\frac{U_B}{F_0^2} = \frac{(1-2\sigma_c)l}{3} \left[ \frac{Y_c (1-2\sigma_s)^2 (1+\sigma_s)^2}{Y_s^2 (1-\sigma_c)^2} + \frac{1}{Y_s} \frac{2(1-2\sigma_s)(1+\sigma_s)(1+\sigma_c)}{(1-\sigma_c)^2} + \frac{1}{Y_c} \frac{(1+\sigma_c)^2}{(1-\sigma_c)^2} \right] \int w^2(\vec{x}) d^2\vec{x} \quad (2.62)$$

$$\frac{U_S}{F_0^2} = \frac{2l}{3} \left[ \frac{Y_c (1-\sigma_c + \sigma_c^2)(1+\sigma_s)^2 (1-2\sigma_s)^2}{Y_s^2 (1-\sigma_c)^2 (1+\sigma_c)} - \frac{(1+\sigma_c)(1-2\sigma_c)(1-2\sigma_s)(1+\sigma_s)}{Y_s (1-\sigma_c)^2} + \frac{(1-2\sigma_c)^2 (1+\sigma_c)}{Y_c (1-\sigma_c)^2} \right] \int w^2(\vec{x}) d^2\vec{x}. \quad (2.63)$$

Here  $l$  is coating thickness; for Young's modulus  $Y$  and Poisson's ratio  $\sigma$ , substrates  $c$  and  $s$  represent coating and substrate, respectively. Directly following Eqs. (2.46) and (2.50) will give rise to a noise spectrum of

$$S_{\xi} = \frac{4k_B T}{\pi f} \left[ \phi_B \frac{U_B}{F_0^2} + \phi_S \frac{U_S}{F_0^2} \right] \quad (2.64)$$

where  $U_B/F_0^2$  and  $U_S/F_0^2$  are given by Eqs. (2.62) and (2.63), respectively.

Here we can define

$$\int w^2(\vec{x}) d^2\vec{x} = \frac{\int d^2\vec{x} I^2(\vec{x})}{[\int d^2\vec{x} I(\vec{x})]^2} \equiv \frac{1}{\mathcal{A}_{\text{eff}}} \quad (2.65)$$

as the inverse of an *effective beam area*. Therefore noise power in  $q$  is proportional to coating thickness and inversely proportional to beam area. In particular, for a Gaussian beam with

$$I(\vec{x}) \propto \exp\left(-\frac{\vec{2}x^2}{w_0^2}\right) \quad (2.66)$$

the effective area is  $\mathcal{A}_{\text{eff}} = \pi w_0^2$ .

Let us compare our results to previous calculations using  $\phi_{\perp}$  and  $\phi_{\parallel}$ . As it turns out, if we assume  $\phi_S = \phi_B$ , then formulas for thermal noise agree with Eq. (22) in Ref. [11]. To illustrate the different roles now played by  $\phi_B$  and  $\phi_S$ , let us take the very simple case of  $Y = Y_c = Y_s$  and  $\sigma = \sigma_c = \sigma_s$ , where

$$\frac{\delta U_B}{F_0^2} = \frac{4l}{3Y\mathcal{A}_{\text{eff}}} (1+\sigma)^2 (1-2\sigma) \quad (2.67)$$

$$\frac{\delta U_S}{F_0^2} = \frac{2l}{3Y\mathcal{A}_{\text{eff}}} (1+\sigma)(1-2\sigma)^2. \quad (2.68)$$

Using Eq. (2.64), we can get the power spectral density of the single-layer nonpenetration coating

thermal noise as

$$\begin{aligned} S_{\xi}(f) \\ = \frac{8k_B T(1 - \sigma - 2\sigma^2)l}{3\pi f Y \mathcal{A}_{\text{eff}}} [2(1 + \sigma)\phi_B + (1 - 2\sigma)\phi_S]. \end{aligned} \quad (2.69)$$

From Eq. (2.69), we can see that the bulk loss and shear loss contribute differently to the total noise. More importantly, at least in this very simple case of  $Y_c = Y_s$ , the combination of  $\phi_B$  and  $\phi_S$ , approximately  $2\phi_B + \phi_S$ , that enters the thermal noise apparently differs significantly from the combination  $\phi_{\text{tot}} \approx \phi_B + 2\phi_S$ , which has been measured by ring-down experiments that have been performed so far [15–17]—as we will see in Eq. (2.110) and will be discussed in detail in the rest of Sec. 2.7.

### 2.3.4 Discussions on the Correlation Structure of Thermal Noise

Before proceeding to more detailed calculations of Brownian noise that involve light penetrating into the coating layers, we would like to gain more insight about thermal noise by inspecting our existing expressions of coating thermal noise [Eqs. (2.62)–(2.64)] more carefully. We note that

$$S_{\xi} \propto l \int w^2(\vec{x}) d^2\vec{x}. \quad (2.70)$$

where the coefficient of proportionality depends only on material property. From such a dependence on coating and beam geometries, we deduce that (i) each point on the coating-air interface fluctuates along the  $z$  direction independently, and (ii) materials at different  $z$ 's within the coating also contribute independently to coating thermal noise. These observations will be confirmed mathematically in the next section.

Finally, within the coefficient of proportionality [cf. Eqs. (2.62) and (2.63)], we found three types of dependence on the Young's moduli of the coating and substrate materials: terms proportional to  $1/Y_c$  are expected to arise from fluctuations in coating thickness, terms proportional to  $Y_c/Y_s^2$  can be interpreted as arising from coating thermal stresses driving the substrate-coating interface, while terms proportional to  $1/Y_s$  are therefore interpreted as correlations between the above two types of noise.

## 2.4 Cross Spectra of Thermal Noise Components

In this section, we compute the cross spectra of each component of coating thermal noise, and assemble the formula for the spectral density of the total noise. Specifically, in Sec. 2.4.1, we compute the cross spectra of the thickness fluctuations any two uniform sublayers of the coating,

and obtain the cross spectrum of  $S_{zz}$ ; in Sec. 2.4.2, we compute the cross spectra involving height fluctuation  $z_s$  of the coating-substrate interface, i.e.,  $S_{S_{zz}z_s}$  and  $S_{z_s z_s}$ ; in Sec. 2.4.3, we dissect the above results and analyze the separate roles of bulk and shear fluctuations; in Sec. 2.4.4, we write down the full formula of coating thermal noise.

### 2.4.1 Coating-Thickness Fluctuations

Let us start by calculating thickness fluctuations of individual layers and correlations among them. Following Levin's approach, we imagine applying two pairs of opposite pressure,

$$f_1(\vec{x}) = F_0 w_1(\vec{x}), \quad f_3(\vec{x}) = F_0 w_3(\vec{x}) \quad (2.71)$$

in the  $z$  direction on layer I and layer III, as shown in Fig. 2.2, with thickness of  $l_1$  and  $l_3$ , respectively. Here  $w_1(\vec{x})$  and  $w_3(\vec{x})$ , like the  $w(\vec{x})$  used in Eq. (2.59), provides the shape of the pressure profiles.

We assume that within each of I and III, there is only one type of material, yet there could be arbitrary number of different material sub layers in II. As it will turn out, the precise locations of layers I and III along the  $z$  direction does not affect the result, *as long as they do not overlap*, or in other words, layer II has nonzero (positive) thickness.

Throughout this paper, we shall assume that the beam spot size is much less than the radius of the mirror, so that we can make the approximation that the mirror surface is an infinite two-dimensional plane. In this case, we perform a spatial Fourier transformation for the applied pressure,

$$\tilde{f}_j(\vec{k}) = \int e^{i\vec{k}\cdot\vec{x}} f_j(\vec{x}) d^2\vec{x} = F_0 \tilde{w}_j(\vec{k}), \quad j = 1, 3, \quad (2.72)$$

and carry out our calculations for strain and stress distributions in the coating-substrate system in the Fourier domain.

We further assume that the coating thickness is much less than the beam spot size, which is inverse the maximum spatial frequency contained in  $\tilde{w}_{1,3}$ . This means we only need to consider  $\vec{k}$ 's with  $|\vec{k}|l \ll 1$ , with  $l$  the total coating thickness. According to calculations of Appendix 2.10, nonzero components of the stress and strain tensors in Layers I and III are found to be (in the spatial Fourier domain)

$$\tilde{T}_{xx}^I = \tilde{T}_{yy}^I = \frac{\sigma_1 \tilde{w}_1}{1 - \sigma_1} F_0, \quad \tilde{T}_{zz}^I = \tilde{w}_1 F_0, \quad (2.73)$$

$$\tilde{S}_{zz}^I = -\frac{(1 - 2\sigma_1)(1 + \sigma_1)\tilde{w}_1}{Y_1(1 - \sigma_1)} F_0, \quad (2.74)$$

and

$$\tilde{T}_{xx}^{III} = \tilde{T}_{yy}^{III} = \frac{\sigma_3 \tilde{w}_3}{1 - \sigma_3} F_0, \quad \tilde{T}_{zz}^{III} = \tilde{w}_3 F_0, \quad (2.75)$$

$$\tilde{S}_{zz}^{\text{III}} = -\frac{(1-2\sigma_3)(1+\sigma_3)\tilde{w}_3}{Y_3(1-\sigma_3)}F_0, \quad (2.76)$$

respectively.

Note that deformations within layer I only depend on  $\tilde{w}_1$  (not  $\tilde{w}_3$ ), while deformations within layer III only depend on  $\tilde{w}_3$  (not  $\tilde{w}_1$ )—while regions outside these layers are found to have vanishing strain and stress. This means we can treat deformations caused by each pair of forces independently, as long as layer I and layer III do not overlap. The deformations are also independent from the thickness of the layers. The vanishing of deformations outside these layers means that when we introduce additional pairs of opposite forces, the new deformations introduced will be constrained within those new layers—as long as those new layers do not overlap with existing ones. This independence originates from the linearity of elastic response, and the fact that coating strains induced by force applied on a single surface within the coating, as discussed in Appendix.2.10, does not depend on distance away from that surface, as seen in Eqs. (2.159)–(2.166). The situation here is analogous to the electric field generated by several pairs of oppositely charged infinite parallel planes.

In terms of thermal noise, such a distribution of elastic deformations corresponds to a dissipation energy that consists of two independent terms, each corresponding to one layer and proportional to its thickness:

$$\frac{W_{\text{diss}}}{F_0^2} = W_{11}l_1 \int w_1^2 d^2\vec{x} + W_{33}l_3 \int w_3^2 d^2\vec{x}. \quad (2.77)$$

Here we have defined, for  $J = 1, 3$ :

$$W_{jj} \equiv \frac{(1-2\sigma_j)(1+\sigma_j)}{3(1-\sigma_j)^2 Y_j} \left[ \frac{1+\sigma_j}{2} \phi_B^j + (1-2\sigma_j)\phi_S^j \right]. \quad (2.78)$$

This means the fluctuation of

$$q \equiv \int [w_1(\vec{x})\delta l_1(\vec{x}) + w_3(\vec{x})\delta l_3(\vec{x})] d^2\vec{x} \quad (2.79)$$

is given by

$$S_q = \frac{4k_B T}{\pi f} \sum_{J=1,3} \left[ W_{jj} l_j \int w_j^2(\vec{x}) d^2\vec{x} \right]. \quad (2.80)$$

The absence of cross terms here means that fluctuations in  $\delta l_1(\vec{x})$  and  $\delta l_3(\vec{x}')$  are uncorrelated—and hence statistically independent. Furthermore, within each layer, in the same spirit as the discussions in Sec. 2.3.4, the particular form of dependence on  $l_j$  and  $w_j(\vec{x})$  indicates that  $S_{zz}$  fluctuations at different 3-D locations (within this layer) are all uncorrelated and have the same spectrum. In this way, we obtain the cross spectral density of  $S_{zz}$  at two arbitrary 3-D locations within the coating:

$$S_{S_{zz}S_{zz}}^{ij}(\vec{x}, z; \vec{x}', z') = \frac{4k_B T}{\pi f} \delta_{ij} \delta^{(2)}(\vec{x} - \vec{x}') \delta(z - z') W_{jj}. \quad (2.81)$$

Here we have assumed that  $(\vec{x}, z)$  belongs to layer  $i$ , while  $(\vec{x}', z')$  belongs to layer  $j$ . (The association to layers helps to identify the material property to be used in  $W_{jj}$ .)

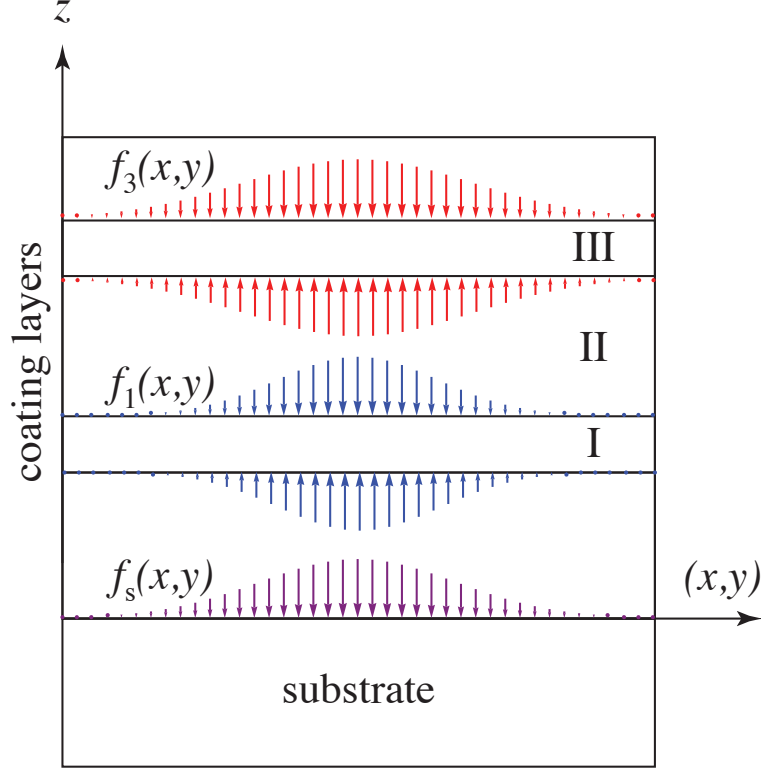


Figure 2.2: Illustrations of forces applied onto various interfaces within the coating. Each of Layers I and III in the coating are assumed to be uniform (but they might each contain a different kind of material); region II denotes the entire gap between them, which may well contain many different dielectric layers. A pair of force distribution  $f_1$  ( $f_3$ ) in opposite directions is exerted on opposite sides of Layer I (III), while  $f_s$  is exerted on the coating-substrate interface. The three distributions may well have different profiles (as also illustrated in the figure).

#### 2.4.2 Fluctuations of Coating-Substrate Interface and Their Correlations with Coating Thickness

To investigate the correlation between height of the coating-substrate thickness,  $z_s(\vec{x})$  and the thickness of each coating layer,  $\delta l_j(\vec{x})$ , we apply a pair of pressures  $f_1(\vec{x}) = F_0 w_1(\vec{x})$  at opposite sides of Layer I, and force  $f_s(x, y) = F_0 w_s(\vec{x})$  onto the coating-substrate interface (along the  $-z$  direction), as shown in Fig. 1. The same strain and stress as in Eqs. (2.73) and (2.74) are driven by  $\tilde{f}_1$ , which are only nonvanishing within layer I. On the other hand,  $\tilde{f}_s$  drives uniform strain and stress over

the entire coating, with nonvanishing components of stress and strain given by,

$$\|\tilde{T}_{ij}\| = \frac{\tilde{w}_s(1 - \sigma_s - 2\sigma_s^2)Y_c}{(1 + \sigma_c)\kappa^2 Y_s} \begin{bmatrix} \frac{k_x^2 + \sigma_c k_y^2}{1 - \sigma_c} & k_x k_y & 0 \\ k_x k_y & \frac{\sigma_c k_x^2 + k_y^2}{1 - \sigma_c} & 0 \\ 0 & 0 & 0 \end{bmatrix} \quad (2.82)$$

$$\|\tilde{S}_{ij}\| = -\frac{\tilde{w}_s(1 - \sigma_s - 2\sigma_s^2)}{\kappa^2 Y_s} \begin{bmatrix} k_x^2 & k_x k_y & \\ k_x k_y & k_y^2 & \\ & & \frac{-\sigma_c}{1 - \sigma_c} \end{bmatrix}, \quad (2.83)$$

where Young's modulus  $Y_c$  and Poisson's ratio  $\sigma_c$  of the coating are given by values within layer I. The total dissipation in this case will have the following structure,

$$\frac{W_{\text{diss}}}{F_0^2} = l_1 \left[ W_{11} \int w_1^2 d^2 \vec{x} + 2W_{1s} \int w_1 w_s d\vec{x} + W_{ss} \int w_s^2 d^2 \vec{x} \right], \quad (2.84)$$

with the first term arising from dissipation in layer I that is due to strain and stress driven by  $f_1$ , the second term also arising from dissipation in layer I arising from cross terms between strains and stresses caused by  $f_1$  and  $f_s$ , and the third term arises from dissipations throughout the entire coating, due to strain and stress caused by  $f_s$ . Here  $W_{11}$  is the same as defined by Eq. (2.78), and

$$W_{js} = \frac{(1 - \sigma_s - 2\sigma_s^2)(1 - \sigma_j - 2\sigma_j^2)}{2(1 - \sigma_j)^2 Y_s} (\phi_B^j - \phi_S^j) \quad (2.85a)$$

$$W_{ss}^{(j)} = \frac{(1 - \sigma_s - 2\sigma_s^2)^2 Y_j}{(1 - \sigma_j)^2 Y_s^2} \left[ \frac{1 - 2\sigma_j}{2} \phi_B^j + \frac{1 - \sigma_j + \sigma_j^2}{1 + \sigma_j} \phi_S^j \right]. \quad (2.85b)$$

Note that we have added a superscript ( $j$ ) for  $W_{ss}$  to indicate that here the dissipation is due to force applied on one thin layer alone.

Here again, the dependences on  $w_1^2$  and  $w_s^2$  indicate that fluctuations at different transverse locations,  $\vec{x} \neq \vec{x}'$ , are uncorrelated, while the  $l_1$  in front of  $W_{11}$ , and the arbitrariness of  $l_1$  means that  $S_{zz}$  fluctuations at different  $z$  locations within the thin layers are uncorrelated. The  $l_1$  in front of both  $W_{1s}$  and  $W_{ss}$  indicates that all  $S_{zz}$  within layer I are correlated with  $z_s$  the same way, even though all of them are mutually uncorrelated.

This allows us to extract the following

$$S_{z_s z_s}(\vec{x}, \vec{x}') = \frac{4k_B T}{3\pi f} \delta^{(2)}(\vec{x} - \vec{x}') \sum_j l_j W_{ss}^{(j)} \quad (2.86a)$$

$$S_{S_{zz} z_s}(\vec{x}; \vec{x}', z') = \frac{4k_B T}{3\pi f} \delta^2(\vec{x} - \vec{x}') W_{js}. \quad (2.86b)$$

Here for Eq. (2.86b),  $j$  is the layer with which  $z'$  is associated; and this labeling is to help identify which material parameter to use in  $W_{js}$ .

### 2.4.3 The Anatomy of Coating Thermal Noise

Here let us assemble Eqs. (2.81), (2.86a) and (2.86b) from the previous sections, and write:

$$S_{S_{zz}S_{zz}}^{ij}(\vec{x}, z; \vec{x}', z') = \frac{4k_B T (1 + \sigma_j)(1 - 2\sigma_j)}{3\pi f Y_j (1 - \sigma_j)^2} \left[ \frac{1 + \sigma_j}{2} \phi_{Bj} + (1 - 2\sigma_j) \phi_{Sj} \right] \delta_{ij} \delta^{(2)}(\vec{x} - \vec{x}') \delta(z - z') \quad (2.87a)$$

$$S_{z_s z_s}(\vec{x}, \vec{x}') = \frac{4k_B T (1 - \sigma_s - 2\sigma_s^2)^2}{3\pi f Y_s^2} \sum_j \frac{Y_j l_j}{(1 - \sigma_j)^2} \left[ \frac{1 - 2\sigma_j}{2} \phi_{Bj} + \frac{1 - \sigma_j + \sigma_j^2}{1 + \sigma_i} \phi_{Sj} \right] \delta^{(2)}(\vec{x} - \vec{x}') \quad (2.87b)$$

$$S_{z_s S_{zz}}(\vec{x}; \vec{x}', z') = \frac{2k_B T (1 - \sigma_s - 2\sigma_s^2)(1 - \sigma_j - 2\sigma_i^2)}{3\pi f Y_s (1 - \sigma_j)^2} [\phi_{Bj} - \phi_{Sj}] \delta^2(\vec{x} - \vec{x}'). \quad (2.87c)$$

Here we have assumed that  $z$  belongs to the  $i$ -th layer and that  $z'$  belongs to the  $j$ -th layer, respectively. The thickness fluctuation of different layers are mutually independent [note the Kronecker delta in Eq. (2.87a)], while thickness fluctuation of each layer is correlated with the height fluctuation of the coating-substrate interface [Eq. (2.87c)].

Fluctuations described by Eqs. (2.87a)–(2.87b) can be seen as driven by a set of microscopic fluctuations throughout the coating. Suppose we have  $3N$  thermal noise fields (i.e., 3 for each coating layer),  $n_j^B(\mathbf{x})$ ,  $n_j^{S_A}(\mathbf{x})$  and  $n_j^{S_B}(\mathbf{x})$ , all independent from each other, with

$$S_{n_j^B n_k^B} = \frac{4k_B T (1 - \sigma_j - 2\sigma_j^2)}{3\pi f Y_j (1 - \sigma_j)^2} \phi_B^j \delta_{jk} \delta^{(3)}(\mathbf{x} - \mathbf{x}'), \quad (2.88a)$$

$$S_{n_j^{S_A} n_k^{S_A}} = S_{n_j^{S_B} n_k^{S_B}} = \frac{4k_B T (1 - \sigma_j - 2\sigma_j^2)}{3\pi f Y_j (1 - \sigma_j)^2} \phi_S^j \delta_{jk} \delta^{(3)}(\mathbf{x} - \mathbf{x}'), \quad (2.88b)$$

and all other cross spectra vanishing. Here  $j$  labels coating layer, the superscript  $B$  indicates bulk fluctuation, while  $S_A$  and  $S_B$  label two types of shear fluctuations. The normalization of these fields are chosen such that each of these fields, when integrated over a length  $l_j$  along  $z$ , have a noise spectrum that is roughly the same magnitude as a single-layer thermal noise.

Noise fields  $n_j^B(\mathbf{x})$ ,  $n_j^{S_A}(\mathbf{x})$  and  $n_j^{S_B}$  can be used to generate thickness fluctuations of the layers and the interface fluctuation (2.87a)–(2.87b) if we define

$$u_{zz}(\vec{x}, z) = C_j^B n_j^B(\vec{x}, z) + C_j^{S_A} n_j^{S_A}(\vec{x}, z) \quad (2.89)$$

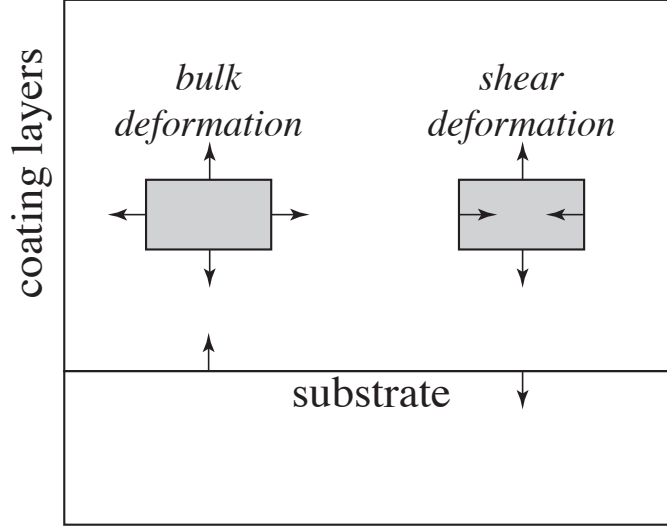


Figure 2.3: Illustration of the correlations between coating thickness  $\delta l_j$  and the height of the coating-substrate interface,  $z_s$ . On the left, for a bulk deformation: when a coating element is expanding, its expansion along the  $x$ - $y$  plane lifts the coating-substrate interface upwards, causing additional motion of the coating-air interface correlated to that caused by the increase in coating thickness. On the right, a particular shear mode: when a coating element is expanding, its contraction along the  $x$ - $y$  plan pushes the coating-substrate interface downwards, causing addition motion of the coating-air interface anticorrelated to that caused by the increase in coating thickness.

	Thickness ( $\delta_j$ )	Surface height ( $z_s$ )
Bulk	$C_j^B = \sqrt{\frac{1 + \sigma_j}{2}}$	$D_j^B = \frac{1 - \sigma_s - 2\sigma_s^2 Y_j}{\sqrt{2(1 + \sigma_j)} Y_s}$
Shear A	$C_j^{SA} = \sqrt{1 - 2\sigma_j}$	$D_j^{SA} = -\frac{1 - \sigma_s - 2\sigma_s^2 Y_j}{2\sqrt{1 - 2\sigma_j} Y_s}$
Shear B	(none)	$D_j^{SB} = \frac{\sqrt{3}(1 - \sigma_j)(1 - \sigma_s - 2\sigma_s^2) Y_j}{2\sqrt{1 - 2\sigma_j}(1 + \sigma_j) Y_s}$

Table 2.1: Transfer functions from bulk and shear noise fields to layer thickness and surface height

and

$$z_s(\vec{x}) = \sum_j \int_{L_{j+1}}^{L_j} dz \left[ D_j^B n_j^B(\vec{x}, z) + D_j^{SA} n_j^{SA}(\vec{x}, z) + D_j^{SB} n_j^{SB}(\vec{x}, z) \right]. \quad (2.90)$$

For each coating layer,  $C_j^B$  and  $D_j^B$  are transfer functions from the bulk noise field  $n_j^B$  to its own thickness  $\delta l_j$  and to surface height  $z_s$ , respectively;  $C_j^{SA}$  and  $D_j^{SA}$  are transfer functions from the first type of shear noise to thickness and surface height; finally  $D_j^{SB}$  is the transfer function from the second type of shear noise to surface height (note that this noise field does not affect layer thickness). Explicit forms of these transfer functions are listed in Table. 2.1.

Equations (2.89) and (2.90) owe their simple forms to the underlying physics of thermal fluctuations:

For *bulk noise*, i.e., terms involving  $n_j^B$ , the form of Eqs. (2.89) and (2.90) indicates that the interface fluctuation due to bulk dissipation is simply a sum of pieces that are directly proportional to the bulk-induced thickness fluctuations of each layer. This means the thermal bulk stress in a layer drive simultaneously the thickness fluctuation of that layer and a fluctuation of the coating-substrate interface. The fact that  $D_j^B$  and  $C_j^B$  having the same sign means that when thickness increases, the interface also rises (with intuitive explanation shown in Figure 2.3). This sign of correlation is generally unfavorable because the two noises add constructively towards the rise of the coating-air interface.

For *shear noise*, the situation is a little more complicated, because unlike bulk deformations, there are a total of 5 possible shear modes. From Eq. (2.73) and (2.74), it is clear that  $f_1$ , applied on opposites of Layer I (Figure 2.2), only drives the  $xx + yy - 2zz$  shear mode and the  $xx + yy + zz$  bulk mode, while from Eq. (2.82) and (2.83), the force distribution  $f_s$  drives three shear modes of  $xx - yy$ ,  $xy + yx$ , and  $xx + yy - 2zz$ . This means while thermal shear stresses in the  $xx + yy - 2zz$  mode drives layer thickness and interface fluctuation simultaneously, there are additional modes of shear stress,  $xx - yy$  and  $xy + yx$ , that only drives the interface without driving layer thickness. Our mode  $S_A$ , which drives both layer thickness and interface height, therefore corresponds to the physical shear mode of  $xx + yy - 2zz$ ; our mode  $S_B$ , which only drives interface height, corresponds to the joint effect of the physical shear modes  $xx - yy$  and  $xy + yx$ . It is interesting to note that for  $S_A$ , its contributions to  $\delta l_j$  and  $z_s$  are anti correlated, because  $C^{S_A}$  and  $D^{S_A}$  have opposite signs. This is intuitively explained in Fig. 2.3.

As an example application of Eqs. (2.89) and (2.90), if we ignore light penetration into the coating layers, namely, when thermal noise is equal to

$$\xi^{\text{np}} \equiv -z_s - \sum_j \delta l_j \quad (2.91)$$

we have

$$\begin{aligned} \xi^{\text{np}} = - \sum_j \int_{L_j}^{L_{j+1}} dz & \left[ (C_j^B + D_j^B) n_j^B \right. \\ & + (C_j^{S_A} + D_j^{S_A}) n_j^{S_A} \\ & \left. + D_j^{S_B} n_j^{S_B} \right] \end{aligned} \quad (2.92)$$

in which contributions from each layer has been divided into three mutually uncorrelated groups, each arising from a different type of fluctuations. Here we see explicitly that  $C^B$  and  $D^B$  sharing

the same sign increases contributions from  $n^B$ ;  $C^{SA}$  and  $D^{SA}$  having opposite signs suppresses contributions from  $n^{SA}$ .

Finally, we note that in the spectral density of  $\xi^{\text{np}}$ , contributions directly from coating thickness will be proportional to  $|C_j^B|^2$  and  $|C_j^{SA}|^2$ , and hence proportional to  $1/Y_c$ , those from interface height will be  $|D_j^B|^2$ ,  $|D_j^{SA}|^2$  and  $|D_j^{SB}|^2$ , and hence proportional to  $Y_c/Y_s^2$ , while those from correlations will be proportional to  $C_j^B D_j^B$  and  $C_j^{SA} D_j^{SA}$ , and hence proportional to  $1/Y_s$ . This confirms our anticipation at the end of Sec. 2.3.4.

#### 2.4.4 Full Formula for Thermal Noise

As we consider light penetration into the coating, we resort to Eq. (2.24), and write:

$$\begin{aligned} & \xi(\vec{x}) - i\zeta(\vec{x}) \\ &= - \sum_j \int_{z_{j+1}}^{z_j} dz \left\{ \left[ \left[ 1 + \frac{i\epsilon_j(z)}{2} \right] C_j^B + D_j^B \right] n_j^B(\vec{x}, z) \right. \\ & \quad + \left[ \left[ 1 + \frac{i\epsilon_j(z)}{2} \right] C_j^{SA} + D_j^{SA} \right] n_j^{SA}(\vec{x}, z) \\ & \quad \left. + D_j^{SB} n_j^{SB}(\vec{x}, z) \right\}. \end{aligned} \quad (2.93)$$

Here spectra of independent fields  $n_j^B$ ,  $n_j^{SA}$  and  $n_j^{SB}$  have been given in Eqs. (2.88a)–(2.88b),  $\epsilon$  is defined in Eq. (2.25), while the transfer functions  $C$ s and  $D$ s are listed in Table. 2.1.

We can then obtain the spectrum of phase noise (after averaging over the mirror surface, weighted by the power profile of the optical mode) as

$$\begin{aligned} S_{\bar{\xi}} &= \sum_j \int_{z_{j+1}}^{z_j} \frac{dz}{\lambda_j} \left[ \left[ 1 - \text{Im} \frac{\epsilon_j(z)}{2} \right] C_j^B + D_j^B \right]^2 S_j^B \\ &+ \sum_j \int_{z_{j+1}}^{z_j} \frac{dz}{\lambda_j} \left[ \left[ 1 - \text{Im} \frac{\epsilon_j(z)}{2} \right] C_j^{SA} + D_j^{SA} \right]^2 S_j^S \\ &+ \sum_j \left[ D_j^{SB} \right]^2 \frac{l_j}{\lambda_j} S_j^S \\ &\equiv \sum_j q_j^B S_j^B + q_j^S S_j^S \end{aligned} \quad (2.94)$$

and spectrum of amplitude noise as

$$\begin{aligned} S_{\bar{\zeta}} &= \sum_j \int_{z_{j+1}}^{z_j} \frac{dz}{\lambda_j} \left\{ \left[ C_j^B \text{Re} \frac{\epsilon_j(z)}{2} \right]^2 S_j^B \right. \\ & \quad \left. + \left[ C_j^{SA} \text{Re} \frac{\epsilon_j(z)}{2} \right]^2 S_j^S \right\}. \end{aligned} \quad (2.95)$$

Here  $\lambda_j$  is the wavelength of light in Layer  $j$ , and we have defined

$$S_j^X \equiv \frac{4k_B T \lambda_j \phi_X^j (1 - \sigma_j - 2\sigma_j^2)}{3\pi f Y_j (1 - \sigma_j)^2 \mathcal{A}_{\text{eff}}}, \quad X = B, S. \quad (2.96)$$

which is at the level of coating thickness fluctuation of a single layer of dielectrics with material parameters identical to layer  $j$  and length equal to  $\lambda_j$ . Note that the quantity  $S_j^X$  only depends on the material properties (and temperature) of the layer, and is independent from length of that layer; the quantities  $q_j^X$ , on the other hand, give us the relative thermal-noise contribution of each layer in a dimensionless way.

Note that the reason for keeping the integrals in Eqs. (2.94) and (2.95) is because  $\epsilon$  has a  $z$  dependence, which originates from the fact that the back-scattering contributions to  $\delta\phi_j$ 's and  $\delta r_j$ 's a weighted integral of  $u_{zz}$  within each layer [cf. (2.17) and (2.18)].

## 2.5 Effect of Light Penetration into the Coating

In this section, we synthesize results from Sec. 2.2 and Sec. 2.4, and compute the full Brownian thermal noise for coating configurations. We will illustrate how the light penetration affects the total noise in highly reflective coatings.

### 2.5.1 Optics of Multilayer Coatings

For completeness of the paper, we briefly review how light penetration coefficient  $\partial \log \rho / \partial \phi_j$  can be calculated.

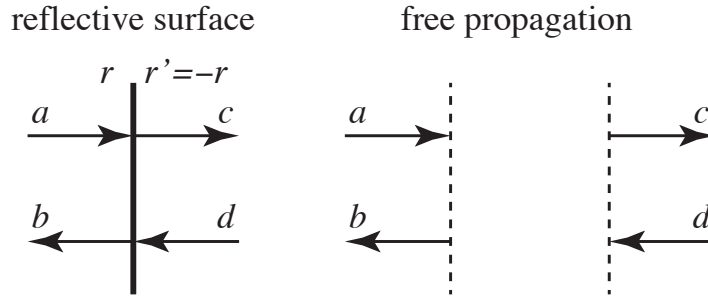


Figure 2.4: Two basic transformations involved in solving for optical fields in a multilayer coating

From an interface from layer  $i$  to  $j$  (here  $j$  is either  $i + 1$  or  $i - 1$ ), we denote the reflectivity and transmissivity of different layers by  $r_{ij}$  and  $t_{ij}$ :  $r_{ij}^2 + t_{ij}^2 = 1$ .

$$r_{ij} = \frac{n_i - n_j}{n_i + n_j}. \quad (2.97)$$

Parameter	Tantala( $\text{Ti}_2\text{O}_5$ )	Silica( $\text{SiO}_2$ )
Refractive index	2.07 [18]	1.45 [18]
Poisson's ratio	0.23 [19]	0.17 [19]
Young's modulus (Pa)	$1.4 \times 10^{11}$ [20]	$7 \times 10^{10}$ [19]
Loss angle ( $\phi_B = \phi_S$ )	$2.3 \times 10^{-4}$ [21]	$4.0 \times 10^{-5}$ [22]
Photoelastic coefficient	-0.50 [23]	-0.41 [24]

Table 2.2: Baseline material parameters

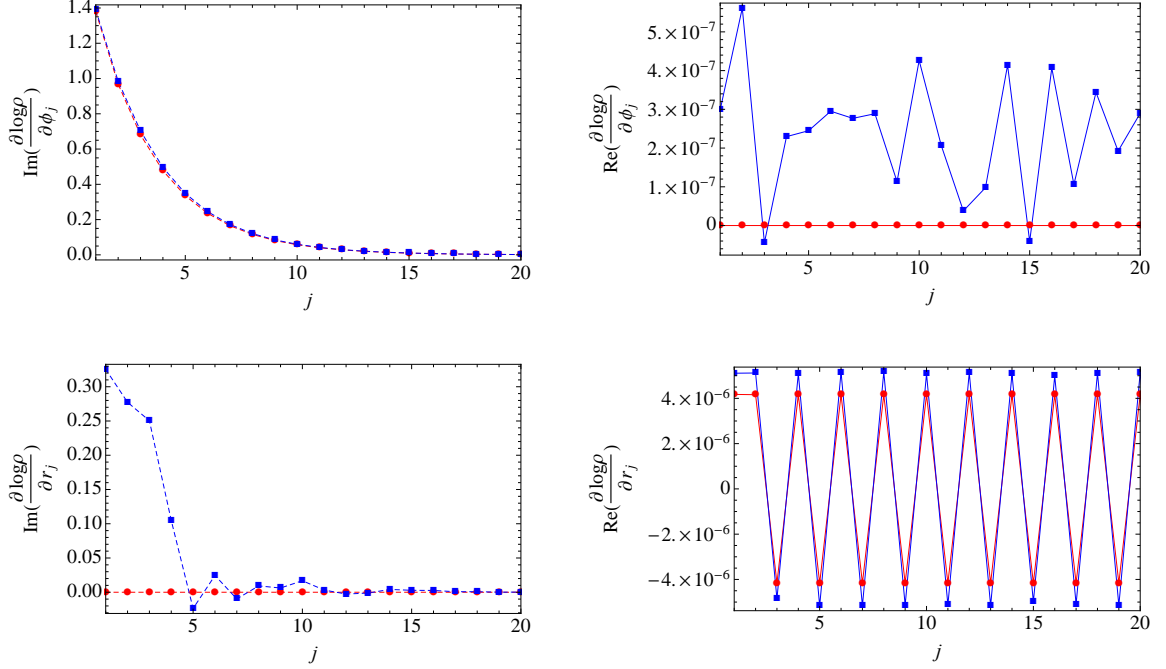


Figure 2.5: Real (solid curves) and imaginary (dashed curves) parts of  $\partial \log \rho / \partial \phi_j$  (upper panel) and  $\partial \log \rho / \partial r_j$  (lower panel), for conventional (red curve) and Advanced LIGO (blue curve) coatings. [Note that  $\text{Re}(\partial \log \rho / \partial \phi_j) = 0$  for conventional coating.]

We also define  $n_{N+1} = n_1$ , since that is the refractive index of the substrate.

A matrix approach can be applied to solve for the amplitude of light inside the layers, when we view the coating as made up from two elementary transformations, each representable by a matrix. In this approach, instead of writing out-going fields in terms of in-going fields, one write fields to the right of an optical element in terms of those to the left. As illustrated in Figure 2.4, for reflection at an interface (left panel), we write

$$\begin{bmatrix} c \\ d \end{bmatrix} \equiv \mathbf{R}_r = \frac{1}{t} \begin{bmatrix} 1 & -r \\ -r & 1 \end{bmatrix} \begin{bmatrix} a \\ b \end{bmatrix}. \quad (2.98)$$

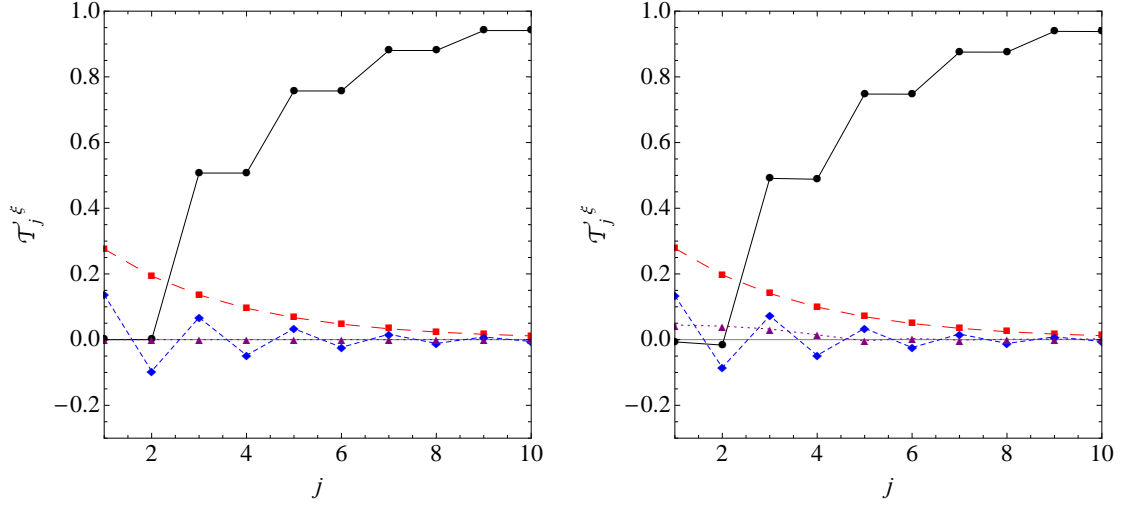


Figure 2.6: Light penetration into the first 10 layers of a 38-layer coating (left panel for conventional coating and right panel for Advanced LIGO coating). We plot the non-photoelastic part of  $\mathcal{T}_j$  in black solid curves, the photoelastic part of  $\mathcal{T}_j^s$  in long-dashed red curves, as well as  $\mathcal{T}_j^s$  (scaled by rms value of  $\delta l_j^c$  with respect to the rms value of  $\delta l_j$ , shown in short-dashed blue curves) and  $\mathcal{T}_j^s$  (scaled by rms value of  $\delta l_j^s$ , shown in dotted purple curves). These plots indicate that for both structures, light penetration is restricted within the first 10 layers.

On the other hand, for propagation across a gap with phase shift  $\phi$ , we have

$$\begin{bmatrix} c \\ d \end{bmatrix} \equiv \mathbf{T}_\phi = \begin{bmatrix} e^{i\phi} & \\ & e^{-i\phi} \end{bmatrix} \begin{bmatrix} a \\ b \end{bmatrix}. \quad (2.99)$$

In this way, assuming the input and output field amplitude at the top surface of a multi-layer coating to be  $v_1$  and  $v_2$ , and writing those right inside the substrate to be  $s_1$  and  $s_2$ , we have

$$\begin{bmatrix} s_1 \\ s_2 \end{bmatrix} = \begin{bmatrix} M_{11} & M_{12} \\ M_{21} & M_{22} \end{bmatrix} \begin{bmatrix} v_1 \\ v_2 \end{bmatrix} = \mathbf{M} \begin{bmatrix} v_1 \\ v_2 \end{bmatrix} \quad (2.100)$$

where  $\mathbf{M}$  is given by

$$\mathbf{M} = \mathbf{R}_{r_{N,N+1}} \mathbf{T}_{\phi_{N-1}} \mathbf{R}_{r_{N-1,N}} \cdots \mathbf{R}_{r_{12}} \mathbf{T}_{\phi_1} \mathbf{R}_{r_{01}}. \quad (2.101)$$

The complex reflectivity is given by

$$\rho = -M_{21}/M_{22}. \quad (2.102)$$

## 2.5.2 Levels of Light Penetration in advanced LIGO ETM Coatings

In advanced LIGO, the coating stack is made from two alternating layers of materials:  $\text{SiO}_2$  ( $n_1 = 1.45$ ) and  $\text{Ta}_2\text{O}_5$  ( $n_2 = 2.07$ ). Here we consider the end test-mass mirror (ETM). In order to achieve

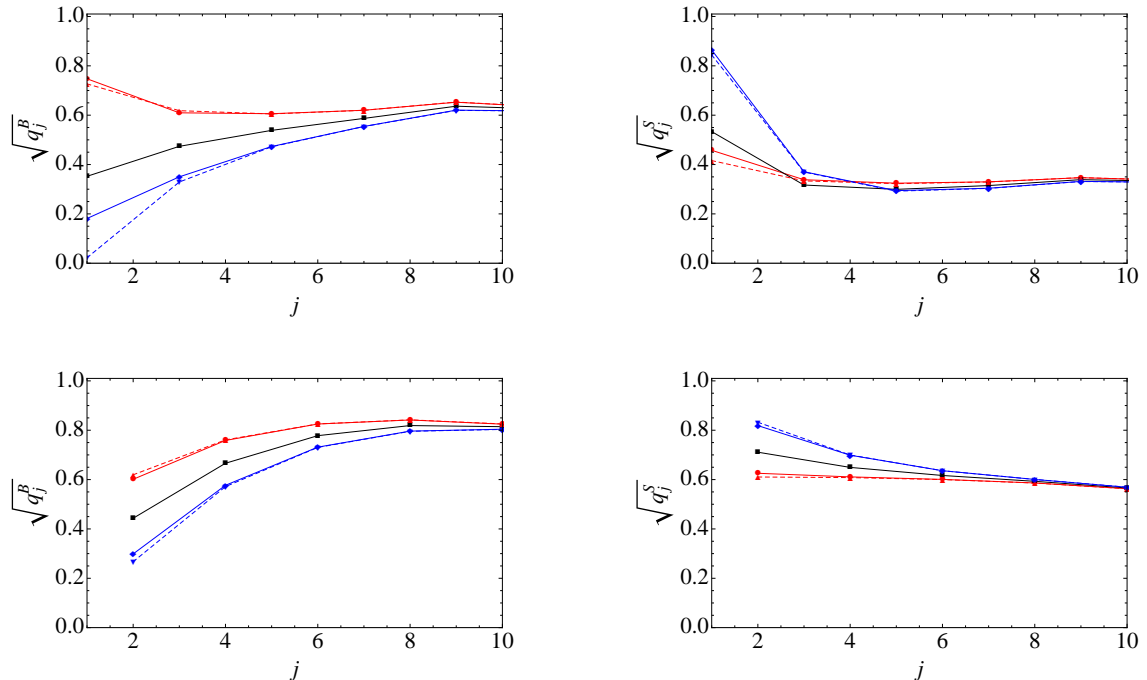


Figure 2.7: A break-down of thermal noise contributions from silica (upper panels) and tantalum (lower panels) layers, from bulk (left panels) and shear (right panels) losses. Blue curves correspond to  $\beta = -1$ , black  $\beta = 0$  and red  $\beta = 1$ . Dashed curves indicate results calculated without including back-scattering effects.

very high reflectivity, the coating is made of 19 successive pairs of alternating  $\text{SiO}_2$  and  $\text{Ta}_2\text{O}_5$  layers, all  $\lambda/4$  in thickness except the top one, which is  $\lambda/2$ . We will refer to this as the *conventional coating*. An alternative design has been made to allow the coating to operate at both 1064 nm and 532 nm. We shall refer to this as the *advanced LIGO coating* (see Appendix. 2.12) [25].

In Fig. 2.5, we plot real and imaginary parts of  $\partial \log \rho / \partial \phi_j$  and  $\partial \log \rho / \partial r_j$ , for both conventional and advanced LIGO coating. Here we note that the real parts of these derivatives are at the order of  $10^{-6}$ , which means  $\bar{\zeta}$  is less than  $\bar{\xi}$  by 6 orders of magnitude. This, together with considerations in Sec. 2.2.5, will make amplitude coating noise negligible.

In Eq. (2.27), we have divided contributions to  $\xi$  into four terms, the first,  $z_s$ , is the height of the coating-substrate interface, while the other three are related to fluctuations in layer thickness,  $\delta l_j$ ,  $\delta l_j^c$ , and  $\delta l_j^s$ , see Eqs. (2.27)–(2.30). We can illustrate the effect of light penetration by showing the relative size of these three contributions for each layer. In Figure 2.6, we carry out this illustration, for conventional coating on the left panel and for advanced LIGO coating on the right. We use a solid black line to indicate the nonphotoelastic part of  $\mathcal{T}_j^\xi$  [i.e., term not containing  $\beta_j$ , see Eq. (2.28)], and we use red-long-dashed, blue-short-dashed, and purple-dotted curves to indicate the photoelastic

part of  $\mathcal{T}_j^\xi$ ,  $\mathcal{T}_j^{\xi c} \sqrt{\langle(\delta l_j^c)^2\rangle/\langle(\delta l_j)^2\rangle}$  and  $\mathcal{T}_j^{\xi s} \sqrt{\langle(\delta l_j^s)^2\rangle/\langle(\delta l_j)^2\rangle}$ , respectively. The weighting factors,

$$\sqrt{\langle(\delta l_j^c)^2\rangle/\langle(\delta l_j)^2\rangle} = \frac{1}{\sqrt{2}} \sqrt{1 + \frac{\sin 4\phi_j}{4\phi_j}}, \quad (2.103)$$

$$\sqrt{\langle(\delta l_j^s)^2\rangle/\langle(\delta l_j)^2\rangle} = \frac{1}{\sqrt{2}} \sqrt{1 - \frac{\sin 4\phi_j}{4\phi_j}}, \quad (2.104)$$

have been added for  $\mathcal{T}_j^{\xi c}$  and  $\mathcal{T}_j^{\xi s}$ , respectively, to correct for the fact that  $\delta l_j^c$  and  $\delta l_j^s$  have different r.m.s. values compared to  $\delta l$ . Because of the lack of experimental data, we have assumed  $\beta_j = -0.4$  identically. Note that in order to focus on the effect of light penetration, we have only shown the first 10 layers.

In the figure, the effect of light penetration into the coating layers is embodied in the deviation of the black solid curve from unity in the first few layers, and in the existence of the other curves. Although we cannot perceive the correlation between these contributions, we can clearly appreciate that only the first few layers are penetrated, and that the total effect of light penetration will be small. We should also expect the effect of photoelasticity (dashed curves) to be small, and the effect of back-scattering (which gives rise to  $\mathcal{T}_j^{\xi c}$  and  $\mathcal{T}_j^{\xi s}$ , blue and purple dashed curves) even smaller.

### 2.5.3 Thermal Noise Contributions from Different Layers

Let us now examine the breakdown of the total coating noise by plotting the coefficients  $q_j^B$  and  $q_j^S$  in Eq. (2.94). In Fig. 2.7, we plot silica contributions on top panels, and tantala contributions on lower panels, with bulk contributions on left panels, and shear contributions on right panels. Here we use the baseline parameters shown in Table 2.2. As it turns out, the results for conventional and advanced LIGO coatings are hardly distinguishable from each other—therefore we only use the advanced LIGO coating. The red curve uses  $\beta = -1$ , black uses  $\beta = 0$  and blue uses  $\beta = 1$ . Superimposed onto the solid lines are dashed lines of each type, calculated without introducing the back-scattering terms; the effect is noticeable for the first few layers.

## 2.6 Dependence of Thermal Noise on Material Parameters

Experimental knowledge of coating materials is limited. Most notably, values of Young's moduli and Poisson's ratios of the coating materials are still uncertain, while only *one combination* of the two loss angles have been experimentally measured by ring-down experiments. In this section, we explore the possible variation in coating Brownian noise, away from the baseline configuration (Table 2.2), considering these uncertainties. We shall use the advanced LIGO coating structure mentioned in the previous section.

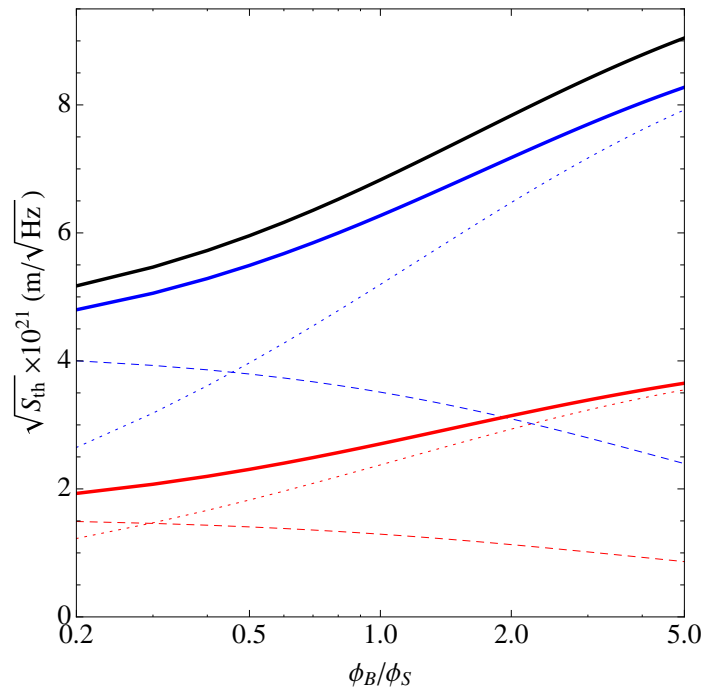


Figure 2.8: (color online) Variations in thermal noise contributions when  $\phi_B/\phi_S$  is varied. Contributions from tantalum layers is shown in blue, those from silica layers are shown in red. The total thermal noise is in black. Bulk contributions are shown in dotted curves, while shear contributions are shown in dashed curves.

### 2.6.1 Dependence on Ratios Between Loss Angles

In the baseline (Table 2.2), we have assumed that  $\phi_B$  and  $\phi_S$  are equal, but this is only out of our ignorance: experiments have only been able to determine one particular combination of these two angles. We now explore the consequence of having these loss angles not equal, while keeping fixed the combination measured by ring down rate of drum modes [see Eq. (2.69)].

In Figure 2.8, while fixing all other baseline parameters, we plot how each type of thermal noise (i.e., silica vs tantalum, bulk vs shear) varies when the ratio  $\phi_B/\phi_S$  for both tantalum and silica layers varies between 1/5 and 5. We use blue for tantalum, red for silica, dotted for bulk, dashed for shear, and solid for the total of bulk and shear. In this configuration, tantalum layers' contribution to thermal noise always dominates over silica layers, mainly due to the higher loss angle. As we vary the ratio between the loss angles, there is moderate variation of thermal noise. For the dominant tantalum, as  $\phi_B/\phi_S$  vary from 1/5 to 5, there is a 30% change in thermal noise, while for silica, the change is a more significant 68%.

As we see from Fig. 2.8, a larger value of  $\phi_B/\phi_S$  gives rise to higher bulk, lower shear, and higher total noise—this is reasonable because bulk fluctuations drive correlated noise between layer's thickness and the height of coating-substrate interface, while shear fluctuations drive anticorrelated

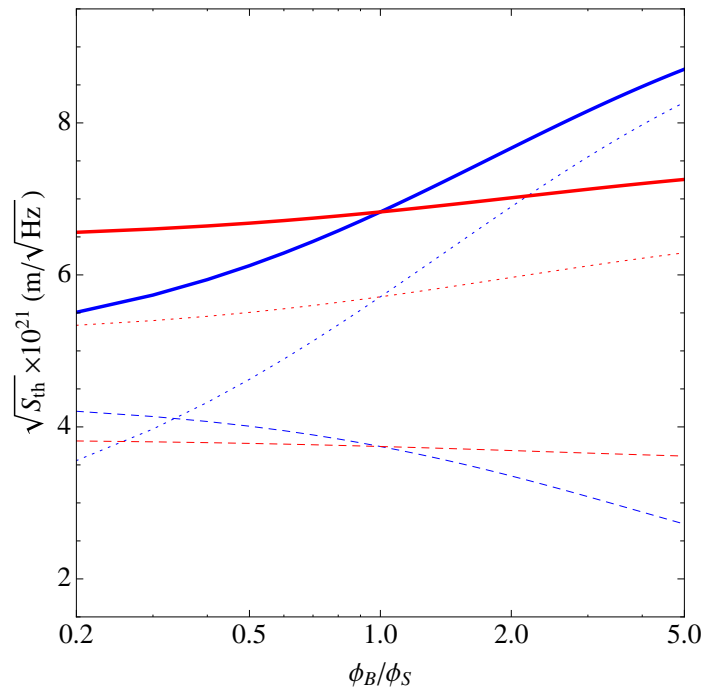


Figure 2.9: (color online) Variations in total noise when  $\phi_B/\phi_S$  is varied: (solid) total noise, (dotted) total bulk noise, (dashed) total shear noise. The red (blue) curve corresponds to only varying  $\phi_B/\phi_S$  for tantalum (silica). With  $\phi_B/\phi_S$  of tantalum or silica varying from 0.2 to 5, the change in total noise is 58.1% and 10.6%, respectively.

noise, as shown in Fig. 2.3.

Moreover, the fact that variation is more significant for silica layers can be explained when we recall that thickness-induced thermal noise is proportional to  $1/Y_c$ , while surface-height-induced thermal noise is proportional to  $Y_c/Y_s^2$ . For silica layers,  $Y_c$  is assumed to be equal to  $Y_s$ , so the two types of noise being added (bulk) or subtracted (shear) are more comparable in magnitude; by contrast, the Young's modulus of tantalum layers is significantly higher than that of the substrate, causing the noise to be dominated by fluctuations of the height of the coating-substrate interface, therefore making correlations between the two types of noise less important.

In Fig. 2.9, we plot variations in the total noise as we vary  $\phi_B/\phi_S$  for silica layers (blue) or tantalum layers (red) only, and fix the other one. It shows that the variance of tantalum's loss angle will generate larger change of the total noise.

## 2.6.2 Dependence on Young's moduli and Poisson's ratios

Since the Young's modulus and Poisson's ratios of coating materials, especially of tantalum, are also uncertain. In Fig. 2.10, we plot variations of tantalum thermal noise when its Young's modulus varies from the baseline value by up to a factor of 2, for  $\phi_B/\phi_S = 0.2, 0.5, 1, 2,$  and 5. The noise is seen

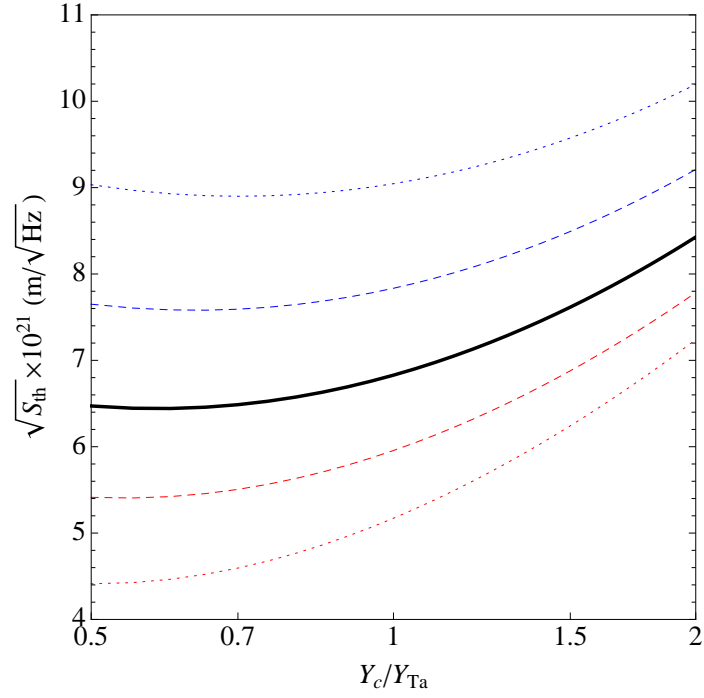


Figure 2.10: Thermal noise contribution from tantalum, as its Young's modulus deviates from baseline value, for  $\phi_B/\phi_S=5$  (blue dashed), 2 (blue dotted), 1 (black solid), 1/2 (red dotted), and 1/5 (red dashed)

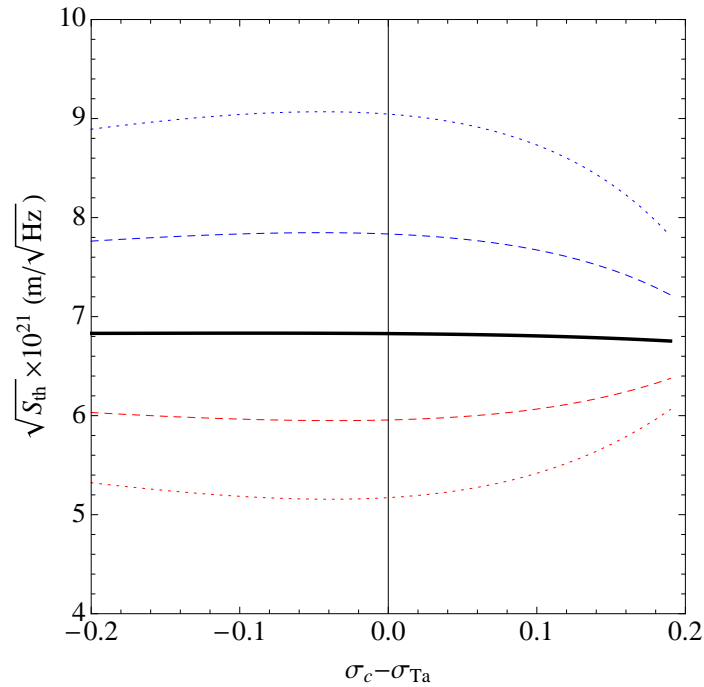


Figure 2.11: Thermal noise contribution from tantalum, as its Poisson's ratio deviates from baseline value, for  $\phi_B/\phi_S=5$  (blue dashed), 2 (blue dotted), 1 (black solid), 1/2 (red dotted), and 1/5 (red dashed)

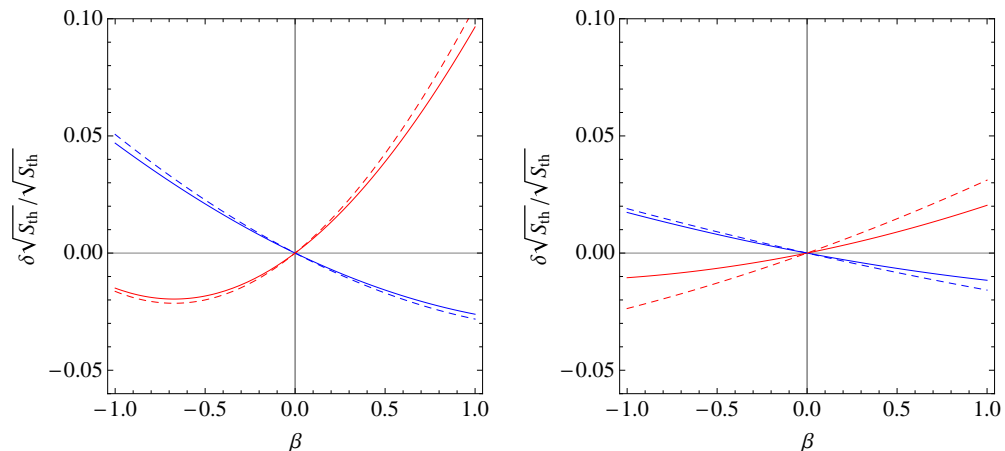


Figure 2.12: Fractional change in the contribution to thermal noise from all silica layers (left panel) and all tantala layers (right panel), due to bulk (blue) and shear (red) loss. Dashed lines indicate results calculated without including back-scattering terms.

to vary by  $\sim 15\%$  as Young's modulus varies by a factor of  $\sim 2$ .

We can also explain the way the thermal noise varies as a function of  $Y_c$ . Starting from the baseline value, a lower  $Y_c$  leads to a lower thermal noise, until  $Y_c$  becomes comparable to  $Y_s$  (which we fix at the baseline value, equal to  $0.5Y_{\text{Ta}}$ ), and starts to increase again. Such a behavior is reasonable because thickness noise spectrum and interface noise spectrum are proportional to  $\sim 1/Y_c$  and  $\sim Y_c/Y_s^2$ , respectively—as we decrease  $Y_c$  from the baseline  $Y_{\text{Ta}}$  value, we transition from interface fluctuation being dominant towards equal amount of both noises (which gives a minimum total noise), and then towards thickness fluctuation becoming dominant.

In Fig. 2.11, we explore the effect of varying coating Poisson's ratio, for the same values of  $\phi_B/\phi_S$  chosen in Fig. 2.10. In the baseline assumption of  $\phi_B = \phi_S$ , when bulk and shear have the same level of loss, thermal noise does not depend much on Poisson's ratio. However, if  $\phi_B/\phi_S$  turns out to differ significantly from 1, and if Poisson's ratio can be larger than the baseline value by more than  $\sim 0.1$ , then thermal noise can vary by  $\sim 10\%$ .

### 2.6.3 Dependence on Photoelastic Coefficients

Photoelastic properties of the coating materials are not yet well known. In Fig. 2.12, we plot the fractional change in thermal noise, separately for silica (left panel) and tantala (right pane), and for bulk (blue) and shear (red) losses, when we vary  $\beta$  between -1 and +1. Dashed curves are obtained ignoring back-scattering effects.

It is interesting to note that for small values of  $\beta$ , the dependence of noise on  $\beta$  have different trends for bulk and shear contributions. This is also related to the different types of correlations

between thickness and interface height fluctuations. As we can see from the Figure, the effect of varying  $\beta$  is small, since it only affects thermal noise due to light penetration into the first few layers. If bulk and shear losses are indeed comparable, then cancelation between these two types of noises (especially for the more lossy tantala layers) will likely make the photo elastic effect completely negligible. Even in the case when one particular type of loss dominates shall we expect at most  $\sim 2\%$  contribution from photo elasticity of the more lossy tantala—if we further assume that  $|\beta| \sim 1$  [right panel of Fig. 2.12].

## 2.6.4 Optimization of Coating Structure

Although a standard highly reflective coating consists of  $\lambda/4$  layers of alternating material capped by a  $\lambda/2$  layer, this structure can be modified to lower thermal noise while still maintaining a high reflectivity for the 1064 nm carrier light, e.g., as shown by Agresti et al. [26]. As their results have indicated, for baseline coating parameters and neglecting light penetration into the coating layers [11], the optimal structure is more close to a stack of pairs of  $\lambda/8$  ( $\text{Ta}_2\text{O}_5$ ) and  $3\lambda/8$  ( $\text{SiO}_2$ ) layers, capped by a  $\lambda/2$  ( $\text{SiO}_2$ ) layer. This alternative coating structure shortens the total thickness of the more lossy tantala layers, while maintaining a high reflectivity for the light. The *advanced LIGO type* coating given in Appendix 2.12, on the other hand, has been optimized considering reflectivity at both 1064 nm and 532 nm, as well as thermal noise—although light penetration into the layers have not been considered.

In this section, we carry out a numerical optimization taking penetration into account. We first fix the number  $N$  of layers ( $N$  is even, so we have  $N/2$  pairs), and then for  $N$ , we use the Lagrange multiplier method to search for the constrained minimum of  $S_{\text{th}}$ , fixing  $T_{1064}$  and  $T_{532}$ , namely the power transmissivity,  $1 - |\rho|^2$  assuming the coating is lossless, evaluated at 1064 nm and 532 nm, respectively. The quantity we seek to minimize (or, the *cost function*) is

$$y \equiv \sqrt{S_{\text{th}}} + \mu_1 T_{1064} + \mu_2 (T_{532} - 5\%)^2. \quad (2.105)$$

As we vary  $\mu_1$  and  $\mu_2$  and minimizing  $y$ , we obtain the constrained minimum of  $\sqrt{S_{\text{th}}}$  for different pairs of  $(T_{532}, T_{1064})$ . The aim is to obtain a series of coating configurations with approximately 5% transitivity for 532 nm, and with minimized thermal noise for a variable 3–20 ppm transmissivity for 1064 nm. (Note that the choice of the cost function contains a certain level of arbitrariness.)

Since we are going to carry out minimization for a large number of multipliers over a large number of degrees of freedom, we have chosen to proceed gradually allowing only the first  $n$  pairs and last  $n$  pairs of layers to vary, while maintaining the same pair structure for  $N/2 - n$  pairs in the middle

(repeating doublets). In other words, our coating structure looks like:

$$\underbrace{\hspace{2cm}}_{2n \text{ layers}}^{\text{free}} \quad \underbrace{\hspace{2cm}}_{N - 2n \text{ layers}}^{\text{repeating pair}} \quad \underbrace{\hspace{2cm}}_{2n \text{ layers}}^{\text{free}} .$$

In this work, we found that it suffices to choose  $n = 2$  (which corresponds to optimizing over 10 parameters); further increasing  $n$  does not lead to noticeable improvements. During our numerical optimization, we have adopted the *downhill simplex method* [27, 28].

target $\phi_B/\phi_S$	$N$	Resulting Coating Structure										$\sqrt{S_{\text{th}}^{\text{opt}}}$			$\sqrt{S_{\text{th}}^{\lambda/4}}$
		First 4 layers				Repeated Pair		Last 4 layers				$\frac{\phi_B}{\phi_S} = \frac{1}{5}$	$\frac{\phi_B}{\phi_S} = 1$	$\frac{\phi_B}{\phi_S} = 5$	
1/5	42	0.0479	0.1581	0.3430	0.1760	0.2919	0.1897	0.3164	0.1738	0.3178	0.1627	<b>5.01</b>	6.64	8.81	5.35
1	42	0.1020	0.1250	0.3267	0.1917	0.2911	0.1914	0.3110	0.1752	0.3196	0.1609	5.02	<b>6.64</b>	8.81	7.05
5	42	0.1118	0.0968	0.3353	0.1882	0.2893	0.1939	0.3135	0.1673	0.3199	0.1662	5.02	6.64	<b>8.81</b>	9.33

Table 2.3: Results of coating-structure optimization. We list optimized coating structures for  $T_{1064} = 5$  ppm and  $T_{532} = 5\%$ , for three target values of  $\phi_B/\phi_S$  while fixing the measured effective loss angle  $\phi_D$  [Eq. (2.56)] and other baseline material parameters [Table 2.2]. Thickness of coating layers are given in units of wavelength (for 1064 nm light). For each optimized coating structure, thermal noise is calculated separately for all three values of  $\phi_B/\phi_S$ , and given in units of  $10^{-21}$  m/ $\sqrt{\text{Hz}}$  (thermal noise for the target  $\phi_B/\phi_S$  is given in boldface, and boldface numbers should be the minimum within its column); thermal noise spectra of the 38-layer  $\lambda/4$  stack assuming the target  $\phi_B/\phi_S$  are also listed for comparison.

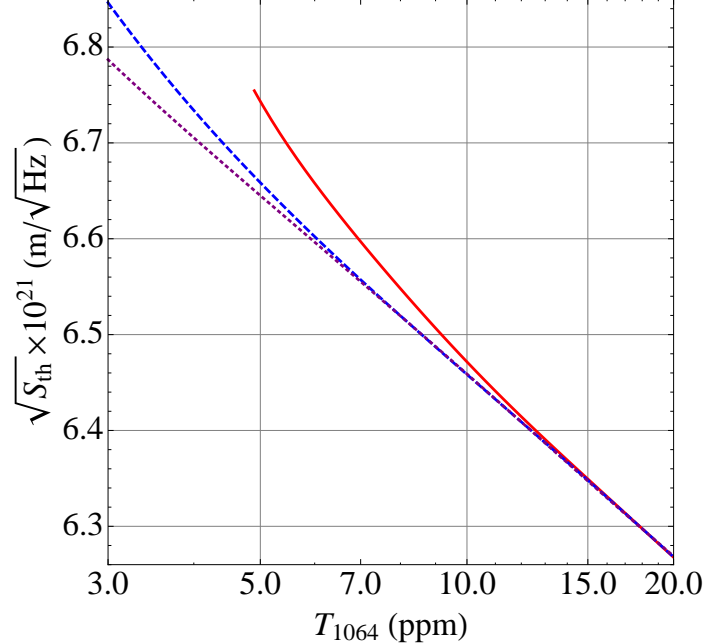


Figure 2.13: Optimized thermal noise versus transmissivity at 1064 nm, for a coating of 38 (red), 40 (blue), and 42 (purple) layers

Results for baseline material parameters (Table. 2.2) and  $N = 38, 40$  and  $42$  have been shown in Figure 2.13. This figure indicates that different numbers of layers should be chosen for different

target  $T_{1064}$ —more layers are required for lower transmissivity (higher reflectivity). Overall, the optimal thermal noise varies by around  $\sim 10\%$  as for  $T_{1064}$  from 3 to 20 ppm. In particular, for the standard Advanced LIGO requirement of 5 ppm (see first column of Table 2.3), 42 layers are found to be optimal. This is 2 more pairs or 4 more layers than the 38-layer  $\lambda/4$  doublet, which has the minimum number of layers to reach 5 ppm. The larger number of layers here gets lower thermal noise (by 6%) because the more-lossy tantala layers are shortened, and the less-lossy silica layers lengthened.

We have further optimized the structure when the ratio  $\phi_B/\phi_S$  is different from 1, while keeping fixed the effective loss angle measured so far—as done in Sec. 2.6.1. For  $T_{1064} = 5$  ppm, we have listed results of optimized coating structure and thermal noise in the second and third columns of Table 2.3. The extent of variation found here is comparable to those obtained in Sec. 2.6.1 using a standard coating structure without optimization: the optimal coating structures consistently lower thermal noise by about 6%. In addition, as shown in Table 2.3, the optimal coating structure is robust against changes in  $\phi_B/\phi_S$ : structure obtained for any one of the values of the ratio is already almost optimal for all other ratios.

## 2.7 Measurements of Loss Angles

In this section, we study possible mechanical ringdown experiments that can be used to measure independently the bulk and shear loss angles,  $\phi_B$  and  $\phi_S$  of a coating material.

In a ringdown experiment, a sample with a high intrinsic  $Q$  is coated with a thin layer of the coating material in question. Due to the mechanical losses in the coating, the quality factor of the mechanical eigenmodes of the sample will be reduced [29, 30]. More specifically, for the  $n^{\text{th}}$  eigenmode with resonant frequency  $f_n$ , if an e-folding decay time of  $\tau_n$  is measured, then the quality factor is

$$Q_n = \pi f_n \tau_n, \quad (2.106)$$

while correspondingly, the loss angle is given by

$$\phi(f_n) = 1/Q_n, \quad (2.107)$$

which is equal to the amount of energy dissipated  $W_{\text{diss}}$  per radian.

### 2.7.1 Bending Modes of a Thin Rectangular Plate

Figure 2.14 shows the schematic geometry of a rectangularly shaped sample, in which a thin coating layer with thickness  $d$  is deposited on a rectangular plate with dimensions  $a \times b \times c$  ( $c \ll a, b$ ), and  $d$  is much less than  $c$ . If we pay attention only to the transverse oscillations of the plate, the amount

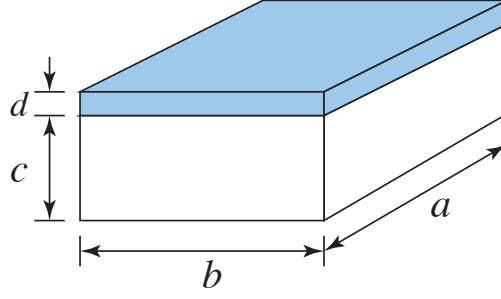


Figure 2.14: Rectangular shaped thin plate ( $a \times b \times c$ ) with thin coating (thickness  $d$ ):  $c \ll a, b; d \ll c$ . The transverse vibration mode is considered in this case.

of energy stored in the coating layer, in the form of bulk and shear energies  $U_B$  and  $U_S$ , as a fraction of the entire energy  $U$ , can be calculated as

$$\frac{U_B}{U} = \frac{d Y_c (1 - \sigma_s^2)(1 - 2\sigma_c)}{c Y_s (1 - \sigma_c)^2} \quad (2.108)$$

$$\frac{U_S}{U} = \frac{2d Y_c (1 - \sigma_s^2)(1 - \sigma_c + \sigma_c^2)}{c Y_s (1 - \sigma_c)^2(1 + \sigma_c)}. \quad (2.109)$$

Using Eq. (2.58), the the total loss angle of the sample is

$$\phi = \phi_{\text{sub}} + \frac{d Y_c (1 - \sigma_s^2)}{c Y_s (1 - \sigma_c)^2} \left[ \phi_B(1 - 2\sigma_c) + 2\phi_S \frac{1 - \sigma_c + \sigma_c^2}{1 + \sigma_c} \right]. \quad (2.110)$$

It is not surprising that this combination of  $\phi_B$  and  $\phi_S$  is proportional to  $\phi_D$  [cf. Eq. (2.56)], the loss angle of the 2-D flexural rigidity of the coating material, which we defined in Sec. 2.3.2. This is because when the drum mode of a thinly coated plate is excited, the stress  $T_{zz}$  remains zero within the coating layer, and the layer's elastic response is governed by the flexural rigidity, as defined in Sec. 13 of Ref. [14].

As it turns out, the part of coating thermal noise due to bending of the coating-substrate interface [ $S_{z_s z_s}$  in Eq. (2.87b)] also depends directly on  $\phi_D$ , because the loss mechanism in this case is the same as during the oscillation of a drum mode—one only applies a perpendicular force from below the coating layer, while keeping  $T_{zz} = 0$  within the layer.

It proves less straightforward to connect the thickness fluctuation part of thermal noise [ $S_{u_z u_z}$  in Eq. (2.87a)] to the effective loss angle of either  $Y$  or  $D$ . Although the loss mechanism here is due to the compressing of a thin membrane from both sides—this membrane is not characterized by vanishing  $T_{xx}$  and  $T_{yy}$ , because the coating is attached to a substrate which provides restoring forces along the transverse ( $x$  and  $y$ ) directions. However, in the case when the Poisson ratio  $\sigma_c$  of the coating vanishes, the thickness fluctuation does depend on the loss angle of the Young's modulus.

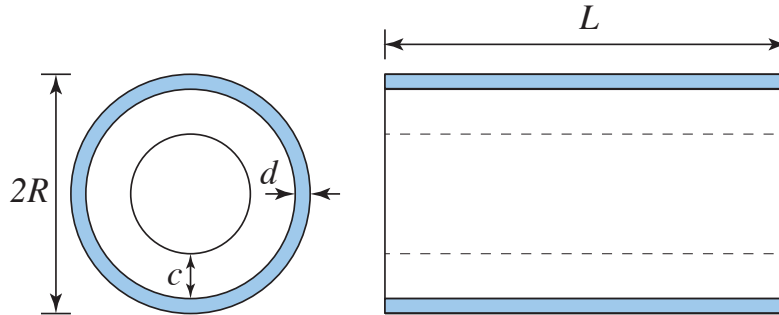


Figure 2.15: Thin cylindrical shell with thin coating outside. The first torsional eigenmodes of such a shell can be used to measure the shear loss angle of the coating.

For our baseline parameters, mechanical dissipation is mostly contributed by the tantala layers, and because the Young's modulus of the tantala coating material is assumed to be much greater than that of the substrate, the largest contribution to the LIGO mirrors' Brownian noise is bending noise  $S_{z_s z_s}$ . This explains why the noise only varies by 30% (as noted in Sec. 2.6.1) even if no further measurements on the other loss angle are made.

### 2.7.2 Torsional Modes of a Coated Hollow Cylinder

Here we propose an approach with which we can measure another combination of loss angles. We consider a cylindrical shell with a thin, uniform coating layer outside, as shown in Fig. 2.15 ( $c \ll R$ ,  $d \ll c$ ). In this configuration, the surface deformations produce strains in the plane of shell according to the Donnell shell theory [31]. Here we assumed that there is only angular displacement in the shell, which means the longitudinal position of the cross section won't change. For a torsion mode, we only have shear strain energy, the expressions are given by

$$\frac{U_B}{U} = 0 \quad (2.111)$$

$$\frac{U_S}{U} = \frac{d Y_c (1 + \sigma_s)}{c Y_s (1 + \sigma_c)}. \quad (2.112)$$

As a consequence, the total loss angle can be expressed as

$$\phi = \phi_{\text{sub}} + \frac{d Y_c (1 + \sigma_s)}{c Y_s (1 + \sigma_c)} \phi_S. \quad (2.113)$$

For a cylinder shell, according to the Donnell shell theory, the natural frequency of the  $n$ -th torsional mode is given by [32]

$$f_n = \frac{n}{2^{\frac{3}{2}} L} \left[ \frac{Y}{\rho(1 + \sigma)} \right]^{1/2}. \quad (2.114)$$

A more accurate calculation may be found by using the Flügge shell theory [33].

Using the values from Table 2.4, we can estimate the resonant frequency to be 9.2 kHz. The coating contribution to loss angle, assuming a  $\phi_S$  of at least  $10^{-5}$ , would be at least the order of  $10^{-6}$ , which seems plausible to be extracted from ring-down measurements.

Table 2.4: Example parameters of a thin, uniformly coated cylindrical shell ( $\text{SiO}_2$ )

	$L$	$R$	$c$	$d$
unit(mm)	200	50	1	0.04

With the measurement of both the thin plate and cylinder shell, we can obtain  $\phi_B$  and  $\phi_S$  of the coating.

## 2.8 Conclusions

In this paper, by applying the fluctuation-dissipation theorem, we obtained a *full set of correlation functions* (2.87a)–(2.87c) of Brownian thermal fluctuations of a multilayer dielectric coating. In particular, we have related fluctuations of coating thickness and coating-substrate interface to *independent* bulk and shear thermal stresses associated with each coating layer. These stresses not only induce thickness fluctuations of the layers themselves, but also bends the coating-substrate interface—this bending noise had not been previously appreciated intuitively, although its effect has been incorporated into formulas, e.g., in Ref. [11]. As a result, we found that although thickness fluctuations of different coating layers are independent of each other, they each have partial correlations with the height fluctuations of the coating-substrate interface. Moreover, bulk loss creates a positive correlation between them, while shear loss creates a negative correlation. The entire picture is succinctly written mathematically in Eqs. (2.89) and (2.90). This coherence structure then gives coating Brownian noise in Eq. (2.93). Apart from having provided a pedagogical and systematic derivation of these noise components, the most important conceptual consequence of our work is to point out an uncertainty in coating loss angles, which has not been anticipated previously. We have also incorporated the photo elastic effect, the reflectivity fluctuations of the interfaces within the multilayer coating, and considered the effect of amplitude modulations caused by Brownian thermal noise. All of these turned out to be rather unimportant.

We have applied our formalism to mirrors that are to be used in Advanced LIGO detectors. As estimated in Sec. 2.6 and summarized in Table 2.5 (calculated for a typical candidate for the Advanced LIGO end test-mass mirror coating configuration), parameter uncertainties could lead to non-negligible corrections to coating Brownian noise calculations. The biggest uncertainties actually arise from the elastic moduli of coating materials—for example, current uncertainties in Young’s modulus of the tantala coating material might lead up to 60% increase in thermal noise. Although photo elastic coefficients for our coating materials are very uncertain, they do not significantly affect

material parameter	range	uncertainty in $\sqrt{S_x}$	for details, see
$\phi_B/\phi_S$	$0.2 - 5^1$	$\pm 37\%$	Sec. 2.6.1, Figs. 2.8, 2.9.
$Y_{\text{Ta}}$	factor of $\sim 2$	$\sim 60\%$	Sec. 2.6.2, Fig. 2.10.
$\sigma_{\text{Ta}}$	$\pm 0.2$	up to 10% if $\phi_B/\phi_S \neq 1$	Sec. 2.6.2, Fig. 2.11.
$\beta$	$-1 < \beta < +1$	$\pm 1\%$ <sup>2</sup>	Sec. 2.6.3, Fig. 2.12.

Table 2.5: Levels of thermal noise uncertainty caused by parameter uncertainties

thermal noise since light does not penetrate through many layers.

It is rather remarkable that our lack of experimental knowledge about the loss angles, beyond what we had already obtained from the ring down of drum modes, would not give rise to a higher uncertainty in thermal noise. This is rather serendipitous, considering our path of understanding of the problem: for the baseline parameters of advanced LIGO, the highest contribution to coating Brownian noise arises from the coating-substrate bending noise caused by losses in tantala layers, because these layers are much more lossy than the silica layers, and have been assumed to have a much higher Young’s modulus than the substrate material. This bending noise, first elaborated by this work, turns out to be associated with the loss angle of the 2-D flexural rigidity, which in turn is directly connected to the decay of the drum modes of a thinly coated sample. This means the currently existing program has been measuring the predominant loss angle all along. Nevertheless, the level of uncertainty noted in our study still warrants further experiments seeking the other loss angle, e.g., as outlined in Sec. 2.7. In addition, since future gravitational-wave detectors may use different substrate and coating materials, situations may arise when the loss angle measured now does not correlate with the total coating brownian noise.

At this moment, it is worth looking once more at the previously used loss angles,  $\phi_{\parallel}$  and  $\phi_{\perp}$ —although they are mathematically ill defined, they do correctly reflect the existence of two channels of loss. The  $\phi_{\parallel}$  was meant to characterize losses incurred by the  $x$ - $y$  deformations of the coating measurable when we do not compress the coating but instead drive its deformations using drum modes of the substrate. This loss angle is now replaced by the (mathematically well-defined) imaginary part of the flexural rigidity, for which extensive measurements have already been carried out. The  $\phi_{\perp}$  was meant to characterize the losses incurred by compressing the coating layers. This has not been measured because it had not been obvious how to easily excite this mode of coating deformation (the most obvious way would be to compress the coating layer, but that is difficult); however, because the Young’s modulus of the coating is much larger than that of the substrate, this difficult-to-measure loss angle should not contribute as much to the total coating noise. This said, in this work, we do come up with ways to measure both loss angles,  $\phi_S$  and  $\phi_B$ , without having to compress the coating layers—but instead by exciting different modes of substrate deformation. Of course, this is only possible because we have assumed that the material is isotropic—otherwise we

may have to compress the coating to directly access the loss induced by such a deformation.

On the other hand, one may think of the possibilities of using substrate materials with higher Young’s modulus to reduce the bending noise. Sapphire and Silicon are two viable choices because they both have higher Young’s modulus than tantalum. Using Eq. (2.87a)–(2.87c), it is straight forward to estimate the new coating Brownian noise while replacing the substrate material by sapphire or silicon but keeping the same aLIGO coating design. It turns out that the coating brownian noise will be reduced to 35% of its original power spectra value if we use silicon substrate or 32% if we use sapphire. However, there are other disadvantages for sapphire or silicon substrate that prevents us from using them for aLIGO mirrors. The main problem is that they both have very high thermal conductivity—much higher than fused silica. As a result, the substrate thermoelastic noise is one of the important noise source for both materials. For instance, if the aLIGO mirror was made of sapphire, the bulk thermal elastic noise would have about the same magnitude as the coating brownian noise at 100 Hz. As for silicon substrate, the bulk thermal elastic noise is more than 4 times larger than its corresponding coating brownian noise in power because silicon has even higher thermal conductivity than sapphire. One may refer to [37] for detailed methods to calculate bulk thermal elastic noise. Setting up the experiment in a cryogenic environment is a possible way to reduce the thermooptic noise.

Furthermore, our formula Eq. (2.93) can serve as a starting point for optimizing the material choice and structure design of the multilayer coating taking light penetration effects into account. Our numerical results in Sec. 2.6.4 (see Table 2.3) have shown that optimization of the coating structure consistently offers a  $\sim 6\%$  decrease in thermal noise, regardless of  $\phi_B/\phi_S$ . In fact, the optimal structure for these ratios are quite similar, and configurations obtained for each presumed ratio of  $\phi_B/\phi_S$  are shown to work for other ratios interchangeably.

Upon completion of this manuscript, we noted that the optimization of coating structure for the case assuming  $\phi_B = \phi_S$  (and  $\beta = 0$ ) has been carried out by Kondratiev, Gurkovsky and Gorodetsky [34]. [We note that their formalism is capable to treating  $\beta \neq 0$  and  $\phi_B \neq \phi_S$ , as well as back-scattering induced by photo elasticity, but they did not explore the impact of these effects in their optimization.] Our results are compatible with theirs, if we also use these restrictions in parameter space and ignore back-scattering.

A comparison between our result, Kondratiev et al., and Harry et al. [11] (which ignores light penetration into the layers, and also effectively assumes  $\phi_S = \phi_B$ ) would therefore illustrate the effects caused by ignoring photoelasticity and further ignoring light penetration into the coating. This is shown in Table 2.6. This again confirms that for total coating thermal noise, light penetration causes noticeable difference in coating thermal noise, while photoelasticity causes a negligible difference.

Coating	Ref. [11] (no light penetration)	Ref. [34] ( $\beta = 0$ and no back scattering)	This Work
$\lambda/4$	7.18	7.08	7.08
Advanced LIGO	6.93	6.82	6.83
optimal	6.73	6.62	6.64

Table 2.6: Comparison of thermal noise spectral density (assuming  $\phi_B = \phi_S$  and evaluated at 200 Hz, in units of  $10^{-21}\text{m}/\sqrt{\text{Hz}}$ ) between different works

## 2.9 Appendix A: Fluctuations of the Complex Reflectivity due to Refractive index fluctuations

Brownian noise is not only caused by the random strains, but also by the refractive-index fluctuations caused by such strains, through the photo elastic effect [cf. Eqs. (2.13) and (2.14)]. We shall quantify this contribution in this section.

### 2.9.1 The Photoelastic Effect

If we denote the displacement of coating mass elements as  $(u_x, u_y, u_z)$ , then the relative coating-thickness change from its equilibrium value can be written as

$$\delta l/l = u_{z,z} \quad (2.115)$$

and the relative transverse area expansion can be written as

$$\delta A/A = u_{x,x} + u_{y,y}. \quad (2.116)$$

If we denote 2-dimensional displacement vectors along the  $x$ - $y$  plane as  $\vec{u} = (u_x, u_y)$ , and two-dimensional gradient as  $\vec{\nabla}$ , then we have

$$\delta A/A = u_{x,x} + u_{y,y} = \vec{\nabla} \cdot \vec{u}. \quad (2.117)$$

We can then write the change in refractive index as

$$\delta n = \left[ \frac{\partial n}{\partial \log l} \right]_{A_j} \frac{\delta l}{l} + \left[ \frac{\partial n}{\partial \log A} \right]_{l_j} \vec{\nabla} \cdot \vec{u} \quad (2.118)$$

where  $\partial n/\partial \log l$  and  $\partial n/\partial \log A$  only depends on material properties. The two terms on the right-hand side of Eq. (2.118) represent refractive index change driven by relative length and area changes,

respectively. The *first term* is given by [24]

$$\beta^L = \left[ \frac{\partial n}{\partial \log l} \right]_A = -\frac{1}{2}n^3CY \quad (2.119)$$

where  $C$  is the photoelastic stress constant,  $Y$  is the Young's modulus. For silica,  $CY \approx 0.27$ , therefore  $\beta_{\text{Si}}^L = -0.41$ . The photoelastic coefficient can also be written as

$$\beta = -\frac{1}{2}n^3p_{ij} \quad (2.120)$$

where  $p_{ij}$  is the photo elastic tensor [36]. Some experiments have been done to measure this coefficient for tantala [23]. Empirically, the value of  $p_{ij}$  varies from  $-0.15$  to  $0.45$  for  $\text{Ta}_2\text{O}_5$  thin film fabricated in different ways. Here for the longitudinal photoelasticity,  $\beta_{\text{Tan}}^L$ , we use  $-0.5$  in our numerical calculation.

We shall next obtain formulas that will allow us to convert fluctuations in  $n$  into fluctuations in the complex reflectivity of the multilayer coating.

### 2.9.2 Fluctuations in an Infinitesimally Thin Layer

Because the coating is much thinner than the beam spot size, we only consider phase shifts along the  $z$  direction—for each value of  $\vec{x}$ . If the refractive index  $\delta n$  at a particular location  $\delta n(z)$  is driven by longitudinal strain  $u_{zz}$  at that location, the fact that  $\langle u_{zz}(z')u_{zz}(z'') \rangle \propto \delta(z' - z'')$  causes concern, because this indicates a high *variance* of  $\delta n$  at any given single point  $z$ , with a magnitude which is formally infinity, and in reality must be described by additional physics (for example, there would be a scale at which the above-mentioned delta function starts to become resolved). Therefore, if we naively considers the reflection of light across an interface, at  $z = z_0$ , then the independent and high-magnitude fluctuations of  $n(z_0-)$  and  $n(z_0+)$  would lead to a dramatic fluctuation in the reflectivity

$$r = \frac{n(z_0-) - n(z_0+)}{n(z_0+) + n(z_0-)} \quad (2.121)$$

of the interface, whose magnitude of fluctuation seems to be indefinitely large. Fortunately, for any thin layer, if we simultaneously consider propagation through this layer and the reflection and transmission across *both* of its boundaries, then the effect caused by the refractive index fluctuation of this particular layer can be dramatically suppressed. Nevertheless, we do find an additional fluctuating contribution to the total complex reflectivity of the multilayer coating.

In order to carry out a correct calculation that does not diverge, we first consider a three-layer and two-interface situation, as shown in Fig. 2.16, with  $n_1$ ,  $n_2$ , and  $n_3$  separated by two interfaces, with the length of the  $n_2$  layer given by  $\Delta l$ —and here we only consider fluctuations in  $n_2$ . The

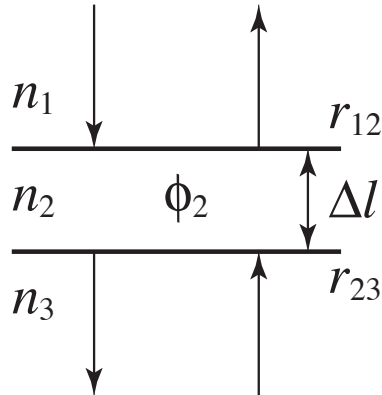


Figure 2.16: Light propagation across a thin layer (thickness of  $\Delta l$ ) with fluctuating refractive index (from a uniform  $n_2$  to an average of  $n_2 + \delta n_2$  within this thin layer). The propagation matrix corresponding to this structure is given by Eq. (2.122).

entire transfer matrix (from below to above, in Fig. 2.16) is given by

$$\mathbf{M} = \mathbf{R}_{r_{12}} \mathbf{T}_{\phi_2} \mathbf{R}_{r_{23}} . \quad (2.122)$$

following the same convention as in Sec. 2.2.3. Suppose the originally uniform  $n_2$  now fluctuates, and after averaging over this thin layer, gives a mean refractive index of  $n_2 + \delta n_2$ , we use this as the refractive index of the entire layer, and then have

$$\delta \mathbf{M} = \frac{n_2}{\sqrt{n_1 n_3}} \begin{pmatrix} i & -i \\ i & -i \end{pmatrix} \delta n_2 \cdot k_0 \Delta l \quad (2.123)$$

This can be considered as a regularization, because each individual  $\mathbf{R}_{r_{12}}$  or  $\mathbf{T}_{\phi_2}$  (since their expressions only contain  $n_1$ ,  $n_2$ , and  $n_3$  but no  $l$ ) has a standard deviation proportional to  $O(1/\sqrt{\Delta l})$  (when  $\Delta l$  is greater than the coherence length of refractive-index fluctuation) or  $O(1/\Delta l)$  (when  $\Delta l$  is less than the coherence length of refractive-index fluctuation)—both diverge as  $\Delta l \rightarrow 0$ —which means the reflectivity fluctuation of each of these layers diverge. However, in order for our use of average refractive index to make sense in calculating the reflectivities  $r_{12}$  and  $r_{23}$ ,  $\Delta l$  should be less than the coherence length of refractive index fluctuations. In any case, the total transfer matrix  $\delta M$  does not diverge; it instead has an infinitesimal fluctuation. Moreover, since  $\delta M$  only depends on  $\delta n_2 \cdot \Delta l$ , we shall see that the particular choice of  $\Delta l$  will not affect the final results when layers like these are stacked together.

The physical meaning of Eq. (2.123) is clear: a random field of refractive index not only gives a random phase shift (diagonal term), but also gives rise to a random reflectivity (nondiagonal term). The latter term is an additional contribution that has been ignored by previous calculations.

### 2.9.3 The Entire Coating Stack

Now we are ready to consider the entire multilayer coating. Here we bear in mind that eventually, the fluctuation in  $n$  has a non-zero coherence length—and we can then divide our existing layers further into sub layers with length  $\delta l$  much less than the physical coherence length. Since each of these sub layers only makes a negligible contribution to the entire complex reflectivity, we only need to consider layers that contain only one coating material. Let us first focus on Layer  $j$ , bounded by two interfaces with reflectivities  $r_{j-1}$  and  $r_j$ , respectively. The total transfer matrix of the entire stack is written as

$$\mathbf{M} = \cdots \mathbf{T}_{\phi_{j+1}} \mathbf{R}_{r_j} \mathbf{T}_{\phi_j} \mathbf{R}_{r_{j-1}} \cdots \quad (2.124)$$

Here reflectivity fluctuations within Layer  $j$  are going to add to the matrix  $\mathbf{T}_{\phi_j}$  above. Consider  $dz$ -thick sublayer located at distance  $z'$  from the  $r_j$  boundary (lower boundary in Fig. 2.1), therefore at coordinate location  $z = z_{j+1} + z'$  and integrate, we have

$$\begin{aligned} \mathbf{T}_{\phi_j} &\rightarrow \mathbf{T}_{\phi_j} + k_0 \int_0^{l_j} \delta n(z_{j+1} + z) \mathbf{T}_{k_0 n_j z} \begin{bmatrix} i & -i \\ i & -i \end{bmatrix} \mathbf{T}_{k_0 n_j (l_j - z)} dz' \\ &= \begin{bmatrix} 1 & \delta \eta_j \\ \delta \eta_j^* & 1 \end{bmatrix} \mathbf{T}_{\phi_j + k_0 \delta \bar{n}_j l_j} \end{aligned} \quad (2.125)$$

where

$$\delta \bar{n}_j = \frac{1}{l_j} \int_0^{l_j} \delta n_j(z_{j+1} + z) dz \quad (2.126)$$

and

$$\delta \eta_j = -ik_0 \int \delta n_j(z_{j+1} + z) e^{2ik_0 n_j z} dz. \quad (2.127)$$

Here we have defined

$$z_j \equiv \sum_{n=j}^N l_n \quad (2.128)$$

to be the  $z$  coordinate of the top surface of Layer  $j$ .

We need to adapt the new transfer matrix into the old form, but with modified  $\{r_j\}$  and  $\{\phi_j\}$ . From Eq. (2.125), since  $\delta \eta_j$  is complex, we need to adjust  $\phi_j$ ,  $r_j$ , as well as  $\phi_{j+1}$ :

$$\begin{aligned} &\mathbf{T}_{\phi_{j+1}} \mathbf{R}_{r_j} \mathbf{T}_{\phi_j} \\ \rightarrow &\mathbf{T}_{\phi_{j+1} + \delta \psi_j^+} \mathbf{R}_{r_j + \delta r_j} \mathbf{T}_{\phi_j + k_0 l_j \delta \bar{n}_j + \delta \psi_j^-}. \end{aligned} \quad (2.129)$$

Here we have defined, in addition,

$$\delta r_j = -t_j^2 k_0 \int_0^{l_j} \delta n_j(z_{j+1} + z) \sin(2k_0 n_j z) dz \quad (2.130)$$

and

$$\delta \psi_j^\pm = \frac{r_j^2 \pm 1}{2r_j} k_0 \int_0^{l_j} \delta n_j(z_{j+1} + z) \cos(2k_0 n_j z) dz. \quad (2.131)$$

As we consider photoelastic noise of all the layers together,  $\delta r_j$  in Eq. (2.130) needs to be used for the effective fluctuation in reflectivity of each layer, while

$$\delta \phi_j = k_0 l_j \delta \bar{n}_j + \delta \psi_j^- + \delta \psi_{j-1}^+ \quad (2.132)$$

should be used as the total fluctuation in the phase shift of each layer.

#### 2.9.4 Unimportance of Transverse Fluctuations

Connecting with photoelastic effect, we have explicitly

$$\delta n_j(z, \vec{x}) = \beta_j^L u_{zz}(z, \vec{x}) + \beta_j^T \vec{\nabla} \cdot \vec{u}. \quad (2.133)$$

Here the vector  $\vec{u}$  is the two-dimensional displacement vector ( $u_x, u_y$ ) and  $\vec{\nabla} \cdot$  is the 2-D divergence along the  $x$ - $y$  plane. For terms that contain  $\vec{u}$ , we note that when taking the optical mode into account [see Sec. 2.2.4], i.e., when a weighted average of  $\xi$  is taken, they yield the following type of contribution

$$\begin{aligned} & \int_M I(\vec{x}) (\vec{\nabla} \cdot \vec{u}) d^2 \vec{x} \\ &= \int_{\partial M} dl (\vec{n} \cdot \vec{u} I) + \int_M \vec{u} \cdot \vec{\nabla} I d^2 \vec{x} \\ &= \int_M \vec{u} \cdot \vec{\nabla} I d^2 \vec{x}. \end{aligned} \quad (2.134)$$

Here  $M$  stands for the 2-d region occupied by the beam, and  $\partial M$  is the boundary on which power already vanishes. As a consequence, the first term is zero according to the boundary condition, while the second term gains a factor of  $(l_i/r_{\text{beam}})$  with respect to other types of coating Brownian noise, here  $l_j$  is the thickness of the  $j$ -th layer, and  $r_{\text{beam}}$  is an effective beam radius. Since we always assume coating thickness  $l_i$  to be much smaller than the beam radius  $r_{\text{beam}}$ , we can neglect refractive index fluctuation due to area fluctuation.

## 2.10 Appendix B: Elastic Deformations in The Coating

Throughout this paper, we assume the mirror substrate to be a half infinite space. We establish a Cartesian coordinate system, with  $(x, y)$  directions along the coating-substrate interface, and  $z$  direction orthogonal to the mirror surface (in the elasticity problem, we also ignore mirror curvature). This allows us to calculate elastic deformations in the spatial frequency domain. We will also assume the coating thickness to be much less than the beam spot size.

We denote the displacement along  $x$ ,  $y$  and  $z$  directions as  $u_x$ ,  $u_y$ , and  $u_z$ . It is then straightforward to express the  $3 \times 3$  strain tensor  $\mathbf{S}$  in terms of their derivatives, and stress tensor  $\mathbf{T}$  in terms of Hooke's Law:

$$S_{ij} = \frac{1}{2} \left( \frac{\partial u_i}{\partial x_j} + \frac{\partial u_j}{\partial x_i} \right) \quad (2.135)$$

$$\Theta = S_{ii} \quad (2.136)$$

$$\Sigma_{ij} = \frac{1}{2} [S_{ij} + S_{ji}] - \frac{1}{3} \delta_{ij} \Theta \quad (2.137)$$

$$T_{ij} = -K\Theta I_{ij} - 2\mu\Sigma_{ij}. \quad (2.138)$$

Here we have  $x^j = (x, y, z)$ , with Latin indices (like  $i$  and  $j$ ) running from 1 to 3. Within any layer, it is straightforward to write down the most general solution of the elasticity equilibrium equation

$$T_{ij,j} = 0 \quad (2.139)$$

as

$$\begin{aligned} \tilde{u}_x &= ik_x[(\tilde{\alpha}_+ + \kappa z \tilde{\beta}_+)e^{\kappa z} + (\tilde{\alpha}_- - \kappa z \tilde{\beta}_-)e^{-\kappa z}] \\ &\quad - ik_y[\tilde{\gamma}_+ e^{\kappa z} + \tilde{\gamma}_- e^{-\kappa z}] \end{aligned} \quad (2.140)$$

$$\begin{aligned} \tilde{u}_y &= ik_y[(\tilde{\alpha}_+ + \kappa z \tilde{\beta}_+)e^{\kappa z} + (\tilde{\alpha}_- - \kappa z \tilde{\beta}_-)e^{-\kappa z}] \\ &\quad + ik_x[\tilde{\gamma}_+ e^{\kappa z} + \tilde{\gamma}_- e^{-\kappa z}] \end{aligned} \quad (2.141)$$

$$\begin{aligned} \tilde{u}_z &= -\kappa[\tilde{\alpha}_+ + \tilde{\beta}_+(-3 + 4\sigma + \kappa z)]e^{\kappa z} \\ &\quad + \kappa[\tilde{\alpha}_- + \tilde{\beta}_-(-3 + 4\sigma - \kappa z)]e^{-\kappa z} \end{aligned} \quad (2.142)$$

where tilde denotes quantities in the  $x$ - $y$  spatial-frequency domain, and  $\kappa = \sqrt{k_x^2 + k_y^2}$ . Namely

$$u_x(x, y, z) = \int \frac{dk_x dk_y}{(2\pi)^2} \tilde{u}(k_x, k_y, z) e^{-i(k_x x + k_y y)}. \quad (2.143)$$

We now consider a single-layer coating on a substrate, with the coating-substrate interface located at  $z = 0$ , and the coating-air interface at  $z = l$ . Suppose there is a force profile  $F(x, y)$  exerted

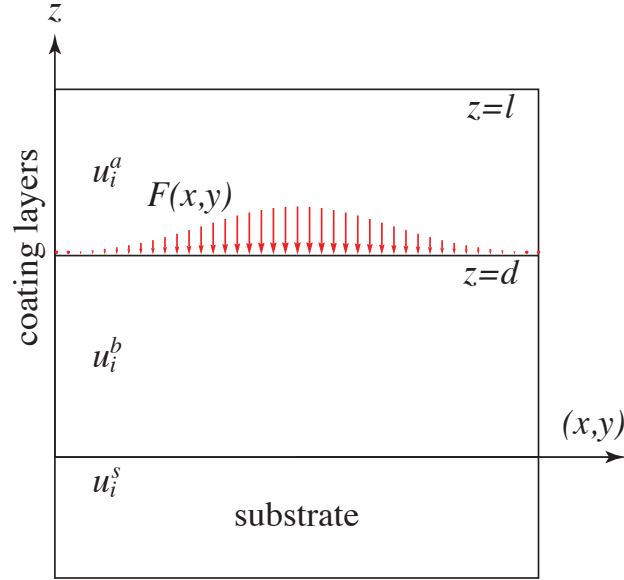


Figure 2.17: Sample with single layer coating. Force is applied perpendicular to the air/coating interface.

perpendicular to the coating surface, at  $z = d$ ,  $0 < d < l$ , and let us calculate the elastic deformation field caused by  $F$ . The entire system is now divided into three regions, (a):  $d < z < l$ , (b):  $0 < z < d$ , and (s):  $z < 0$ . At the interfaces, we obtain the following 15 boundary conditions,

$$T_{iz}^a = 0, \quad z = l \quad (2.144)$$

$$T_{xz}^a = T_{xz}^b, \quad T_{yz}^a = T_{yz}^b, \quad T_{zz}^b - T_{zz}^a = F, \quad z = d \quad (2.145)$$

$$u_j^a = u_j^b, \quad z = d \quad (2.146)$$

$$T_{iz}^b = 0, \quad u_j^b = u_j^s, \quad z = 0 \quad (2.147)$$

as well as the condition that when  $z \rightarrow -\infty$ ,  $u_j^s \rightarrow 0$  (which leads to  $\tilde{\alpha}_-^s = \tilde{\beta}_-^s = \tilde{\gamma}_-^s = 0$ ). We are left with 15 fields of

$$(\tilde{\alpha}_\pm^a, \tilde{\beta}_\pm^a, \tilde{\gamma}_\pm^a, \tilde{\alpha}_\pm^b, \tilde{\beta}_\pm^b, \tilde{\gamma}_\pm^b, \tilde{\alpha}_+^s, \tilde{\beta}_+^s, \tilde{\gamma}_+^s) \quad (2.148)$$

which can be solved from the 15 boundary conditions. Assuming  $\kappa d \ll 1$  and  $\kappa l \ll 1$ , we obtain

that all  $\tilde{\gamma}$  vanish, and

$$\tilde{\alpha}_+^a = \frac{F(1 + \sigma_s)[2 - 3\sigma_s + \sigma_c(-3 + 4\sigma_s)]}{2Y_s\kappa^2(-1 + \sigma_c)} \quad (2.149)$$

$$\tilde{\alpha}_-^a = \frac{F(\sigma_c - \sigma_s)(1 + \sigma_s)}{2Y_s\kappa^2(-1 + \sigma_c)} \quad (2.150)$$

$$\tilde{\beta}_+^a = -\frac{F(1 + \sigma_s)(-3 + 4\sigma_s)}{4Y_s\kappa^2(-1 + \sigma_c)} \quad (2.151)$$

$$\tilde{\beta}_-^a = \frac{F(1 + \sigma_s)}{4Y_s\kappa^2(1 - \sigma_c)} \quad (2.152)$$

$$\tilde{\alpha}_+^b = \frac{F(1 + \sigma_s)[2 - 3\sigma_s + \sigma_c(-3 + 4\sigma_s)]}{2Y_s\kappa^2(-1 + \sigma_c)} \quad (2.153)$$

$$\tilde{\alpha}_-^b = \frac{F(\sigma_c - \sigma_s)(1 + \sigma_s)}{2Y_s\kappa^2(-1 + \sigma_c)} \quad (2.154)$$

$$\tilde{\beta}_+^b = \frac{F[Y_s(1 + \sigma) - Y_c(-3 + \sigma_s + 4\sigma_s^2)]}{4Y_s\kappa^2(-1 + \sigma_c)} \quad (2.155)$$

$$\tilde{\beta}_-^b = \frac{F[Y_s(1 + \sigma_c) - Y_c(1 + \sigma_s)]}{4Y_s\kappa^2(-1 + \sigma_c)} \quad (2.156)$$

$$\tilde{\alpha}_+^s = \frac{F(1 + \sigma_s)(-1 + 2\sigma_s)}{Y_s\kappa^2} \quad (2.157)$$

$$\tilde{\beta}_+^s = -\frac{F(1 + \sigma_s)}{Y_s\kappa^2}. \quad (2.158)$$

We can therefore obtain the strain tensor in the frequency domain for the coating, the nonzero elements for region (a) are given by

$$S_{xx}^a = \frac{Fk_x^2(-1 + 2\sigma_s)(1 + \sigma_s^2)}{Y_s\kappa^2} \quad (2.159)$$

$$S_{yy}^a = \frac{Fk_y^2(-1 + 2\sigma_s)(1 + \sigma_s^2)}{Y_s\kappa^2} \quad (2.160)$$

$$S_{xy}^a = S_{yx} = \frac{Fk_x k_y(-1 + 2\sigma_s)(1 + \sigma_s^2)}{Y_s\kappa^2} \quad (2.161)$$

$$S_{zz}^a = F \frac{\sigma_c(-1 + \sigma_s + 2\sigma_s^2)}{Y_s(-1 + \sigma_c)} \quad (2.162)$$

while those in region (b) are given by

$$S_{xx}^b = \frac{Fk_x^2(-1 + 2\sigma_s)(1 + \sigma_s^2)}{Y_s\kappa^2} \quad (2.163)$$

$$S_{yy}^b = \frac{Fk_y^2(-1 + 2\sigma_s)(1 + \sigma_s^2)}{Y_s\kappa^2} \quad (2.164)$$

$$S_{xy}^b = S_{yx} = \frac{Fk_x k_y(-1 + 2\sigma_s)(1 + \sigma_s^2)}{Y_s\kappa^2} \quad (2.165)$$

$$S_{zz}^b = F \left[ \frac{-(1 + 2\sigma_c)}{Y_c} - \frac{\sigma_c(-1 + \sigma_s + 2\sigma_s^2)}{Y_s(1 - \sigma_c)} \right]. \quad (2.166)$$

Using linear superposition, as well as taking the appropriate limits of the above solution, it is straightforward to obtain elastic deformations in all the setups required in order to obtain cross spectra between different noises.

## 2.11 Appendix C: Definition of loss angle

In the past [11], the coating loss angle was defined in association with the parallel and perpendicular coating strains. The equation is written as

$$\phi_{\text{coated}} = \phi_{\text{sub}} + \frac{\delta U_{\parallel} d}{U} \phi_{\parallel} + \frac{\delta U_{\perp} d}{U} \phi_{\perp} \quad (2.167)$$

where  $\delta U_{\parallel}$  and  $\delta U_{\perp}$  are the dissipation energy density in parallel and perpendicular coating strains

$$\delta U_{\parallel} = \int_s \frac{1}{2} (S_{xx} T_{xx} + S_{yy} T_{yy}) dx dy \quad (2.168)$$

$$\delta U_{\perp} = \int_s \frac{1}{2} S_{zz} T_{zz} dx dy \quad (2.169)$$

and where  $S_{ij}$  are the strains and  $T_{ij}$  are the stresses. While such a definition seems to be compatible with the symmetry of the system, the quantities  $\delta U_{\parallel}$  and  $\delta U_{\perp}$  cannot be used as energy, since in certain scenarios they each can become negative.

For example, if we have a cube with surface area of each side  $A$  (Poisson's ratio  $\sigma$ , Young's modulus  $Y$ ), we uniformly apply two pairs of forces, one pair with magnitude  $f$  on opposite  $yz$  planes, the other with magnitude  $F$  on opposite  $xy$  planes, with  $f \ll F$ , as shown in Figure 2.18. According to definition of Young's modulus and Poisson's ratio, up to leading order in  $f/F$  the nonvanishing strains are,

$$S_{zz} = -\frac{F/A}{Y}, \quad S_{xx} = S_{yy} = \sigma \frac{F/A}{Y}. \quad (2.170)$$

On the other hand, for stress, we have, up to leading order in  $f/F$ ,

$$T_{xx} = -f/A, \quad T_{yy} = 0, \quad T_{zz} = -F/A. \quad (2.171)$$

As a consequence, we have

$$\delta U_{\parallel} = S_{xx} T_{xx} + S_{yy} T_{yy} = -\sigma f F / (A^2 Y) < 0 \quad (2.172)$$

which means  $\delta U_{\parallel}$  is not a reasonable candidate for energy, at least with  $\sigma \neq 0$ . Since it is also true that  $S_{xx} T_{xx} < 0$  we will arrive at

$$\delta U_{\perp} = S_{zz} T_{zz} < 0 \quad (2.173)$$

if we take this configuration and rotate for 90 degrees around the  $y$  axis, such that  $x$  rotates into  $z$ .

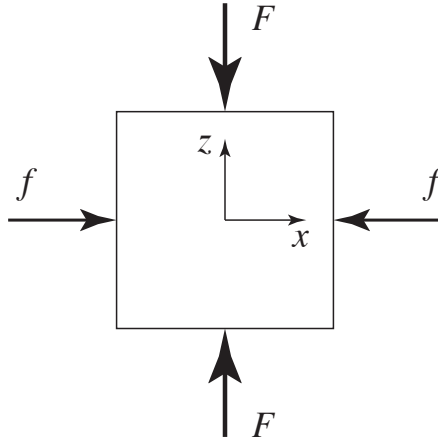


Figure 2.18: Solid cube with two pairs of forces applied on the side:  $f \ll F$

One reasonable way of defining the loss angle is to derive from the fundamental elastic energy equation. The general form of the stored elastic energy density  $U$  can be written as

$$U = \frac{1}{2}K\Theta^2 + \mu\Sigma_{ij}\Sigma_{ij} \quad (2.174)$$

$$U_B = \frac{1}{2}K\Theta^2 \quad (2.175)$$

$$U_S = \mu\Sigma_{ij}\Sigma_{ij}. \quad (2.176)$$

Where  $K$  is called the *bulk modulus* and  $\mu$  is the *shear modulus*. In the calculation, we use Young's modulus  $Y$  and the Poisson's ratio  $\sigma$  instead of  $K$  and  $\mu$ . Their relation is given in Eq.(15). The expansion  $\Theta$  and shear  $\Sigma$  are both irreducible tensorial parts of the strain tensor  $S$ .

$$\Theta = S_{ii} \quad (2.177)$$

$$\Sigma = \frac{1}{2}(S_{ij} + S_{ji}) - \frac{1}{3}g_{ij}S_{kk} \quad (2.178)$$

Note that the expansion and shear energy  $U_B$  and  $U_S$  is always positive, so it is consistent to define loss angle by  $\phi_B$  and  $\phi_S$ .

## 2.12 Appendix D: Advanced LIGO Style Coating [25]

In Table 2.7, we provide the structure of the coating optimized jointly for dichroic operation and thermal noise (baseline parameter, neglecting penetration).

$j$	$l_j$				
1–5	0.497325	0.208175	0.289623	0.237274	0.250176
6–10	0.245330	0.249806	0.240129	0.270968	0.224129
11–15	0.251081	0.259888	0.260826	0.213460	0.290468
16–20	0.214524	0.273240	0.230905	0.259924	0.230020
21–25	0.275429	0.233086	0.270385	0.208581	0.273798
26–30	0.249741	0.267864	0.204698	0.292317	0.209712
31–35	0.278560	0.220264	0.282694	0.221687	0.268559
36–38	0.233460	0.270419	0.223050		

Table 2.7: Structure of an advanced LIGO-like coating optimized jointly for dichroic operation and thermal noise. Thickness of each layer is given in units of wavelength (for light with vacuum-wavelength of 1064 nm) are listed here for the 38 layers. Note that  $l_{1,3,5,\dots}$  are  $\text{SiO}_2$  layers, while  $l_{2,4,6,\dots}$  are  $\text{Ta}_2\text{O}_5$  layers.

## Bibliography

- [1] D. Meiser et. al., Phys. Rev. Lett. **102**, 163061 (2009).
- [2] LIGO Scientific Collaboration, Rep. Prog. Phys. **72** (2009).
- [3] G. M. Harry (for the LIGO Scientific Collaboration), Class. Quantum Grav. **27**, 084006 (2010).
- [4] B. Willke et al., Class. Quantum Grav. **23** S207 (2006).
- [5] The Virgo Collaboration, *Advanced Virgo Baseline Design*, note VIR027A09, May 16, (2009).
- [6] K. Kuroda (on behalf of the LCGT Collaboration), Class. Quantum Grav. **27**, 084004 (2010).
- [7] H. J. Kimble, B. L. Lev and J. Ye, Phys. Rev. Lett. **101**, 260602 (2008).
- [8] M. Evans et al., Phys. Rev. D **78**, 102003 (2008).
- [9] G. González and P. Saulson, J. Acoust. Soc. Am. **96**, 207 (1994).
- [10] Y. Levin, Phys. Rev. D **57**, 659 (1998).
- [11] G. M. Harry, A. M. Gretarsson, P. R. Saulson, S. E. Kittelberger, S. D. Penn, W. J. Startin, S. Rowan, M. M. Fejer, D. R. M. Crooks, G. Cagnoli, J. Hough and N. Nakagawa, Class. Quantum Grav. **19**, 897 (2002).
- [12] A. Gurkovsky and S. Vyatchanin, Phys. Lett. A **374**,3267 (2010)
- [13] H. B. Callen and T. A. Welton, Phys. Rev. **83**, 34 (1951).
- [14] L. D. Landau and E. M. Lifshitz, *Theory of Elasticity (Course of Theoretical Physics)*, Pergamon (1981).
- [15] I.W. Martin, Class. Quantum Grav. **27**, 225020 (2010)

- [16] G.M. Harry et al., *Class. Quantum Grav.* **24**, 405, (2007).
- [17] S.D. Penn et al., *Class. Quantum Grav.* **20** 2917, (2003).
- [18] R. Waynant and M. Ediger, *Electro-Optics Handbook*, McGraw-Hill (1994)
- [19] M. M. Fejer, S. Rowan, G. Cagnoli, D. R. M. Crooks, A. Gretarsson, G. M. Harry, J. Hough, S. D. Penn, P. H. Sneddon and S. P. Vyatchanin, *Phys. Rev. D* **70**, 082003 (2004).
- [20] P. J. Martin, A. Bendavid, M. Swain, R. P. Netterfield, T. J. Kinder, W. G. Sainty, D. Drage and L. Wielunski, *Thin Solid Films* **239**, 181 (1994).
- [21] G. M. Harry, M. R. Abernathy, A. E. Becerra-Toledo, H. Armandula, E. Black, K. Dooley, M. Eichenfield, C. Nwabugwu, A. Villar, D. R. M. Crooks, G. Cagnoli, J. Hough, C. R. How, I. MacLaren, P. Murray, S. Reid, S. Rowan, P. H. Sneddon, M. M. Fejer, R. Route, S. D. Penn, P. Ganau, J. M. Mackowski, C. Michel, L. Pinard and A. Remillieux, *Class. Quantum Grav.* **24**, 405 (2007).
- [22] S. D. Penn, P. H. Sneddon, H. Armandula, J. C. Betzwieser, G. Cagnoli, J. Camp, D. R. M. Crooks, M. M. Fejer, A. M. Gretarsson, G. M. Harry, J. Hough, S. E. Kittelberger, M. J. Mortonson, R. Route, S. Rowan and C. C. Vassiliou, *Class. Quantum Grav.* **20**, 2917 (2003).
- [23] Y. Nakagawa et al., *Electronics and Communications in Japan*, (**84**), 46 (2001).
- [24] J. Stone, *Journal of Lightwave Technology* **6**, 1245 (1988).
- [25] G. Billingsley, private communication.
- [26] J. Agresti, G. Castaldi, R. DeSalvo, V. Galdi, V. Pierro, and I. M. Pinto, LIGO-P060027-00-Z.
- [27] J. A. Nelder and R. J. Mead, *The Computer Journal*, **7**, (1965).
- [28] W. H. Press, S. A. Teukolsky, W. T. Vetterling, B. P. Flannery, “Numerical Recipes: The Art of Scientific Computing” (Third Edition), Section 10.5, Cambridge University Press (2007).
- [29] A. Heptonstall, G. Cagnoli, J. Hough, S. Rowan, *Phys. Lett. A* **354**, 353, (2006).
- [30] S. D. Penn, A. Ageev, D. Busby, G. M. Harry, A. M. Gretarsson, K. Numata, P. Willems, *Phys. Lett. A* **352**, 3, (2006).
- [31] L. H. Donnell, NACA Report No. 479, (1933).
- [32] Robert D. Blevins, *Formulas for Natural Frequency and Mode Shape*, Van Nostrand Reinhold Company, New York (1979).

- [33] W. Flügge, *Stresses in Shells*, Springer-Verlag, New York(1973)
- [34] N. M. Kondratiev, A. G. Gurkovsky, and M. L. Gorodetsky, Phys. Rev. D **84**, 022001, (2011)
- [35] S. E. Whitcomb, private communication.
- [36] D. F. Nelson and M. Lax, Phys. Rev. Lett. **24** (1970).
- [37] V. B. Braginsky, M. L. Gorodetsky, and S. P. Vyatchanin, Phys. Lett. A **271**, 303, (2000).

## Chapter 3

# Effects of Mirror Aberrations on Laguerre-Gaussian Beams in Interferometric Gravitational-Wave Detectors

A fundamental limit to the sensitivity of optical interferometers is imposed by Brownian thermal fluctuations of the mirrors' surfaces. This thermal noise can be reduced by using larger beams which “average out” the random fluctuations of the surfaces. It has been proposed previously that wider, higher-order Laguerre-Gaussian modes can be used to exploit this effect. In this article, we show that susceptibility to spatial imperfections of the mirrors' surfaces limits the effectiveness of this approach in interferometers used for gravitational-wave detection. Possible methods of reducing this susceptibility are also discussed.

---

Originally published as T. Hong, J. Miller, H. Yamamoto, R. Adhikari, and Y. Chen, *Physics Review D* **84**,102001(2011).

### 3.1 Introduction

Long-baseline laser-interferometer gravitational-wave detectors, such as those used in LIGO [1], VIRGO [2], GEO600 [3], and LCGT [4], use Michelson interferometry to measure tiny differential changes in arm length induced by gravitational waves. Spurious motions of a mirror’s surface, such as those caused by seismic, thermal, and radiation-pressure fluctuations, can compromise the sensitivity to gravitational wave signals. Brownian thermal noise in the dielectric mirror coatings, or *coating Brownian noise*, is known to be the dominant noise source in the intermediate frequency band of Advanced LIGO [5] and other similar interferometers.

As described by the fluctuation-dissipation theorem [6, 7], dissipation via internal friction in the dielectric coatings must lead to fluctuations in the thickness of the coatings. When the beam spot size is much larger than the coating thickness, coating Brownian noise at different locations on the mirror’s surface can be considered to be uncorrelated. This leads to the following scaling law [8, 9],

$$S_x \propto \frac{\int I^2(\vec{r}) d^2\vec{r}}{\left[ \int I(\vec{r}) d^2\vec{r} \right]^2} \quad (3.1)$$

which describes how the power spectrum of observed coating Brownian noise  $S_x$  depends on the intensity profile  $I(\vec{r})$  of the optical field which is used to read out the mirror motion; i.e., the coating Brownian noise power spectrum is inversely proportional to the effective area of the optical mode.

Mode	Mirror Shape	Suppression Factor	Ref.
LG <sub>3,3</sub>	Spherical	1.61	[10]
Mesa	Sombrero	1.53	[11, 12]
Conical	Conical	2.30	[13]

Table 3.1: Beam shapes that have been considered for use in gravitational-wave detectors, mirror shapes that support them and their thermal-noise suppression factors (in power) for advanced LIGO parameters (cavity length  $L = 4$  km, mirror radius of 17 cm)

Three families of optical modes have so far been considered for mitigating coating thermal noise (see Table 3.1). Among these modes, only the higher-order Laguerre-Gauss mode, LG<sub>3,3</sub>, can be supported by optical cavities employing standard spherical mirrors. Due to the practical advantages associated with the use of spherical mirrors, experimental testing of LG<sub>3,3</sub> modes has begun. It has thus far been demonstrated that these modes can be generated with high efficiency and resonated in tabletop cavities with small mirrors [14, 15].

An unpleasant property of higher-order LG modes is that each LG <sub>$p,l$</sub>  mode is  $2p + |l| + 1$  fold degenerate, the LG<sub>3,3</sub> mode being 10 fold degenerate. Mirror figure errors will inevitably split each formerly degenerate mode into  $2p + |l| + 1$  single modes with eigenfrequencies which depend on the particulars of the figure error. By contrast, a nondegenerate mode, under the same figure error, will

usually remain as a single, weakly-perturbed nondegenerate mode.

In this work we explore the effects of  $LG_{3,3}$  modal degeneracy quantitatively, via both numerical and analytical methods. Guided by experience with existing interferometers we have selected contrast defect as our metric of interferometer performance.

To ground our investigation in reality we incorporate mirror figure errors derived from measurements of the first advanced LIGO optics. The creation of these maps is described in Section 3.2.

In Section 3.3, we use perturbation theory to analyze the effect of such mirror perturbations on the degenerate subspace which includes the  $LG_{3,3}$  mode. We then use this newly perturbed set of modes to calculate the contrast degradation of a single Fabry-Perot arm cavity analytically in Section 3.4.1.

In Section 3.4.2, we utilize a sophisticated numerical field propagation code to confirm analytical results and examine a more complicated interferometer topology.

In Sec. 3.5, we explore two methods of mitigating contrast degradation; neither of the methods was ultimately successful.

## 3.2 Mirror Figure Errors

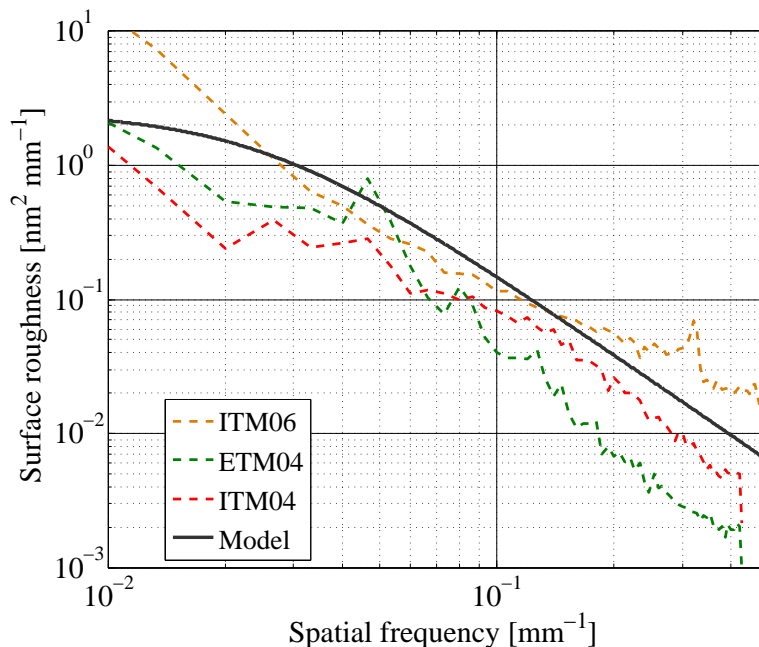


Figure 3.1: Power spectral densities of uncoated mirror surface roughness. The dashed lines are the measured spectra of three Advanced LIGO arm cavity mirrors. A model approximating these spectra (black trace, see (3.2)) was created to generate the random maps used in our work.

In this work we investigate the consequences of realistic mirror imperfections on the performance of the LG<sub>3,3</sub> mode. The parameters of the particular imperfections applied are therefore significant.

Fig. 3.1 illustrates measured surface roughness power spectral densities of selected advanced LIGO mirror substrates, prior to the application of dielectric mirror coatings (the PSD plots end up to spatial wavelength of 2 mm). Based on the measured initial LIGO optics and small optics of advanced LIGO, we construct an analytical model (solid black line) which falls roughly in the middle of advanced LIGO test mass PSDs,

$$S(f) \propto (1 + (0.04f)^2)^{-1}. \quad (3.2)$$

This one-dimensional function was used to generate random mirror maps which are statistically similar to those one might find in an advanced gravitational-wave interferometer. Such random mirror maps, used in all aspects of this investigation, were constructed by multiplying each point of the amplitude spectral density's magnitude by a random complex number  $a + ib$  before transforming back to coordinate space and appropriately scaling the result to yield the desired RMS. Scalars  $a$  and  $b$  are drawn independently from a normal distribution with zero mean and a standard deviation of one [16].

The entire surface is fit by Zernike polynomials and the terms corresponding to Piston, tilt and power (Zernike polynomials  $Z_0^0, Z_1^{\pm 1}, Z_2^0$ ) were removed from our maps (the Piston term is irrelevant because the lock process adjusts the microscopic length; the tilt term is removed to represent the alignment control; the ROC of the generated surface is corrected by hand). The RMS values quoted are calculated after this subtraction.

Fig. 3.2 shows the surface figure of one map generated using our algorithm. This map is typical of a larger population and was selected as a reference to be used in all analytical calculations.

### 3.3 Degenerate Perturbation-Theory Analysis

#### 3.3.1 Laguerre-Gauss modes

The Laguerre-Gauss modes (LG <sub>$p,l$</sub> ) are a set of circularly symmetric modes which can be written in cylindrical coordinates as [17]

$$\begin{aligned} u_{p,l}(r, \phi, z) = & \sqrt{\frac{2p!}{\pi(|l|+p)!}} \frac{1}{\omega(z)} \left[ \frac{\sqrt{2}r}{\omega(z)} \right]^{|l|} \\ & \times L_p^{|l|} \left[ \frac{2r^2}{\omega^2(z)} \right] \exp[i(2p + |l| + 1)\psi(z)] \\ & \times \exp \left[ -ik \frac{r^2}{2R(z)} + il\phi \right] \exp \left[ \frac{-r^2}{\omega^2(z)} \right], \end{aligned} \quad (3.3)$$

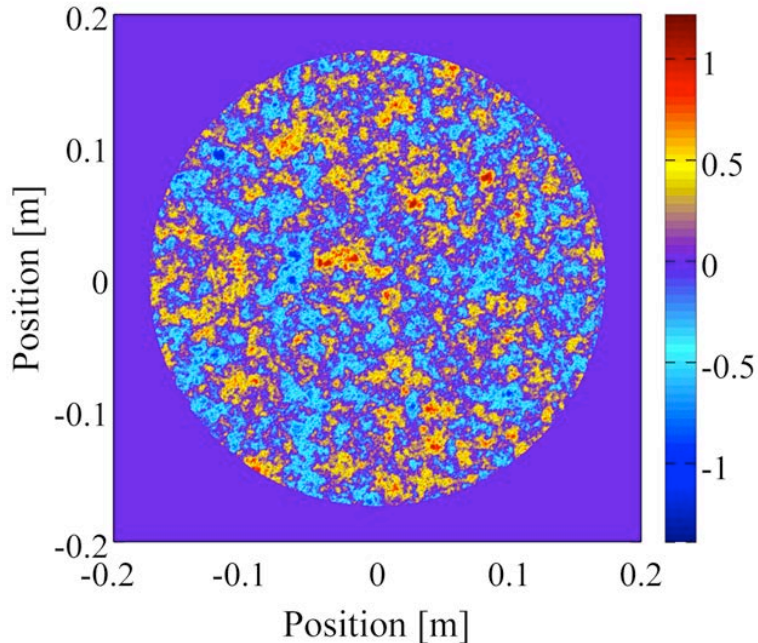


Figure 3.2: Surface figure (in nm) of a typical generated phase map with Piston, tilt, power and astigmatism terms subtracted

where  $\omega(z)$  is the beam radius,  $\psi(z)$  is the Gouy phase, and  $R(z)$  is phase front curvature of the beam.  $L_p^{|l|}(x)$  is the associated Laguerre polynomial where  $p \geq 0$  and  $l$  are the radial and azimuthal indices, respectively.

The mode selectivity of the cavity is determined by the cavity finesse and the mode dependent phase shift  $(2p + |l| + 1)\psi(z)$ . From this we see that the  $\text{LG}_{p,l}$  mode has  $2p + |l| + 1$  degenerate eigenmodes. For example,  $\text{LG}_{3,3}$  belongs to a ten fold degenerate space, which can be spanned by:  $\text{LG}_{3,\pm 3}$ ,  $\text{LG}_{0,\pm 9}$ ,  $\text{LG}_{1,\pm 7}$ ,  $\text{LG}_{2,\pm 5}$  and  $\text{LG}_{4,\pm 1}$ .

Coating Brownian noise power is proportional to the integral of beam intensity, as the scaling law (Eq. (3.1)) indicates. In Table 3.2, we present theoretical thermal noise suppression factors for selected LG modes. To permit a fair comparison, the widths of all modes considered here and henceforth were chosen to be 0.018 m, which yield a clipping loss [18], due to the finite size of the cavity mirrors, of around 1 ppm. We see that the  $\text{LG}_{3,3}$ , considered by many as the leading candidate for use in gravitational wave interferometers, offers a theoretical thermal noise reduction factor of  $\sim 1.6$  compared to a standard Gaussian beam ( $\text{LG}_{0,0}$ ). The transverse intensity distribution of the  $\text{LG}_{3,3}$  mode is presented in Fig. 3.3.

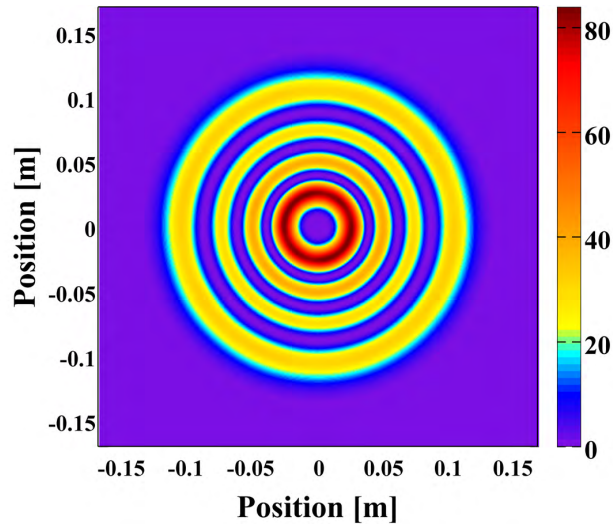


Figure 3.3: Normalized intensity distribution of the  $LG_{3,3}$  mode at the mirror position ( $\omega_0 = 0.021$  m,  $z = 1997.25$  m)

	$LG_{0,0}$	$LG_{0,9}$	$LG_{1,7}$	$LG_{2,5}$	$LG_{3,3}$	$LG_{4,1}$
Beam radius (mm)	9.96	16.5	17.3	17.9	18.2	18.4
Suppression Factor	1	1.51	1.62	1.64	1.61	1.51

Table 3.2: Suppression factors of thermal noise (in power spectral density) for LG modes with a fixed clipping loss of 1 ppm

### 3.3.2 Application of Degenerate Perturbation Theory to the Perturbed Fabry-Perot Cavity

The combination of eigenmodes excited in a cavity depends on the composition of the incident field and on the properties of the cavity itself. In this section we discuss how first-order perturbation theory can be applied to this problem. We first explore how mirror figure error breaks the degeneracy of LG cavity modes before describing the phase shift each mode experiences in an optical cavity and finally constructing the total field (prompt plus leakage) reflected from a perturbed Fabry-Perot resonator.

#### 3.3.2.1 Mode Splitting

Fig. 3.4 illustrates light propagation in a simple Fabry-Perot cavity, introducing the notation employed in our formalism.

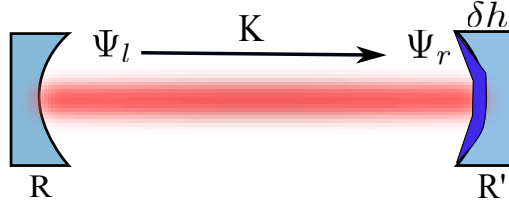


Figure 3.4: Fabry-Perot cavity with a perturbation  $\delta h(x, y)$  on the end mirror

We use the following standard method for propagating cavity fields,

$$\Psi_r(\vec{r}) = \int K(\vec{r}, \vec{r}') \Psi_l(\vec{r}') d^2 \vec{r}', \quad (3.4)$$

or  $|\Psi_r\rangle = \hat{K}|\Psi_l\rangle$ , where  $\Psi_r$  and  $\Psi_l$  are the electric fields near the right and left mirror, respectively, and  $K$  is the field propagator from the left mirror to the right

$$K(\vec{r}, \vec{r}') = \frac{ik}{2\pi L} e^{-\frac{ik}{2L} |\vec{r} - \vec{r}'|^2}. \quad (3.5)$$

Therefore, if  $|\psi\rangle$  is an eigenmode of the cavity,

$$|\psi\rangle = \hat{R}\hat{K}\hat{R}'\hat{K}|\psi\rangle, \quad (3.6)$$

where  $\hat{R}$  is the reflection operator of the left mirror and  $\hat{R}'$  is for the right. Hence,  $|\psi\rangle$  is an eigenmode of the operator  $(\hat{R}\hat{K}\hat{R}'\hat{K})$ .

We assume that the mirror on the left is ideal and study the consequences of applying a surface figure perturbation  $\delta h$  to the right hand (end mirror) optic. The reflection operator  $\hat{R}'$  can then be

written as

$$\hat{R}' = \hat{R}e^{2ik\delta h} \approx \hat{R}(1 + 2ik\delta h). \quad (3.7)$$

To obtain the real cavity eigenmodes, we need to solve for the eigenfunctions of  $(\hat{R}\hat{K}\hat{R}'\hat{K})$ . Note that the original LG<sub>33</sub> mode is an eigenfunction of an unperturbed cavity:

$$|33\rangle = (\hat{R}\hat{K}\hat{R}\hat{K})|33\rangle. \quad (3.8)$$

As introduced above, the LG<sub>33</sub> mode is degenerate with 9 other modes, each having eigenfrequency  $\omega_0$ , thus  $\hat{R}\hat{K}\hat{R}\hat{K}$  also has 10 degenerate eigenmodes at  $\omega_0$ .

For reasonable parameters, modes outside of this degenerate subspace are far enough from resonance that we may ignore them in this first-order analysis. Therefore, to good approximation, we can assume the new eigenmodes of the perturbed cavity are still members of the Hilbert space of the original 10 LG modes, which we represent by  $|i\rangle$ , ( $i=1,2,\dots,10$ ). These new eigenmodes, denoted  $|i'\rangle$ , are the eigenvectors of the matrix with elements  $\langle i|\hat{R}\hat{K}\delta h\hat{R}\hat{K}|j\rangle = \langle i|\delta h|j\rangle$ , ( $i, j = 1, 2, \dots, 10$ )

$$\begin{pmatrix} \langle 1|\delta h|1\rangle & \dots & \langle 1|\delta h|10\rangle \\ \vdots & \ddots & \vdots \\ \langle 10|\delta h|1\rangle & \dots & \langle 10|\delta h|10\rangle \end{pmatrix}. \quad (3.9)$$

Denoting the electric field of  $|i\rangle$  as  $\phi_i$ , we write

$$\langle i|\delta h|j\rangle = \iint \phi_i^*(x, y)\delta h(x, y)\phi_j(x, y) dx dy. \quad (3.10)$$

The frequency shift of the degenerate modes introduced by the perturbation is then proportional to the eigenvalues of the matrix

$$\omega_{i'} = \frac{kc}{L}\langle i'|\delta h|i'\rangle, \quad (3.11)$$

where  $k = 2\pi/\lambda$  is the optical wavenumber,  $c$  is the speed of light and  $L$  is the cavity length.

This quantity was evaluated using the reference map shown above (Fig. 3.2). The RMS roughness of the reference was scaled to be similar to those of measured Advanced LIGO mirror surfaces (0.3 nm RMS). Results are presented in Fig. 3.5. Here the frequency splits are given in Hertz ( $\omega/2\pi$ ). The frequency shifts are one order of magnitude smaller than the advanced gravitational-wave interferometer's cavity linewidth. Thus, multiple perturbed eigenmodes will be partially resonant, radically distorting the shape of the output field.

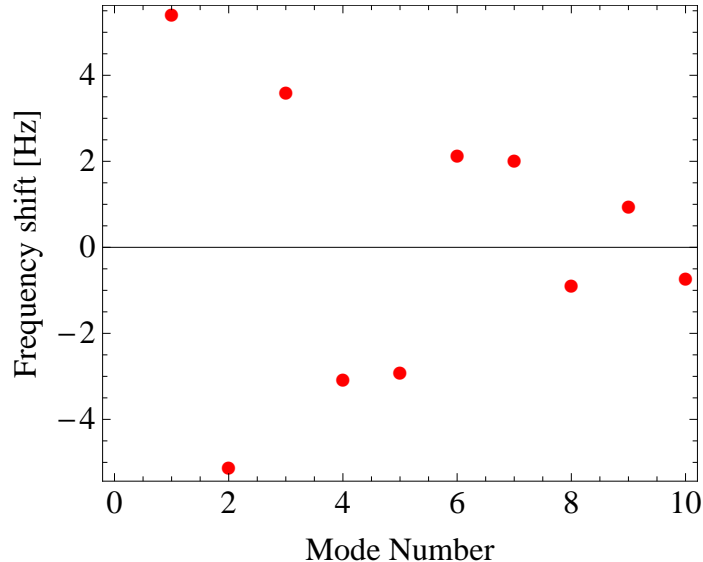


Figure 3.5: Frequency shift of LG modes introduced as a result of realistic mirror perturbations

### 3.3.2.2 The Modal Input-Output Equation

Above we have shown that mirror figure errors will lift the modal degeneracy and split the degenerate  $\text{LG}_{3,3}$  space into distinct states with unique eigenfrequencies. We now consider how each of these modes interacts with a cavity.

For any mode  $|\text{in}\rangle$  injected into an ideal cavity, there exists a frequency dependent phase shift between the input and total reflected or *output* fields. This can be written as [19]

$$|\text{out}\rangle = \frac{\gamma_c + i(\omega - \omega_0)}{\gamma_c - i(\omega - \omega_0)} |\text{in}\rangle, \quad (3.12)$$

where  $\omega$  is the frequency of the injected field,  $\omega_0$  is the resonant frequency of the cavity closest to  $\omega$  and  $\gamma_c = cT_{\text{input}}/4L$  is the cavity pole frequency in Hertz. Here,  $T_{\text{input}}$  denotes the power transmissivity of the cavity input mirror; the transmissivity of the end mirror is assumed to be zero.

Suppose that this ideal cavity hosts an  $N$ -fold degenerate space and that we inject an input mode  $|\text{in}\rangle$  which belongs to this space. If the  $N$ -fold degeneracy is broken by some mirror figure error, the new eigenmodes can be approximated by  $|n\rangle$ ,  $n = 1, 2, \dots, N$ , where each mode still belongs to the original subspace, but has a new eigenfrequency  $\omega_n$ . As we shall see in Appendix 3.7, this is justified as long as the cavity finesse is high enough and the eigenfrequencies of the non-degenerate modes are well separated from this subspace.

The output from the perturbed cavity can be obtained by projecting the input mode  $|\text{in}\rangle$  onto

the new basis  $|n\rangle$  and calculating the phase shifts using the following relation:

$$|\text{out}\rangle = \sum_{n'=1}^N \frac{\gamma_c + i(\omega - \omega_{n'})}{\gamma_c - i(\omega - \omega_{n'})} |n'\rangle \langle n'|\text{in}\rangle. \quad (3.13)$$

This procedure was applied to the  $\text{LG}_{3,3}$  degenerate space using the resonant frequencies of the previous section,  $\omega_n$ . With the reference phase map scaled to 0.3 nm RMS, the intensity profile of the resulting output mode is shown in Fig. 3.6.

### 3.4 Contrast Defect

In gravitational-wave interferometers, contrast defect is defined as the ratio of the minimum possible optical power at the anti-symmetric (dark) port to the power incident on the beamsplitter. This quantity can be expressed as

$$C = \frac{P_{\text{AS}}}{P_{\text{X}} + P_{\text{Y}}}, \quad (3.14)$$

where X and Y are labels for the two arm cavities,  $P_{\square} = \iint_{\mathbb{R}^2} (\Psi_{\square}^{\text{out}})^* \Psi_{\square}^{\text{out}} dx dy$  and  $\Psi_{\text{AS}}^{\text{out}} = \Psi_{\text{X}}^{\text{out}} - \Psi_{\text{Y}}^{\text{out}}$  represents the field at the anti-symmetric port (AS) of the interferometer.

In principle, the dark port could be completely dark. However, the presence of intentional imbalances in the arms (finite beamsplitter size, Schnupp asymmetry, etc.) and unintentional imperfections (mirror shape, scatter loss, mirror motion, etc.) result in imperfect destructive interference between the fields which recombine at the beamsplitter. This imperfect interference leads to the leakage of some ‘junk’ light to the dark port where the gravitational-wave signal is also detected. Excess light at the dark port can lead to a degradation of sensitivity via several mechanisms and compromise the robust operation of interferometer longitudinal and alignment control systems [20, 21]. Contrast defect is thus a useful metric to employ when comparing interferometer configurations.

The above perturbation analysis shows that the fields resonating in the arm cavities of a real interferometer will no longer be pure  $\text{LG}_{3,3}$  modes. Further, the relative amplitudes of the quasi-degenerate modes are strongly dependent on mirror properties, which will, in general, be different for each arm. Hence the perturbed arm cavity fields will interfere imperfectly at the beamsplitter. We therefore expect an  $\text{LG}_{3,3}$  interferometer to exhibit a larger contrast defect than, e.g., an  $\text{LG}_{0,0}$  mode. We now test this hypothesis by analytical and numerical means.

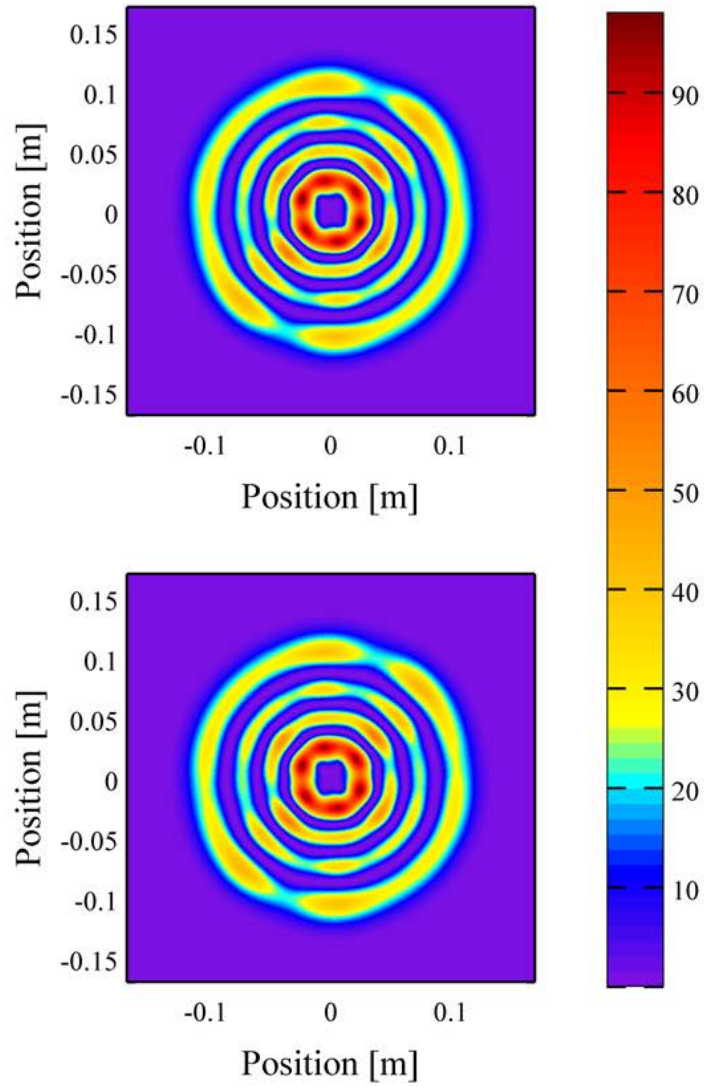


Figure 3.6: Intensity distributions of the total field reflected from an arm cavity whose end mirror was perturbed by the reference map. These distributions were calculated independently via two different techniques. Top—Analytic method described in Section 3.3.2. Bottom—FFT-based numerical simulation (see Section 3.4.2)

### 3.4.1 Analytic Calculation

According to Appendix 3.7, the contrast defect in an interferometer with one perfect arm cavity and one perturbed arm cavity, can be analytically written as

$$\epsilon = 1 - |\langle \text{in} | \text{out} \rangle|, \quad (3.15)$$

when the mirror perturbations are sufficiently small ( $\epsilon \ll 1$ ).

Appendix 3.7 also shows that when a frequency shift is small compared with the line width of the cavity, i.e.  $\omega - \omega_n \ll \gamma$ , Eq. 3.15 can be approximated as

$$\epsilon = \left[ \sum_{n'} \langle 33 | \delta h | n' \rangle \langle n' | \delta h | 33 \rangle - \langle 33 | \delta h | 33 \rangle^2 \right] \left( \frac{8\sqrt{2}\pi}{\lambda T} \right)^2, \quad (3.16)$$

where

$$\langle 33 | \delta h | pl \rangle = \int \delta h (u_{33}^* u_{pl}) \, dx \, dy. \quad (3.17)$$

Alternatively, this can be written as

$$\epsilon = \left[ \frac{(8\sqrt{2}\pi)}{\lambda T} \right]^2 \delta z^2, \quad (3.18)$$

where

$$\delta z^2 = \sum_{\substack{2p+|l|=10 \\ (p,l) \neq (3,3)}} |\langle 33 | \delta h | pl \rangle|^2. \quad (3.19)$$

This suggests that in order to minimize contrast defect, one must strive to suppress the projection of  $\delta h$  onto the 9 complex basis functions, given by  $u_{33}^* u_{pl}$ . Since these functions are complex and  $\delta h$  is real, this actually corresponds to 18 basis functions.

Based on Eq. (3.13), the contrast defect has been evaluated analytically in the case that only the end mirror (ETM) of one cavity is perturbed with the reference phase map of Fig. 3.2. The perturbation for different RMS values was obtained by rescaling the reference phase map. The results are shown in Fig. 3.7.

One can show that, for small perturbations, perturbing two cavity mirrors using phase maps derived from the same power spectral density function, will, on average, result in twice the contrast defect when compared to perturbations of a single mirror. However, depending on the spatial correlations between the mirrors, the contrast defect can be as much as twice the average in some cases.

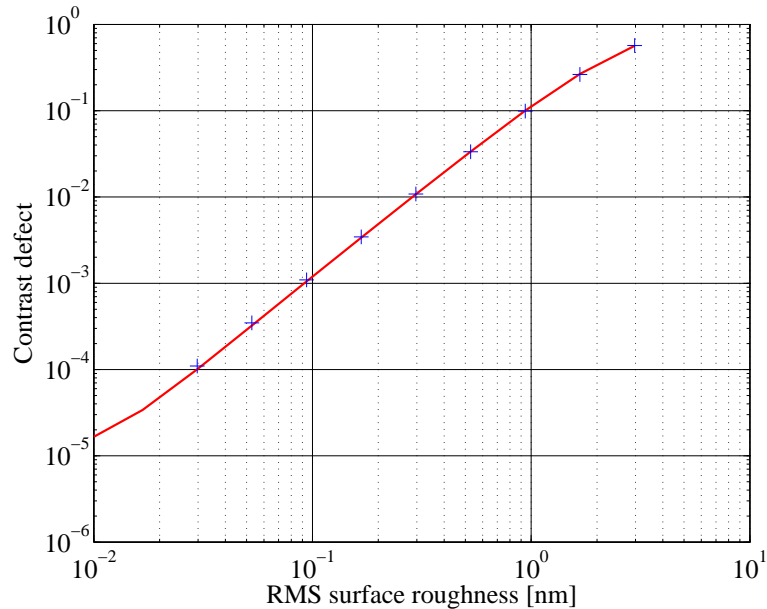


Figure 3.7: Contrast defect with the ETM of one cavity perturbed by rescaling the reference phase map: Solid red is from the analytical calculation, blue marker is from the FFT calculation.

### 3.4.2 Numerical Calculation

To confirm the results obtained via perturbation theory and to extend our analysis to more complicated configurations, a parallel investigation was carried out using numerical methods. We utilized an FFT-based field propagation tool—the stationary interferometer simulation (SIS) [23].

SIS is predominantly used to inform the design of the advanced LIGO interferometers and is under continuous development at Caltech’s LIGO laboratory. SIS employs an iterative procedure to find the stationary fields for a given optical configuration and input beam. Mirror surface maps can be generated from user-defined power spectral density functions, allowing one to study the effects of various hypothetical mirror aberrations. Cavity systems are ‘locked’ using a Pound-Drever-Hall signal [24] to realize an operating condition similar to that which would be observed experimentally.

SIS was used to model advanced LIGO Fabry-Perot arm cavities supporting  $LG_{0,0}$ ,  $LG_{3,3}$  and nearly concentric mesa modes [11, 12]. The parameters of the  $LG_{3,3}$  and mesa cavities (see Table 3.4.2) were adjusted to yield systems with round-trip diffraction loss equivalent to that of the fiducial  $LG_{0,0}$  resonator ( $\lesssim 1$  ppm). In each case the input beam remained fixed as the beam which was ideally coupled to an unperturbed cavity. To suppress the aliasing effect, a larger FFT grid of  $1024 \times 1024$  points on a  $0.7 \text{ m} \times 0.7 \text{ m}$  square was used for all modes.

Initially SIS was used to simulate a configuration identical to that studied analytically. Under these conditions both sets of results are in good agreement (better than 10%) (see Figs. 3.6, 3.7 and 3.8). The flexibility of SIS was then used to consider more complex simulations where both

	LG <sub>0,0</sub>	LG <sub>3,3</sub>	Mesa
R <sub>itm</sub>	1934 m	2857 m	1997.25 m
R <sub>etm</sub>	2245 m	2857 m	1997.25 m
Cavity g factor	0.83	0.16	—

Table 3.3: Cavity parameters used in the numerical simulations. All three resonators had a length of 3994.5 m. The mesa radii of curvature refer to the fiducial sphere from which the mesa correction profile is subtracted (cf. [11]). Cavity g factor is not well defined for mesa modes.

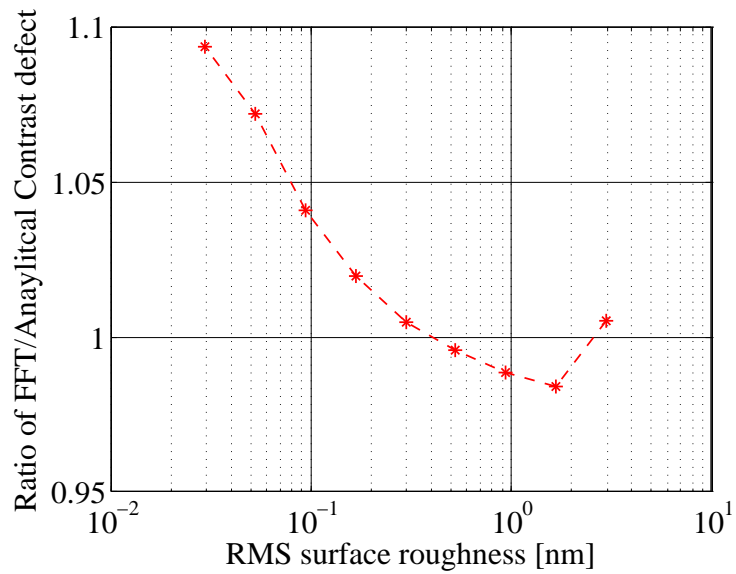


Figure 3.8: Ratio, numerical/analytical, of single-cavity contrast defects calculated with the end mirror perturbed by a 0.3 nm RMS figure error

cavity mirrors are perturbed and to emulate a Fabry-Perot Michelson interferometer. SIS was also employed to study high-RMS cases in which the analytic approximation breaks down.

For each simulation run, two random surfaces, with a specified RMS roughness and a spatial spectrum approximating that of the first Advanced LIGO mirrors (see Fig. 3.1), were generated and added to the profiles of the cavity mirrors. SIS then evaluated the field  $\Psi^{\text{out}}$  reflected from the cavity at its operating point, which is chosen from the cavity which is locked by using the Pound-Drever-Hall error signal.

Results from two discrete, single-cavity simulations, representing the  $X$  and  $Y$  arms of an interferometer, were then combined according to Eq. 3.14 to estimate interferometer contrast defect. Multiple trials were conducted at each value of RMS surface roughness with different random maps, allowing one to consider more than 100 unique arm cavity pairs. From these data, the mean and standard deviation of interferometer contrast defect were found as a function of mirror aberration RMS. Results for all three beams are shown in Fig. 3.9. The simulated contrast defect for Gaussian beam (TEM00) is consistent with the measured value of LIGO, which is around  $10^{-4}$  [25] and low enough for the effective detection.

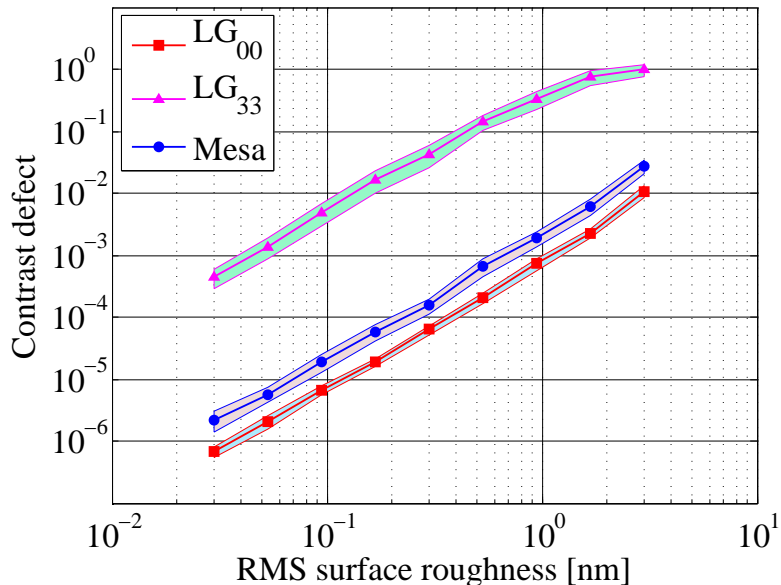


Figure 3.9: Interferometer contrast defect as a function of test mass surface roughness (all 4 mirrors are perturbed with random phase map at the same level of RMS). Solid markers report mean values of numerical results with the corresponding shaded regions illustrating one standard deviation (see 3.4.2), which is roughly four times higher than the trace in Fig. 3.7

Our numerical work confirms the result from perturbation theory; LG<sub>3,3</sub> interferometers are more sensitive to mirror surface roughness than those supporting a fundamental Gaussian mode.

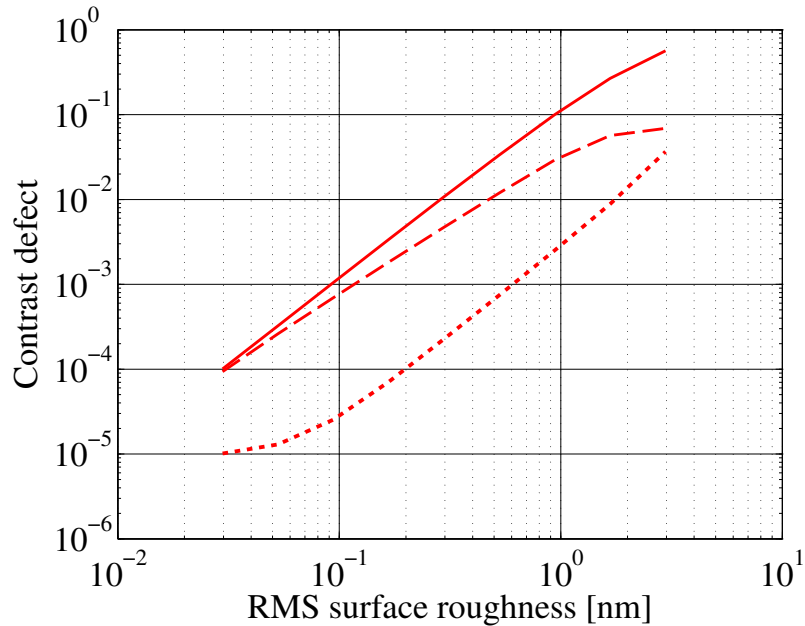


Figure 3.10: Analytic calculation with different conditions for reducing the contrast defect: solid curve is the original contrast defect; dashed line has corrective rings added to the phase map; dotted curve is with detuned injecting laser frequency

We further show that  $LG_{3,3}$  beams are also outperformed in this respect by nearly-concentric mesa beams, indicating that this sensitivity arises due to the properties of the Laguerre-Gauss mode itself and is not an inevitable handicap for all beams capable of mitigating mirror thermal noise.

## 3.5 Contrast Defect Improvement

Here we examine several methods of reducing the contrast defect.

### 3.5.1 Better Polishing

The most direct approach is to reduce the mirror figure error. However, reaching appropriate levels of surface roughness is beyond the capabilities of current technology. We estimate that in order to achieve reasonable performance,  $LG_{3,3}$  modes require mirrors with an RMS roughness roughly one order of magnitude smaller than is currently achievable (assuming the mirror coatings introduce no additional roughness, i.e., perfectly smooth, uniform coatings).

In the remainder of this section, we thus consider more unconventional means of reducing the contrast defect. Fig. 3.10 shows the results of each investigation.

### 3.5.2 Arm Cavity Detuning

Equation (3.12) shows that the output field varies with the frequency of light injected into a cavity, or equivalently with cavity length. This motivated us to study the variation in contrast defect as a function of arm cavity detuning.

It was found that detuning was effective in modifying contrast defect. Unfortunately, the large detuning necessary to recover good contrast had the effect of simultaneously reducing the optical power circulating in the cavity.

With a detuning of 100 Hz (approximately two cavity linewidths), it was possible to recover acceptable contrast (dotted line, Fig. 3.10). However, the same detuning causes the circulating power to drop by  $\sim 60\%$ . We therefore do not consider this approach to be viable in gravitational-wave interferometers where the injected frequency is usually tuned to maximize the optical power circulating in the coupled-cavity system. This technique can, however, be considered for experiments where the thermal noise needs to be reduced, but the cavity's stored power is not of concern.

### 3.5.3 Mirror Corrections

The increase in contrast defect observed when using  $\text{LG}_{3,3}$  modes in the presence of realistic surface roughness results from the presence of multiple pseudo-degenerate higher-order modes. Here we attempt to see if this effect can be mitigated by depositing corrective structures on the mirror's surface.

By introducing material at the nodes of the desired  $\text{LG}_{3,3}$  mode it was hoped that the unwanted modes from the same subspace could be suppressed.

As a concrete example, two Gaussian rings were added to the random phase map at nodes 1 and 3 of the  $\text{LG}_{3,3}$  mode. Each ring was of the form:

$$f(x, y) = \frac{\lambda}{20} e^{-\frac{(r-r_p)^2}{2(R/100)^2}} \quad (3.20)$$

where  $r_p$  indicates the position of the different nodes. The frequency split is plotted in Fig. 3.11. Compared to Fig. 3.5, the frequency splits under this condition are much larger, therefore the other degenerate modes will be harder to excite.

The analytically computed contrast defect for this case is plotted as the dashed line in Fig. 3.10. Although the defect is improved for values of surface roughness similar to that which is currently achievable, we find that, in order to significantly break the modal degeneracy, the height of the rings must be increased to such a degree that the induced scatter becomes unacceptably high ( $\sim 500$  ppm), reducing the stored power and thus the interferometer's phase sensitivity. We hence conclude that this approach is not promising.

At Caltech, Yamamoto has studied a similar approach whereby the mirror reflectivity is set to

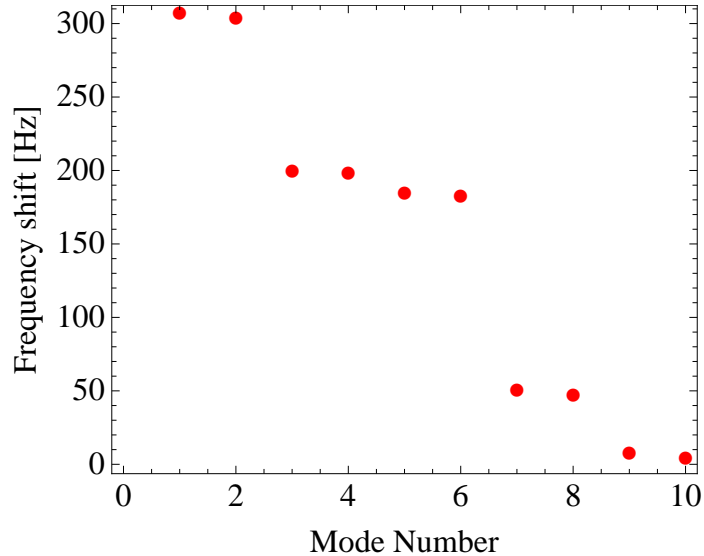


Figure 3.11: Frequency shift in LG modes introduced by adding rings to the reference phase map.

zero at the nodes of the  $\text{LG}_{3,3}$  mode [26]. This technique was found to be similarly unsuitable for application to gravitational wave interferometers.

### 3.5.4 Mode Healing

Previous work [27] has shown that the presence of a signal recycling cavity can substantially reduce the contrast defect in the case where the resonant mode in the interferometer is  $\text{TEM}_{0,0}$ . The higher order transverse modes are not resonant in the signal recycling cavity and are therefore suppressed. In the  $\text{LG}_{3,3}$  case, however, the signal cavity is resonant for the  $\text{LG}_{3,3}$  mode as well as all of the modes which are in the degenerate subspace. Therefore, our expectation is that there *would not* be a mode healing effect when using any higher order mode which can be split in this way. In the case where the signal recycling cavity is detuned to amplify the gravitational wave response at a particular frequency, the situation could be significantly more complicated due to the frequency splitting shown in Fig. 3.5. To quantitatively explore the effect of the compound cavity on degenerate modes, further analytic and numerical work is required.

## 3.6 Conclusions

In this paper, we use numerical analysis as well as perturbation theory to analyze the modes of a Fabry-Perot cavity resonating a  $\text{LG}_{3,3}$  beam. We prove that with realistic mirror figure errors, the real output mode of the cavity will change significantly, resulting in an unacceptable increase of the contrast defect.

We also investigate unconventional corrective techniques to reduce the contrast defect. While

they turn out to be unsuitable for quantum shot noise limited interferometers, they may have some utility for other classes of cavities. For  $LG_{3,3}$  modes to function effectively, we estimate that surface figure errors must be reduced to the order of  $10^{-2}$  nm RMS to achieve the required contrast defect of LIGO ( $\sim 10^{-4}$ ). Such precise polishing and coating uniformity will likely not be available for several years. Using high-order Laguerre-Gauss modes in standard spherical mirror cavities appears to be a poor choice in light of current technologies.

Numerical simulations using mesa and normal Gaussian beams show these beams are not so sensitive to figure errors. Future effort will be directed toward the construction of a new family of optical modes which can reduce the thermal noise impact while simultaneously being robust against mirror imperfections.

### 3.7 Appendix: Contrast Defect

Here we show that the contrast defects defined in equations (3.15) and (3.14) are equivalent in the limit of small perturbations. We denote the input and output field for the two cavities (X and Y) as  $|\text{in}\rangle_X, |\text{out}\rangle_X, |\text{in}\rangle_Y, |\text{out}\rangle_Y$ . In our analytical calculation, we assume the input and output fields of each cavity are normalized, because we ignore transmissivity of the ETM, and the diffraction loss, so that we have

$$\langle \text{in} | \text{in} \rangle_X = \langle \text{in} | \text{in} \rangle_Y = \langle \text{out} | \text{out} \rangle_X = \langle \text{out} | \text{out} \rangle_Y = 1. \quad (3.21)$$

We can then write

$$P_X = \langle \text{in} | \text{in} \rangle_X = 1, P_Y = \langle \text{in} | \text{in} \rangle_Y = 1 \quad (3.22)$$

and the power at the anti-symmetric port can be written as

$$\begin{aligned} P_{AS} &= \| |\text{out}\rangle_X - |\text{out}\rangle_Y \|^2 \\ &= 2 - \langle \text{out} | \text{out} \rangle_{XY} - \langle \text{out} | \text{out} \rangle_{YX}. \end{aligned} \quad (3.23)$$

With the definition of contrast defect in Eq. (3.15), we have

$$\epsilon_X = 1 - |\langle \text{in} | \text{out} \rangle_X|, \epsilon_Y = 1 - |\langle \text{in} | \text{out} \rangle_Y| \quad (3.24)$$

so that we can write the output field as

$$\begin{aligned} |\text{out}\rangle_X &= (1 - \epsilon_X) e^{i\phi_X} |\text{in}\rangle_X + |\delta_X\rangle \\ |\text{out}\rangle_Y &= (1 - \epsilon_Y) e^{i\phi_Y} |\text{in}\rangle_Y + |\delta_Y\rangle \end{aligned} \quad (3.25)$$

where

$$\begin{aligned}
\langle \delta_X | \text{in} \rangle_X &= 0, \langle \delta_X | \delta_X \rangle = \epsilon_X \\
\langle \delta_Y | \text{in} \rangle_Y &= 0, \langle \delta_Y | \delta_Y \rangle = \epsilon_Y \\
\langle \delta_X | \text{in} \rangle_Y &= \langle \delta_Y | \text{in} \rangle_X = 0.
\end{aligned} \tag{3.26}$$

In both the analytical and numerical calculations, we assume one of the two interferometer cavities is perfect and the other is with mirror figure errors, so here we can write  $\epsilon_Y = 1, |\delta_Y\rangle = 0$ , therefore, to the first order approximation ( $\epsilon_X \ll 1$ ), we obtain

$$P_{AS} = 2\epsilon_X \tag{3.27}$$

which shows that the contrast defect defined in Eq. (3.14) is the same as the analytical definition in Eq. (3.15).

When we consider two cavities both with imperfections, if they are statistically independent, we can write  $\langle \delta_X | \delta_Y \rangle = 0$ , so that the average value of the contrast defect of the system is

$$P_{AS} = 2(\epsilon_X + \epsilon_Y). \tag{3.28}$$

We now show that Eq. (3.15) can be approximately written as given in Eq. (3.16). From Eq. (3.13), we have

$$\langle \text{in} | \text{out} \rangle = \sum_{n'} \frac{\gamma + i(\omega - \omega_{n'})}{\gamma - i(\omega - \omega_{n'})} \langle \text{in} | n' \rangle \langle n' | \text{in} \rangle \tag{3.29}$$

when  $\omega - \omega_{n'} \ll \gamma$ , Eq. (3.29) can be expanded as

$$\sum_{n'} \left[ 1 + \frac{2i(\omega - \omega_{n'})}{\gamma} - \frac{2(\omega - \omega_{n'})^2}{\gamma^2} \right] \langle \text{in} | n' \rangle \langle n' | \text{in} \rangle. \tag{3.30}$$

Note that when the mode frequency is shifted  $\omega_{n'}$ , the optical power in the cavity is maximized, so that the linear term vanishes, therefore that the modulated frequency of the beam  $\omega$  can be given by:

$$\omega = \frac{kc}{L} \langle 33 | \delta h | 33 \rangle. \tag{3.31}$$

The contrast defect defined in Eq. (3.15) is

$$\begin{aligned}
\epsilon &= \sum_{n'} \frac{2(\omega - \omega_{n'})^2}{\gamma^2} \langle \text{in} | n' \rangle \langle n' | \text{in} \rangle \\
&= \frac{2}{\gamma^2} \left( \sum_{n'} \langle \text{in} | n' \rangle \omega_{n'}^2 \langle n' | \text{in} \rangle - \omega^2 \right).
\end{aligned} \tag{3.32}$$

After perturbation, the frequency split is the eigenvalue of the matrix given in Eq. (3.9) and the eigenvector of the matrix is the real eigenmode of the cavity, thus we can write

$$\begin{aligned}
& \sum_{n'} \langle \text{in} | n' \rangle \omega_{n'}^2 \langle n' | \text{in} \rangle \\
&= \left( \frac{2\pi c}{\lambda L} \right)^2 \sum_{n' m' l'} \langle \text{in} | n' \rangle \langle n' | \delta h | m' \rangle \langle m' | \delta h | l' \rangle \langle l' | \text{in} \rangle \\
&= \left( \frac{2\pi c}{\lambda L} \right)^2 \sum_{m'} \langle \text{in} | \delta h | m' \rangle \langle m' | \delta h | \text{in} \rangle
\end{aligned} \tag{3.33}$$

where  $\gamma = cT/4L$ . Then, in this limit, when the injected field is  $|33\rangle$ , the contrast defect can be written as in Eq. (3.16).

## Bibliography

- [1] LIGO Scientific Collaboration, “LIGO: The Laser Interferometer Gravitational-wave Observatory”, Reports on Progress in Physics (2009).
- [2] <http://www.virgo.infn.it/>.
- [3] <http://www.geo600.de/>.
- [4] <http://tamago.mtk.nao.ac.jp/>.
- [5] G. Harry, H. Armandula, E. Black, D. Crooks, G. Cagnoli, J. Hough, P. Murray, S. Reid, S. Rowan, P. Sneddon, M. Fejer, R. Route, and S. Penn, *Appl. Opt.* **45**, 1569-1574 (2006).
- [6] R. F. Greene and H. B. Callen, *Phys. Rev. D*, **88**, 6 (1952).
- [7] Y. Levin, *Phys. Rev. D*, **57**, 659(1998).
- [8] G. Lovelace, *Class. Quant. Gravity* **24**, 4491 (2007).
- [9] E. D’Ambrosio, R. OShaughnessy, K. Thorne, S. Strigin, and S. Vyatchanin, *Class. Quant. Gravity* **21**, S867 (2004).
- [10] B. Mours, E. Tournefier, and J.-Y. Vinet, *Class. Quant. Gravity* **23**, 5777 (2006).
- [11] M. Bondarescu and K. S. Thorne, *Phys. Rev. D*, **74**, 082003 (2006).
- [12] J. Miller, PhD. Thesis, U. of Glasgow (2010).
- [13] M. Bondarescu, O. Kogan, and Y. Chen, *Phys. Rev. D* **78**, 082002 (2008).
- [14] M. Granata and C. Buy and R. Ward and M. Barsuglia, *Phys. Rev. Lett.* **105**, 231102(2010).
- [15] P. Fulda, K. Kokeyama, S. Chelkowski, and A. Freise, *Phys. Rev. D*, **82**, 012002 (2010).
- [16] This algorithm is based on techniques developed by F. Bondu (Observatoire de la Côte d’Azur/ Institut de Physique de Rennes).
- [17] A. E. Siegman, *Lasers*, University Science Books (1986).
- [18] S. Chelkowski, S. Hild and A. Freise, *Phys. Rev. D* **79**, 122002 (2009)
- [19] G. J. Milburn, *Quantum Optics*, Springer-Verlag (1994)
- [20] P. Fritschel, R. Bork, G. Gonzalez, N. Mavalvala, D. Ouimette, H. Rong, D. Sigg, and M. E. Zucker, *Appl. Optics* **40**, 4988(2001).

- [21] N. Smith-Lefebvre, S. Ballmer, M. Evans, S. Waldman, K. Kawabe, V. Frolov, N. Mavalvala, LIGO Document, P1100025-v8 (2011)
- [22] Polish and Metrology from Tinsley Optics <http://www.asphere.com>, LIGO Technical Document G1100216 (2011)
- [23] H. Yamamoto, “SIS (Stationary Interferometer Simulation) manual”, LIGO Technical Document, T070039-v3 (2010).
- [24] R. W. P. Drever et al., App. Phys. B **31**, 97-105 (1983).
- [25] S. W. Ballmer, Ph.D. thesis, MIT(2006).
- [26] H. Yamamoto, LIGO Technical note T1100220-v1 (2011).
- [27] B. Bochner, General Rel. and Grav. **35** (2003)

## Chapter 4

# Open Quantum Dynamics of Single-photon Optomechanical Devices

We study the quantum dynamics of a Michelson interferometer with Fabry-Perot cavity arms and one movable end mirror, and driven by a single photon—an optomechanical device previously studied by Marshall et al. as a device that searches for gravity decoherence. We obtain an exact analytical solution for the system’s quantum mechanical equations of motion, including details about the exchange of the single photon between the cavity mode and the external continuum. The resulting time evolution of the interferometer’s fringe visibility displays interesting new features when the incoming photon’s frequency uncertainty is narrower or comparable to the cavity’s line width—only in the limiting case of much broader-band photon does the result return to that of Marshall et al., but in this case the photon is not very likely to enter the cavity and interact with the mirror, making the experiment less efficient and more susceptible to imperfections. In addition, we show that in the strong-coupling regime, by engineering the incoming photon’s wave function, it is possible to prepare the movable mirror into an arbitrary quantum state of a multidimensional Hilbert space.

---

Originally published as T. Hong, H. Yang, H. Miao, and Y. Chen, submitted to Physics Review A, preprint available at arXiv: quant-ph/1110.3348.

## 4.1 Introduction

Recently, significant progress has been made in observing quantum effects in macroscopic mechanical systems [1]. As presented in the work of O’Connell et al. [2], a 6-GHz nanomechanical oscillator was cooled down near its quantum ground state with dilution refrigeration, and later prepared into a Fock state by coupling the oscillator to a superconducting qubit. States with thermal occupation numbers below unity have also been achieved with cavity-assisted radiation-pressure cooling, by Teufel et al. [3] and Safavi-Naeini et al. [4]. Further more, as shown by Gupta et al. [5] and Thompson et al. [6], it is possible to couple a single photon strongly with a mechanical degree of freedom, such that the momentum imparted by a single photon to a mechanical degree of freedom can be comparable to its initial momentum uncertainty.

In this paper, we study the open quantum dynamics of a nonlinear optomechanical device, namely a Michelson interferometer with Fabry-Perot cavities, one of them with a movable end mirror (acting as the mechanical oscillator). This device, driven by a single photon, was proposed by Marshall et al. [7, 8] as an experiment to search for Penrose’s conjecture of gravity decoherence [9]. Such single-photon driven devices have also been more recently studied by Rabl [10] and Nunnenkamp et al. [11]. By taking advantage of the conserved quantity—the total number of photons in the system, one can obtain exact solutions to this system’s quantum dynamics. Unlike Rabl and Nunnenkamp et al., who studied systematically the statistics of the out-going photons and the steady state reached by the mechanical oscillator, we focus instead on the fringe visibility of a single-photon interferometer, and the conditional quantum state of the mechanical oscillator upon the detection of an out-going photon.

The single-photon Michelson interferometer is shown schematically in Fig. 4.1, in which the port on the left is the input port, towards which the single photon is injected; the photon, after interacting with the Michelson interferometer, may exit either from the input port, or from the other open port. Each of the two arms consists of a high-finesse optical cavity; the setup of these two cavities are identical, except one of them has a movable end mirror, which acts as the mechanical oscillator that interacts with light in the cavity. The 50/50 beam splitter splits the quantum state of the entire mirror-light system into two components, one of them corresponding to the photon entering the fixed cavity (and leaving the oscillator at its initial state), the other corresponding to the photon entering the movable cavity (thereby modifying the oscillator’s state through radiation pressure). We will set the displacement zero-point of the interferometer to have equal arm lengths, with each arm at a distance equal to the beamsplitter. At such a zero point, the photon injected from the input port will return to the input port with unit probability. Therefore we also call the input port the “bright port” and the other open port the “dark port”. We can artificially tune the interferometer away from its zero point, e.g., by adjusting the fixed microscopic distances between the front mirrors and

the beamsplitter. This changes the relative phase  $\varphi$  between the two superimposed components in wave function of the entire system; the resulting variations in the probability density of having the photon exiting the bright port at time  $t$ , quantified by the fringe visibility, is a measure of the degree of coherence between these two components at this moment in time.

In the case of low environmental temperature and in the absence of unexpected mechanisms of decoherence, Marshall et al. showed that the visibility will revive completely for every half of the mechanical oscillation period. In obtaining such a result, they assumed the photon was initially already in either of the two cavity arms, and considered a closed evolution of the cavity mode and the mechanical oscillator. This assumption has also been widely used in analysis of such a nonlinear optomechanical device, e.g., by Bose et al. [12] and subsequent analysis of the Marshall experiment [7] by Bassi et al. [13].

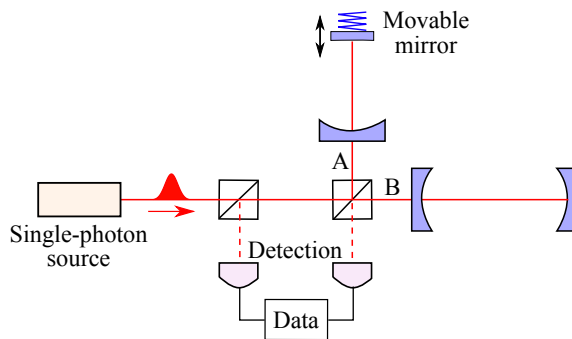


Figure 4.1: (color online) A schematic showing the single-photon interferometer. The external single photon excites the cavity mode which in turn interacts with the movable end mirror via radiation pressure. This is adapted from Fig. 1 of Ref. [7] with small modifications.

In a realistic experimental setup, it is necessary to take full account of the *open quantum dynamics* of this system, which that involves the oscillator (the mirror), the cavity mode and the external continuous field, including how the single photon is coupled into the cavity in the first place. The open quantum dynamics depends on the wave function of the photon, whose Fourier transform is related to the frequency content of the photon. For example, if the photon has a short-pulse wave function with time-domain duration much less than the cavity storage time, which corresponds to a frequency uncertainty much larger than the cavity line width, then the photon will only enter the cavity with a small probability. By contrast, a narrowband photon (with frequency uncertainty below cavity line width) must have a wave packet duration much longer than cavity storage time, and therefore we must address the issue that the photon can be simultaneously inside and outside the cavity. The latter scenario, although more complicated, might be experimentally more favorable, as in this scenario the photon has a high probability to enter the cavity and to interact with the mirror much more strongly.

The outline of this article goes as follows: in Sec. 4.2, we will write down the Hamiltonian of our

nonlinear optomechanical device and study the open quantum dynamics by solving the Schrödinger equation exactly; in Sec. 4.3, we will give a detailed analysis of the single-photon interferometer, and will calculate the interferometer's fringe visibility; in Sec. 4.4, we will show that the mechanical oscillator can be prepared to an arbitrary quantum state in a multidimensional Hilbert space, if we inject the single photon with a properly designed profile into the interferometer; in Sec. 4.6, we will summarize our main results.

## 4.2 A Single Cavity with one Movable Mirror

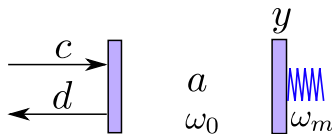


Figure 4.2: (color online) A schematics showing a single-photon interferometer with Fabry-Perot cavity and a movable mirror. The displacement of the mirror-endowed mechanical oscillator  $y$  is parametrically coupled to the cavity mode  $a$ , which has an eigenfrequency  $\omega_0$  with  $y = 0$ . The cavity mode in turn couples to the ingoing continuous field  $c(x)$  and outgoing continuous field  $d(x)$ .

Before studying the entire single-photon interferometer, we first consider a single cavity, as shown schematically in Fig. 4.2. The cavity has one fixed mirror located at  $x = 0$ , and one movable mirror which acts as a mechanical oscillator. Here, assuming the injected photon to have a frequency content much less than the free spectral range of the cavity (which has a relatively high finesse), we will only consider one optical mode of the cavity (which we shall refer to as *the cavity mode*). By assuming a high finesse for the cavity, this mode couples to the external vacuum via single-photon exchange. At linear order in the mirror's motion and assuming low velocity, the coupling between the mirror and the cavity mode is parametric: the position  $y$  of the mirror modifies the eigenfrequency of the cavity mode.

### 4.2.1 The Hamiltonian

Here we will write down the Hamiltonian of the system. For simplicity, we will use natural units with  $\hbar = 1$  and  $c = 1$  throughout this paper. The Hamiltonian of the external continuous optical field, in the position space representation, is given by

$$\begin{aligned} \hat{H}_o &= \frac{i}{2} \int_{-\infty}^0 [(\partial_x \hat{c}_x^\dagger) \hat{c}_x - \hat{c}_x^\dagger \partial_x \hat{c}_x] dx \\ &+ \frac{i}{2} \int_{-\infty}^0 [(\partial_x \hat{d}_x^\dagger) \hat{d}_x - \hat{d}_x^\dagger \partial_x \hat{d}_x] dx \end{aligned} \quad (4.1)$$

where  $\hat{c}_x$  and  $\hat{d}_x$  are the annihilation operators for ingoing and outgoing field at location  $x$ , respectively. Note that for the actual setup shown in Fig. 4.2, the ingoing and outgoing field are on the same side of the front mirror, namely both at  $x < 0$ . Since the field operators at different locations commute with each other— $[\hat{c}_x, \hat{c}_{x'}^\dagger] = \delta(x - x')$ , we can fold the outgoing field from  $[-\infty, 0]$  into  $[0, +\infty]$ , therefore just use  $\hat{c}$  to denote both the ingoing and outgoing fields, with  $\hat{c}_x(x < 0)$  for the ingoing field and  $\hat{c}_x(x > 0)$  for the outgoing field, namely:

$$\hat{H}_o = \frac{i}{2} \int_{-\infty}^{\infty} (\partial_x \hat{c}_x^\dagger \hat{c}_x - \hat{c}_x^\dagger \partial_x \hat{c}_x) dx. \quad (4.2)$$

The free Hamiltonian of the single cavity mode is given by

$$\hat{H}_c = \omega_0 \hat{a}^\dagger \hat{a} \quad (4.3)$$

with  $\hat{a}$  the annihilation operator and  $[\hat{a}, \hat{a}^\dagger] = 1$ .

The free Hamiltonian for the mechanical oscillator reads

$$\hat{H}_m = \frac{\hat{p}_y^2}{2m} + \frac{1}{2} m \omega_m^2 \hat{y}^2, \quad (4.4)$$

where  $\hat{y}$  and  $\hat{p}_y$  are the position and momentum operators, respectively.

The total interaction Hamiltonian  $H_I$  between the external continuum and the cavity mode in the rotating-wave approximation, and between the cavity mode and the mechanical oscillator, is given by

$$\hat{H}_I = i\sqrt{\gamma}(\hat{c}_0 \hat{a}^\dagger - \hat{a} \hat{c}_0^\dagger) + k \hat{a}^\dagger \hat{a} \hat{y}. \quad (4.5)$$

Here  $\gamma = \frac{T}{2L}$  is the cavity bandwidth with  $L$  being the cavity length;  $k = \omega_0/L$  is the optomechanical coupling constant. The interaction between the cavity mode and the external continuum takes place at the front mirror with  $x = 0$  and the Hamiltonian describes the exchange of photon between them. The total Hamiltonian is a sum of the free and the interaction parts, namely,

$$\hat{H} = \hat{H}_o + \hat{H}_c + \hat{H}_m + \hat{H}_I. \quad (4.6)$$

Note once more that by including only a single cavity mode resonant at frequency  $\omega_0/(2\pi)$ , we must make sure the frequency content of the injected light is focused well within a free spectral range,  $c/(2L)$ .

### 4.2.2 Structure of the Hilbert Space

Even though the Hamiltonian contains a cubic term  $\hat{a}^\dagger \hat{a} \hat{y}$ , which implies a nonlinear dynamics, we have a conserved dynamical quantity—the total photon number:

$$\hat{a}^\dagger \hat{a} + \int_{-\infty}^{+\infty} \hat{c}_x^\dagger \hat{c}_x dx, \quad (4.7)$$

which makes the system’s evolution still analytically solvable, as also recognized by Rabl [10] and Nunnenkamp et al. [11]. Since the initial state of our system consists of one single photon, there can only be one photon throughout the entire evolution. Mathematically, this means we only need to consider a one-photon subspace of the entire Hilbert space, which in turn consists of three disjoint subspaces, which corresponds to:  $\mathcal{H}_{1-}$ , which corresponds to an incoming photon towards the cavity;  $\mathcal{H}_2$ , which corresponds to a photon inside the cavity, and  $\mathcal{H}_{1+}$ , which corresponds to a photon leaving the cavity. All quantum states in this space can be written as:

$$\begin{aligned} |\psi\rangle &= \int_{-\infty}^{+\infty} f(x, t) e^{-i\omega_0(t-x)} |x\rangle_\gamma \otimes |\phi_1(x, t)\rangle_m dx \\ &+ \alpha(t) e^{-i\omega_0 t} \hat{a}^\dagger |0\rangle_\gamma \otimes |\phi_2(t)\rangle_m. \end{aligned} \quad (4.8)$$

Here

$$|x\rangle_\gamma \equiv \hat{c}_x^\dagger |0\rangle_\gamma \quad (4.9)$$

is the “position eigenstate” of the single photon outside of the cavity, and  $|0\rangle_\gamma$  is the optical vacuum; the subscripts  $\gamma$  and  $m$  indicate Hilbert spaces of light and movable mirror, respectively;  $f(x, t)$  is a complex function of position ( $-\infty < x < +\infty$ ) and time,  $\alpha(t)$  is a complex function of time  $t$  alone;  $|\phi_1(x, t)\rangle_m$  and  $|\phi_2(t)\rangle_m$  are two *families of* state vectors that belong to the Hilbert space of the mechanical oscillator. At any given time, the  $x < 0$  part of the integral term on the right-hand side corresponds to  $\mathcal{H}_{1-}$ , the  $x > 0$  part of the integral term corresponds to  $\mathcal{H}_{1+}$ , while the non-integral term corresponds to  $\mathcal{H}_2$ . In general, all three terms will be present, which means the entire system’s quantum state is a superposition of having the photon simultaneously present in all three possible locations. Note that the factors  $e^{-i\omega_0(t-x)}$  and  $e^{-i\omega_0 t}$  are added to “factor out” the free oscillation of the EM field, which has oscillation frequencies near  $\omega_0$ .

By imposing normalization conditions of

$${}_m \langle \phi_1(x, t) | \phi_1(x, t) \rangle_m = {}_m \langle \phi_2(t) | \phi_2(t) \rangle_m = 1, \quad (4.10)$$

the probability for finding the photon at location  $x$  (with  $x < 0$  indicating a photon propagating

towards the cavity, and  $x > 0$  a photon propagating away from the cavity) is given by

$$p_\gamma(x, t) = |f(x, t)|^2 \quad (4.11)$$

while the probability that the photon is in the cavity is given by  $|\alpha^2(t)|$ . In this way, the normalization condition of the joint quantum state

$$\int_{-\infty}^{+\infty} |f(x, t)|^2 dx + |\alpha^2(t)| = 1 \quad (4.12)$$

is simply a statement about the conservation of total probability.

The function  $f(x, t)$  can be viewed as the out-of-cavity photon's wave function, while  $|\phi_1(x, t)\rangle_m$  for each  $x$  can be viewed as the oscillator state that is entangled with *each possibility* for the out-of-cavity photon. On the other hand,  $\alpha(t)$  can be viewed as the probability amplitude of the cavity mode, while  $|\phi_2(t)\rangle_m$  can be viewed as the oscillator state that is entangled with the in-cavity photon.

To facilitate calculation, for any joint quantum state  $|\psi\rangle$ , we define

$$|\psi_1(x, t)\rangle_m \equiv {}_\gamma\langle x|\psi\rangle e^{i\omega_0(t-x)} = f(x, t)|\phi_1(x, t)\rangle_m \quad (4.13)$$

$$|\psi_2(t)\rangle_m \equiv \langle 0|a|\psi\rangle e^{i\omega_0 t} = \alpha(t)|\phi_2(t)\rangle_m. \quad (4.14)$$

Here  $|\psi_1(x, t)\rangle_m$ ,  $-\infty < x < +\infty$ , is a series of vectors, parametrized by  $x$ , in the Hilbert space of the mechanical oscillator, while  $|\psi_2(x, t)\rangle$  is a single vector in the Hilbert space of the mechanical oscillator. They together carry the full information of the quantum state of the entire system. To further appreciate the role of  $|\psi_1\rangle_m$  and  $|\psi_2\rangle_m$ , we can project each of them into the position eigenstate of the oscillator,  $|y\rangle_m$ , obtaining

$$\Phi_1(t, x, y) \equiv {}_m\langle y|\psi_1\rangle_m = f(x, t)\phi_1(y, x, t) \quad (4.15)$$

$$\Phi_2(t, y) \equiv {}_m\langle y|\psi_2\rangle_m = \alpha(t)\phi_2(y, t) \quad (4.16)$$

which can be viewed as the *joint wave functions* of the projection of the entire state into  $\mathcal{H}_{1+} \oplus \mathcal{H}_{1-}$  and  $\mathcal{H}_2$ , respectively. Note that although  $f(x, t)$  and  $|\phi_1(x, t)\rangle_m$  [and similarly  $\alpha(t)$  and  $|\phi_2(t)\rangle_m$ ] share a phase ambiguity,  $|\psi_1(x, t)\rangle_m$  and  $|\psi_2(t)\rangle_m$ , and hence  $\Phi_1(t, x, y)$  and  $\Phi_2(t, y)$  are well defined without ambiguity.

### 4.2.3 Initial, Final States and Photodetection

As special cases, we consider the quantum state of the system at  $t = 0$  (the initial state), and at very late times (the final state). For the initial state, the photon is propagating towards the cavity, and the cavity is empty. This corresponds to  $\alpha(0) = 0$ , and  $f(x, 0) = 0$ . In particular, we also presume

the initial state to be *separable* between the photon and the oscillator, with

$$|\psi(0)\rangle = \int e^{i\omega_0 x} F(x) |x\rangle_\gamma dx \otimes |\phi_0\rangle_m. \quad (4.17)$$

Here  $F(x)$  is the slowly-varying part of the initial wave function of the photon, and  $|\phi_0\rangle_m$  the initial wave function of the oscillator. In other words, we have

$$|\psi_1(t=0)\rangle_m = F(x) |\phi_0\rangle_m \quad (4.18)$$

$$|\psi_2(t=0)\rangle_m = 0 \quad (4.19)$$

with  $F(x) = 0$  for  $x > 0$ . At a sufficiently late time  $T$ , the photon will leave the cavity with unity probability, and we expect  $\alpha(T) = 0$  and  $f(x, T) = 0$  for  $x < 0$ . Mathematically,

$$\begin{aligned} |\psi_1(x, t \geq T)\rangle_m &= F_{\text{out}}(x, t) |\phi(x, t)\rangle_m \\ |\psi_2(t \geq T)\rangle_m &= 0 \end{aligned} \quad (4.20)$$

with  $F_{\text{out}}(t, x) = 0$  for  $x < 0$  and  $t > T$ . This is an explicitly entangled state between the out-going photon and the mirror, if  $|\phi(x, t)\rangle_m$  for different values of  $x$  are not all proportional to the same state vector.

At an intermediate time  $t > 0$ , suppose a photodetector is placed at  $x = L > 0$  (i.e., for out-going photons from the cavity), then the probability density for photon arrival time at  $T$  is given by

$$p_L(T) = {}_m\langle \psi_1(L, T) | \psi_1(L, T) \rangle_m. \quad (4.21)$$

In addition, by detecting a photon at this particular instant, the oscillator is left at a *condition quantum state* of  $|\phi(x, T)\rangle_m$

#### 4.2.4 Evolution of the Photon-mirror Quantum State

Applying the operations  ${}_\gamma\langle x|$  and  ${}_\gamma\langle 0|a$  onto the (joint) Schrödinger equation

$$i\hbar \frac{d|\psi\rangle}{dt} = \hat{H}|\psi\rangle \quad (4.22)$$

we will obtain coupled equations for  $|\psi_1\rangle_m$  and  $|\psi_2\rangle_m$ . Throughout this section, we will mostly encounter states in the oscillator's Hilbert space, therefore we will ignore the subscript "m" unless otherwise necessary.

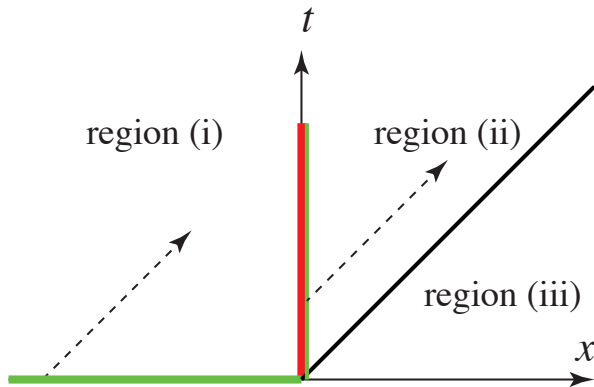


Figure 4.3: (color online) Three regions of the  $t$ - $x$  plane and the free evolutions of  $|\psi_1\rangle$ . In region (i), the photon has not yet entered the cavity; the joint quantum state of the system is a simple free evolution of the initial quantum state, specified on  $t = 0$ ,  $x < 0$  (green horizontal half line), see Eq. (4.25). In region (ii), the photon and the oscillator evolve freely after propagates after the photon emerges from the cavity; the joint wave function depends on the wave function along  $x = 0$ ,  $t > 0$  (green vertical half line). The red line dividing regions (i) and (ii) corresponds to the  $\delta$ -function in Eq. (4.23), which embodies the interaction between the outside photon and the in-cavity photon. Region (iii) is causally irrelevant to our experiment.

#### 4.2.4.1 Free Evolution

For  $|\psi_1\rangle$ , by applying  $\gamma\langle x|$  to both sides of Eq. (4.22) we obtain

$$\left[ \partial_t + \partial_x + i \hat{H}_m \right] |\psi_1(x, t)\rangle = -\sqrt{\gamma} \delta(x) |\psi_2(t)\rangle. \quad (4.23)$$

Equation (4.23), without the  $\delta$ -function term, simply describes the propagation of the initial photon towards the cavity, and the free evolution of the oscillator. This is because when the single photon is outside the cavity, its propagation is free, while the oscillator's evolution is unaffected by light.

Equation (4.23), is a first-order partial differential equation with characteristics along  $x - t = \text{const}$ . We hereby divide the  $t > 0$  region of the  $t$ - $x$  plane into three regions: (i)  $x < 0$ , (ii)  $x > 0$  and  $t > x$ , and (iii)  $x > 0$  and  $t < x$ , as shown in Fig. 4.3. We can discard region (iii) right away, because it is not causally connected with our experiment. In the interiors of regions (i) and (ii) separately, Eq. (4.23) has the following general solution,

$$|\psi_1(x, t)\rangle = e^{-\frac{i}{2} \hat{H}_m(t+x)} |C(t-x)\rangle \quad (4.24)$$

with  $|C(v)\rangle$  an arbitrary state-valued function of  $v$ .

In region (i),  $|C(v)\rangle$  can be specified by initial data along the half line of  $t = 0$ ,  $x < 0$ ; by using Eq. (4.24) twice, at  $(t, x)$  and  $(0, x - t)$ , we obtain [See Fig. 4.3]:

$$|\psi_1(x < 0, t)\rangle = F(x - t) \hat{U}_m(t) |\phi_0\rangle. \quad (4.25)$$

Here  $U_m$  is the evolution operator for the free oscillator, given by

$$\hat{U}_m(t) = e^{-i\hat{H}_m t}. \quad (4.26)$$

In terms of the Fock states  $|n\rangle$ , we have

$$\hat{U}_m(t) = \sum_n |n\rangle e^{-i(n+\frac{1}{2})\omega_m t} \langle n|. \quad (4.27)$$

Equation (4.25) corresponds to the photon's wave packet freely propagating along the positive direction of the  $x$  axis and the mechanical oscillator independently evolving under its own Hamiltonian.

In region (ii),  $|C(v)\rangle$  is specified by boundary data along the half line of  $x = 0+$ ,  $t > 0$ , which we denote by

$$|\psi_1(t)\rangle_{0+} \equiv |\psi_1(0+, t)\rangle. \quad (4.28)$$

By using Eq. (4.24) twice, at  $(t, x)$  and  $(t - x, 0)$ , we obtain

$$|\psi_1(x > 0, t)\rangle = \hat{U}_m(x) |\psi_1(t - x)\rangle_{0+}. \quad (4.29)$$

Henceforth in the paper,  $0+$  and  $0-$  stand for  $x \mapsto 0+$  ( $x$  approaches 0 from positive side of the axis) and  $x \mapsto 0-$  ( $x$  approaches 0 from negative side of the axis), respectively. Equation (4.29) corresponds to the free evolution of the out-going photon and the mechanical oscillator.

#### 4.2.4.2 Junction Condition

The  $\delta$ -function on the right-hand side of Eq. (4.23) relates the out-going photon to the decay of the in-cavity photon and the reflection of the in-going photon. To take this into account, we simply integrate both sides from  $x = 0-$  to  $x = 0+$ , obtaining:

$$|\psi_1(0+, t)\rangle = |\psi_1(0-, t)\rangle - \sqrt{\gamma} |\psi_2(t)\rangle. \quad (4.30)$$

This expresses the outgoing wave as a combination of the promptly reflected incoming wave and the wave coming out from the cavity.

#### 4.2.4.3 Coupled Evolution

By applying  ${}_\gamma\langle 0|a$  to both sides of Eq. (4.22) and using Eq. (4.30), we obtain:

$$\left[ \partial_t + \frac{\gamma}{2} + i\hat{H}_\gamma \right] |\psi_2(t)\rangle = \sqrt{\gamma} |\psi_1(t)\rangle_{0-}. \quad (4.31)$$

Here as in Eq. (4.30), we have defined  $|\psi_1\rangle_{0\pm} \equiv |\psi_1(0\pm, t)\rangle$ . We have also defined

$$\hat{H}_\gamma \equiv \frac{\hat{p}_y^2}{2m} + \frac{m\omega_m^2(\hat{y} - \alpha)^2}{2} - \beta^2\omega_m \quad (4.32)$$

with

$$\alpha = -\frac{k}{m\omega_m^2}, \quad \beta = \frac{k}{\omega_m\sqrt{2m\omega_m}}. \quad (4.33)$$

The operator  $\hat{H}_\gamma$  can be viewed as the modified Hamiltonian for the mirror when the photon is present in the cavity. Here  $\alpha$  characterizes the shift in equilibrium position of the harmonic oscillator when the photon is inside the cavity and applies a constant force to the oscillator, while  $\beta$  (as seen from this equation) modifies the eigenfrequency of the harmonic oscillator. It is easy to work out the eigenstates and eigenvalues of  $\hat{H}_\gamma$ : the eigenstates are

$$|\tilde{n}\rangle = e^{i\alpha\hat{p}_y}|n\rangle = \hat{D}(\beta)|n\rangle \quad (4.34)$$

which are simply displaced from the original Fock states in phase space, due to the change of equilibrium position, with

$$\hat{H}_\gamma|\tilde{n}\rangle = \left(n + \frac{1}{2} - \beta^2\right)\omega_m|\tilde{n}\rangle \quad (4.35)$$

which indicates an overall down-shift of eigenfrequency. Here we have further defined the displacement operator

$$\hat{D}(\beta) \equiv \exp[\beta(b^\dagger - b)] \quad (4.36)$$

with  $b$  and  $b^\dagger$  the annihilation and creation operators for the free mechanical oscillator (i.e., before it couples to light). As we shall see in Sec. 4.6,  $\beta$  will become an important characterizing parameter of our optomechanical device; for example,  $\beta \gtrsim 1$  is the regime in which the device is nonlinear.

For the photon, Eq. (4.31) means that the in-cavity photon is continuously driven by the incoming photon (right-hand side) and decays towards the outgoing photon (as indicated by the  $\gamma/2$  term in the bracket on the left-hand side). The above discussion, together with the initial data of  $|\psi_2\rangle = 0$  at  $t = 0$  gives

$$|\psi_2\rangle = \sqrt{\gamma} \int_0^t e^{-\frac{\gamma}{2}(t-t')} \hat{U}_\gamma(t-t') |\psi_1(t')\rangle_{0-} \quad (4.37)$$

where

$$\hat{U}_\gamma(t) \equiv e^{-i\hat{H}_\gamma t} = \sum_n |\tilde{n}\rangle e^{-i(n+1/2-\beta^2)\omega_m t} \langle \tilde{n}|, \quad (4.38)$$

which is the modified evolution operator of the oscillator when the photon is in the cavity.

#### 4.2.4.4 Full Evolution

The full evolution of the entire system's quantum state can now be obtained by combining Eqs. (4.29), (4.25), (4.30), and (4.37). In order to study the outgoing photon, we only need to consider the region  $x > 0$  and  $t > x$  (see Fig. 4.3), because the photon emerges from the cavity at  $t > 0$ , and it propagates with  $c = 1$ . For this region, we obtain a compact-form solution of

$$|\psi_1(x, t)\rangle = \hat{M}|\phi_0\rangle \quad (4.39)$$

where  $|\phi_0\rangle$  is the initial quantum state of the oscillator, and

$$\begin{aligned} \hat{M} &= \int_0^{t-x} g(t-x, t') \hat{U}_m(x) \hat{U}_\gamma(t-x-t') \hat{U}_m(t') dt' \\ &= \int_0^{t-x} g(t-x, t') e^{i\beta^2 \omega_m(t-x-t')} \\ &\quad \hat{D}(\beta e^{-i\omega_m x}) \hat{D}(-\beta e^{i\omega_m(t'-t)}) \hat{U}_m(t) dt' \end{aligned} \quad (4.40)$$

where

$$g(t, t') \equiv G(t-t') F(-t') \quad (4.41)$$

with

$$G(t) = \delta_+(t) + \gamma e^{-\frac{\gamma}{2}t} \quad (4.42)$$

the cavity's optical Green function. Here the subscript  $+$  for the  $\delta$  function indicates that its support lies completely in the region  $t > 0$ . Within the operator  $\hat{M}$  [Eq. (4.40)], the factor  $g$  contains two terms, the first contains a  $\delta$ -function and the second an exponential decay over time. The first term corresponds to the photon being promptly reflected by the cavity's front mirror, while the second term corresponds to the photon staying inside the cavity, for an amount of time equal to  $t-x-t'$ , which ranges from 0 to  $t-x$ . As a sanity check, it is straightforward to see that when mass of the oscillator approaches infinity,  $\hat{U}_\gamma$  coincides with  $\hat{U}_m$ , and  $\hat{M}$  simply describes the photon's propagation and the independent evolution of the oscillator.

### 4.3 Single-photon Interferometer: Visibility

In this section, we will use the results of the previous section to analyze the single-photon interferometer.

### 4.3.1 The Configuration

We consider a scheme proposed and analyzed by Marshall et al. [7], which is shown in Fig. 4.1. This Michelson interferometer (with 50/50 beamsplitter) has two arms: in the north arm, the end mirror in cavity A is movable, and initially prepared at a quantum state  $|\phi_0\rangle$ , whereas mirrors in cavity B or east arm are fixed. We assume the photon is injected from the west port, while a fixed photodetector is placed at the south port. Apart from mirror A being movable, the two cavities are otherwise identical: with the same input-mirror power transmissivity  $T$ , length  $L$  (for cavity A, counted from the zero-point of A's displacement). The front mirrors are placed at equal macroscopic distance from the beamsplitter, while there is a phase detuning of  $\varphi$  in arm B for  $\omega_0$ <sup>1</sup>. In our convention, if mirror A is at zero point and  $\varphi = 0$ , the photon will always return to the west port. Henceforth in the paper, we shall refer to the west port as the input port, and the south port the output port—although we may not always find the photon at the output port. Indeed, whether and when the photon arrives at the photodetector is jointly determined by  $\varphi$  and the state of motion of mirror A.

In particular, we shall use  $p(t)$  to denote the probability density for the photon to arrive at the detector at  $t$  (which can be measured by repeating the experiment many times). If we idealize the arrival time of the in-going photon (at the front mirror) to be  $t = 0$ , and ignore the macroscopic distance between the front mirrors, the beamsplitter, and the photodetector, then we are interested in  $p(t)$  at  $t \geq 0$ . We further define an *instantaneous fringe visibility*

$$v(t) = \frac{p_{\max}(t) - p_{\min}(t)}{p_{\max}(t) + p_{\min}(t)}, \quad (4.43)$$

which measures the degree of coherence between the two components of returning photons at the beamsplitter, and can only become unity if at time  $t$  the joint mirror-photon quantum state is separable, as we shall see more clearly in Sec. 4.3.4.

### 4.3.2 The Role of the Beamsplitter and a Decomposition of Field Degrees of Freedom

In Sec. 4.2.3, we have studied in detail how the photon first affects the  $x < 0$  components of the optical field outside of a cavity, then interacts with the mirror, and finally returns back to the  $x > 0$  components of the optical field. The scenario for a Michelson interferometer is slightly more complicated: we now need to consider a set of *input fields* that replaces the  $x < 0$  single field in the single-cavity case, and a set of *output fields* which replaces the  $x > 0$  single field.

As shown in Fig. 4.4, the annihilation operators of the input field for the two cavities are  $(\hat{j}_-,$

---

<sup>1</sup>To give rise to a detuning, we assume that all optical frequencies we consider are centered around  $\omega_0$ , and we offset the location of cavity B from symmetry by a length  $l$  such that  $\omega_0 l = \varphi/2$ .

$\hat{k}_-, \hat{a}_-, \hat{b}_-$ ), while those of the output fields for the cavities are  $(\hat{j}_+, \hat{k}_+, \hat{a}_+, \hat{b}_+)$ . Each of these fields are defined as a function of  $-\infty < x < +\infty$ , with  $x = 0$  corresponding to the position of the beamsplitter, and positive direction along the arrow shown in Fig. 4.4. Ultimately, we need to calculate the fields of  $\hat{j}_+$  and  $\hat{k}_+$  in terms of  $\hat{j}_-$  and  $\hat{k}_-$ .

Note that at by allowing  $x$  to run through the entire real axis, we have assigned *two* input fields and two output fields to each point along the optical path (note here that “input” and “output” refer to the cavities, *not the beamsplitter*). This redundancy is necessary for a simplified treatment of the beamsplitter: instead of treating its internal dynamics, we simply view it as a mapping between the two different *representations* of the input and output fields. One representation  $(\hat{j}_\pm, \hat{k}_\pm)$  corresponds to the point of view of observers at the west and south ports, pretending that the beamsplitter does not exist; the other  $(\hat{a}_\pm, \hat{b}_\pm)$  corresponds to the point of view of observers at the east and north ports.

The conversion between the two representations takes the same form as the “input-output relation” of the beamsplitter:

$$\hat{b}_\pm(x) = \frac{\hat{j}_\pm(x) - \hat{k}_\pm(x)}{\sqrt{2}}, \quad \hat{a}_\pm(x) = \frac{\hat{j}_\pm(x) + \hat{k}_\pm(x)}{\sqrt{2}}. \quad (4.44)$$

As an example, consider a quantum state in which a (instantaneous) photon is injected from the input port, which, according to the mapping in Eq. (4.44), has two equivalent representations:

$$\hat{j}_-^\dagger(x_0)|0\rangle = \frac{\hat{a}_-^\dagger(x_0) + \hat{b}_-^\dagger(x_0)}{\sqrt{2}}|0\rangle. \quad (4.45)$$

As time grows, the quantum state evolves as  $x_0 \rightarrow x_0 + t$ . At any instant, the left-hand side represents a single photon propagating from west to east, and continue through the location of the beamsplitter. The right-hand side represents a photon that has a two-component wave function, the first component propagates northwards, the second eastwards.

Although the two representations are equivalent, we still prefer to use the south-west representation when treating the generation and detection of photons, and the north-east representation when treating the light’s interaction with the cavities.

### 4.3.3 Interactions Between Light and Cavities

For each individual cavity, we intend to apply the result of Sec. 4.2.1. We note that  $\hat{a}_-(x)$  (for  $x < 0$ ) and  $\hat{a}_+(x)$  (for  $x > 0$ ) defined in this section maps to the  $\hat{c}(x)$  (for  $x < 0$ ) and  $\hat{d}(x)$  (for

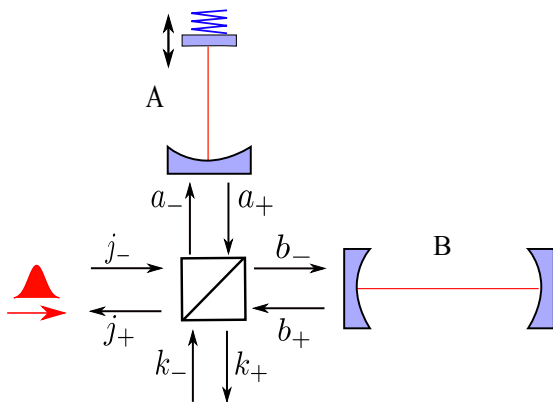


Figure 4.4: We illustrate the fields entering and exiting each of the four ports of the interferometer. We use arrows to define the positive sense of the coordinate used to label their locations. For each of them  $x = 0$  corresponds to the location of the beamsplitter.

$x > 0$ ), respectively, as defined in Sec. 4.2.1 and illustrated in Fig. 4.2. For this reason, we define

$$\hat{a}(x) \equiv \begin{cases} \hat{a}_-(x), & x < 0, \\ \hat{a}_+(x), & x > 0, \end{cases} \quad (4.46)$$

and

$$\hat{b}(x) \equiv \begin{cases} \hat{b}_-(x), & x < 0, \\ \hat{b}_+(x), & x > 0. \end{cases} \quad (4.47)$$

In this way,  $a(x)$  and  $b(x)$  here both map to  $c(x)$  defined in Sec. 4.2.1. [The  $a$  and  $b$  here are not to be confused with operators of the optical mode and the mechanical oscillator—we shall always explicitly include the argument  $(x)$  for these continuum operators.] We further define

$$\hat{j}(x) \equiv \begin{cases} \hat{j}_-(x), & x < 0, \\ \hat{j}_+(x), & x > 0, \end{cases} \quad (4.48)$$

and

$$\hat{k}(x) \equiv \begin{cases} \hat{k}_-(x), & x < 0, \\ \hat{k}_+(x), & x > 0. \end{cases} \quad (4.49)$$

Furthermore, for fields  $a$ ,  $b$ ,  $j$  and  $k$ , the transformation relations Ea. (4.44) also apply.

Now suppose at  $t = 0$ , we have a photon coming from the input (west) port with arbitrary wave

function  $F(x)$  [like in Eq. (4.17), here  $F(x) = 0$  for  $x > 0$ ]. The initial quantum state of the entire optomechanical system is

$$|\psi(0)\rangle = \int_{-\infty}^0 dx F(x) \hat{j}_-^\dagger(x) |0\rangle_\gamma \otimes |\phi_0\rangle_A. \quad (4.50)$$

Since we would like to investigate this state's evolution when the photon reaches the cavity, we covert into the north-east representation:

$$|\psi(0)\rangle = \frac{1}{\sqrt{2}} [|\psi_A(0)\rangle + |\psi_B(0)\rangle]. \quad (4.51)$$

Here we have defined

$$|\psi_A(0)\rangle = \int_{-\infty}^0 dx F(x) \hat{a}^\dagger(x) |0\rangle_\gamma \otimes |\phi_0\rangle_A \quad (4.52)$$

$$|\psi_B(0)\rangle = \int_{-\infty}^0 dx F(x) \hat{b}^\dagger(x) |0\rangle_\gamma \otimes |\phi_0\rangle_A \quad (4.53)$$

in which we have already taken Eqs. (4.46) and (4.47) into account.

Here  $|\psi_A(0)\rangle$  corresponds to the case in which the photon enters Cavity A with the movable mirror, and  $|\psi_B(0)\rangle$  the case in which the photon enters Cavity B with the fixed mirror. As time goes on, these two states evolve individually, and Eq. (4.51) remains true for  $t > 0$ . For the Cavity A component  $|\psi\rangle_A$ , we have [cf. Eq. (4.39)]

$$|\psi_A(t)\rangle = \int_0^{t-x} dt' g(t-x, t') e^{i\beta^2 \omega_m (t-x-t')} \hat{D}(\beta e^{-i\omega_m x}) \hat{D}(-\beta e^{i\omega_m (t'-t)}) \hat{a}^\dagger(x) |\Phi(t)\rangle \quad (4.54)$$

where we have defined

$$|\Phi(t)\rangle \equiv \hat{U}_m(t) |0\rangle_\gamma |\phi_0\rangle_A, \quad (4.55)$$

while for  $|\psi\rangle_B$ , we set  $\beta \rightarrow 0$  and obtain

$$|\psi_B(t)\rangle = e^{i\varphi} \int_0^{t-x} dt' g(t-x, t') \hat{b}^\dagger(x) |\Phi(t)\rangle. \quad (4.56)$$

#### 4.3.4 The Final State

In order to describe the quantum state seen by the photodetector, we map  $a$  and  $b$  into  $j$  and  $k$ , only keeping the  $k$  component. We further project onto the single-photon basis of  ${}_\gamma\langle 0|k(x)$ , assuming  $x = 0+$ , obtaining

$$|\psi(t)\rangle_m = \frac{1}{2} [|\psi_A(t)\rangle_m + e^{i\varphi} |\psi_B(t)\rangle_m] \quad (4.57)$$

with

$$|\psi_A(t)\rangle_m = \int_0^t dt' g(t, t') \hat{O}(t - t') |\phi_0(t)\rangle \quad (4.58)$$

$$|\psi_B(t)\rangle_m = \int_0^t dt' g(t, t') |\phi_0(t)\rangle \quad (4.59)$$

with

$$|\phi_0(t)\rangle \equiv \hat{U}_m(t) |\phi_0\rangle \quad (4.60)$$

and

$$\hat{O}(t) \equiv e^{i\beta^2 \omega_m t} \hat{D}(\beta) \hat{D}(-\beta e^{-i\omega_m t}), \quad (4.61)$$

in particular  $\hat{O}(0) = 1$ . In this way, we are using the same notation as Eq. (4.39), and we can use Sec. 4.2.3 for obtaining photo-detection probability density at each time  $t > 0$ , which is given by

$$p(t) = \frac{\| |\psi_A\rangle_m \|^2 + \| |\psi_B\rangle_m \|^2 + 2\text{Re}(e^{i\varphi} {}_m\langle \psi_A | \psi_B \rangle_m)}{4} \quad (4.62)$$

which, when adjusting values of  $\varphi$ , leads to an instantaneous visibility of [Cf. (4.43)]:

$$v(t) = \frac{2|{}_m\langle \psi_A | \psi_B \rangle_m|}{\| |\psi_A\rangle_m \|^2 + \| |\psi_B\rangle_m \|^2}. \quad (4.63)$$

It relies on how different  $\psi_A$  is from  $\psi_B$ , which indicates how much the movable mirror in Cavity A is capable of “learning” about the existence of the photon in Cavity A. At any instant, if  $\psi_A$  is proportional to  $\psi_B$  (differ by a phase), the state of the movable mirror does not change, and therefore we have a perfect visibility. By contrast, if the photon is able to transform the movable mirror into a state substantially different from its freely evolving state, e.g., the orthogonal state in the extreme case, then we will have a significantly reduced visibility.

Similar to Eq. (4.39), here  $\psi_A$  and  $\psi_B$  each has a promptly reflected part [which arises from the  $\delta$ -function part of  $g(t, t')$ ], and a part in which the photon enters the cavity [which arises from the exponential decay part of  $g(t, t')$ ]. It is the second part that contributes to the reduction of visibility.

### 4.3.5 Examples

We consider an experimental situation with the central frequency of the injecting photon tuned to the resonant frequency of the cavity, with a wave function of

$$F(x) = \sqrt{2\Gamma} e^{\Gamma x} \Theta(-x). \quad (4.64)$$

Here  $\Gamma$  measures the frequency-domain width of the photon. We further assume that the mechanical oscillator's eigenfrequency (when uncoupled with light) is equal to the cavity bandwidth, or  $\omega_m = \gamma$ . As in Ref. [7], we assume that the mechanical oscillator, i.e., the mirror, is initially prepared at its ground state:

$$|\phi_0\rangle = |0\rangle_A. \quad (4.65)$$

With these specializations, we have

$$|\psi_A(t)\rangle_m = C(t) [|0\rangle + \gamma|M(t)\rangle] \quad (4.66)$$

$$|\psi_A(t)\rangle_m = C(t) \left[ |0\rangle + \gamma \int_0^t dt' f(t-t')|0\rangle \right] \quad (4.67)$$

with

$$C(t) \equiv \sqrt{2\Gamma} e^{-(\Gamma+i\omega_m/2)t}, \quad f(t) \equiv e^{(\Gamma-\gamma/2)t} \quad (4.68)$$

and

$$|M(t)\rangle \equiv \int_0^t dt' f(t-t') e^{i\beta^2[\omega_m(t-t') - \sin \omega_m(t-t')]} \times \left| \beta - \beta e^{i\omega_m(t'-t)} \right\rangle. \quad (4.69)$$

By comparing with Sec. 4.3.4, we first find that visibility depends on the similarity between  $|M(t)\rangle$  and its counterpart in Eq. (4.67): when they are similar to each other (e.g., when  $\beta \lesssim 1$ ) or when they do not contribute significantly to  $|\psi_{A,B}(t)\rangle_m$ , the visibility will tend to be high. By contrast, in order to achieve a complete incoherence, we need  $|M(t)\rangle$  to contribute significantly, and nearly orthogonal to  $|0\rangle$ —and this *requires*  $\beta \gtrsim 1$ . The arrival probability density (4.62) and contrast defect (4.63) can be computed if we use

$$\langle 0|\beta\rangle = \langle 0|\hat{D}(\beta)|0\rangle = e^{-\beta^2/2}. \quad (4.70)$$

In Fig. 4.5, we plot maximum and minimum of the probability density in the left panels, and visibility in the right panels, both as functions of time. We have chosen  $\beta = 0.5$  for upper panels,  $\beta = 1.2$  for middle panels and  $\beta = 2$  for lower panels. In each panel, we have also shown curves with  $\Gamma = 0.2$  (red dotted),  $\Gamma = 1$  (blue dashed), and  $\Gamma = 2$  (solid black). As  $\beta$  increases (as we move from upper to lower panels), the photon's ponderomotive effect on the movable mirror increases, therefore the visibility is able to vary more. This means  $\beta \gtrsim 1$  is necessary (but not sufficient, see below) for visibility to substantially decay and then revive — a feature Ref. [7] has used to search for decoherence effects.

On the other hand, another condition for visibility to first decrease and then revive, and repeat

on, seems to be  $\Gamma \gtrsim 1$ , as also indicated by each of the right panels of Fig. 4.5. In addition, as  $\Gamma \gg 1$ , our result becomes comparable to Ref. [7]. Qualitatively, this is because for  $\Gamma \gg 1$ , if photon does arrive at a time around  $\sim 1$ , we can be sure the photon has interacted with the mirror—and we can roughly treat the photon as already within the cavity at  $t = 0$ .

Mathematically, for  $t \gg 1/\Gamma$ , the conditional quantum state of the mirror given photon detection at time  $t$  could be approximately written as:

$$|\psi\rangle_{\text{m}} = \frac{\gamma}{\sqrt{2\Gamma}} e^{-(\gamma+i\omega_m)t/2} \left[ e^{i\varphi}|0\rangle + e^{i\beta^2\omega_m t} \hat{D}(\beta) |-\beta e^{-i\omega_m t}\rangle \right]. \quad (4.71)$$

$$= \frac{\gamma}{\sqrt{2\Gamma}} e^{-(\gamma+i\omega_m)t/2} \left[ e^{i\varphi}|0\rangle + e^{i\beta^2(\omega_m t - \sin \omega_m t)} |\beta - \beta e^{-i\omega_m t}\rangle \right]. \quad (4.72)$$

This is consistent with results of Ref. [7].

However, in order for  $\Gamma \gg 1$  and to observe a revival of visibility, we have to wait till  $t \geq 2\pi$ . The probability for detecting the photon at such late times is exponentially small — as indicated by the left panels of Fig. 4.5 This means we may have to make a trade off between having a very sharp revival of visibility and being robust against loss and able to cumulate enough statistics within reasonable amount of time.

## 4.4 Conditional Quantum-state Preparation

In this section, we show how to engineer an arbitrary quantum state of the mechanical oscillator by injecting a single photon with specifically designed wave function and by post selecting the arrival time of the output photon. Note that unlike Refs. [10, 11], our state preparation procedure is conditional. This guarantees a pure quantum state for the mechanical oscillator, but requires a low decoherence rate and a high detection quantum efficiency for the outgoing photon.

### 4.4.1 The Configuration

The scheme is shown in Fig. 4.6. It is very similar to the single-photon interferometer discussed in the previous section, except that in the east arm we replace the cavity B with a perfectly reflected mirror B. In this case, most of the previous analysis are still valid: Eq. (4.57) to Eq. (4.59). The only difference is that the  $g(t, t')$  function in Eq. (4.59) needs to be replaced by  $\delta(t - t')$ , as we have a perfectly reflecting mirror instead of a cavity here, namely,

$$|\psi_B(t)\rangle_{\text{m}} = |\phi_0(t)\rangle. \quad (4.73)$$

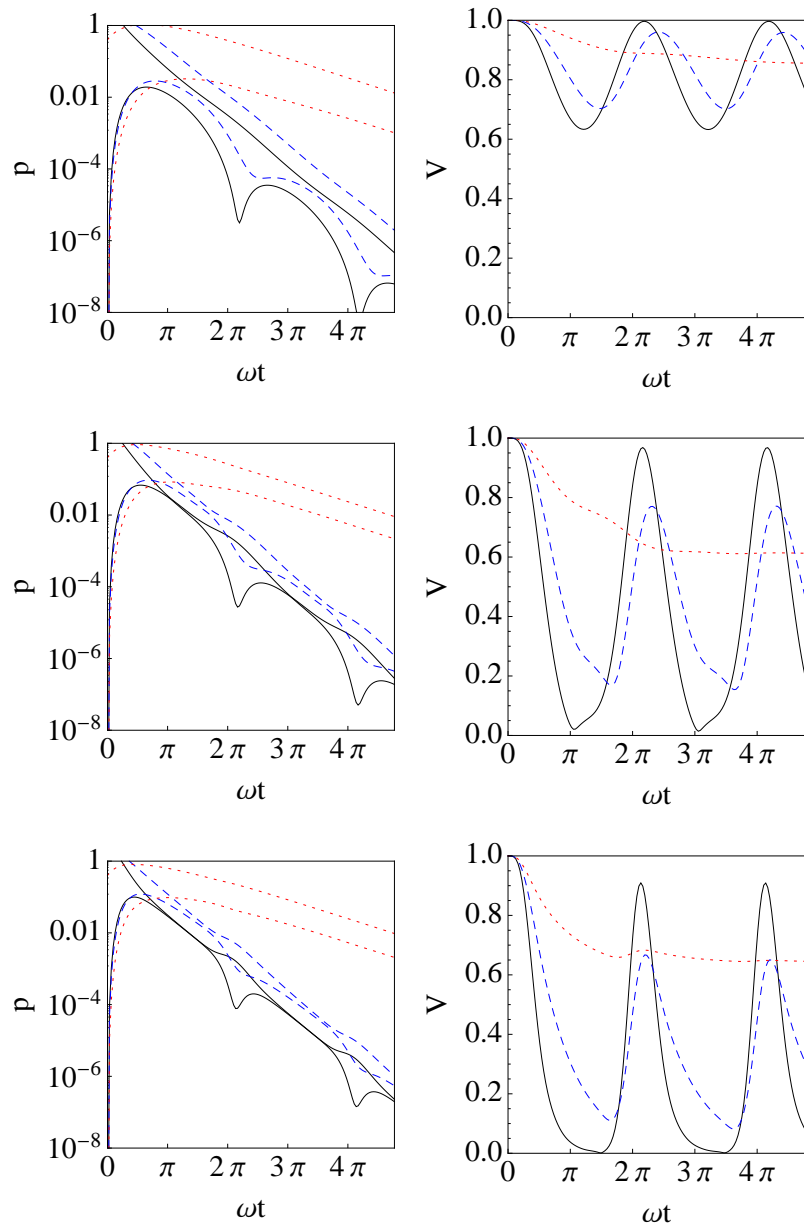


Figure 4.5: (color online) (left) Probability density and (right) fringe visibility for the photon to come out with different  $\beta$ : (Top-to-bottom: first row,  $\beta = 0.5$ ; second row,  $\beta = 1.2$ ; third row,  $\beta = 2$ ). For each  $\beta$ , three different values of  $\Gamma$  are considered for comparison:  $\Gamma = 0.2$  (red dotted), 1 (blue dashed), 2 (black solid). All the calculation assume  $\gamma = 1, \omega_m = 1$ . For probability density plot, the upper line of the same color is the maximum value of the probability density, the lower one is the minimum value.

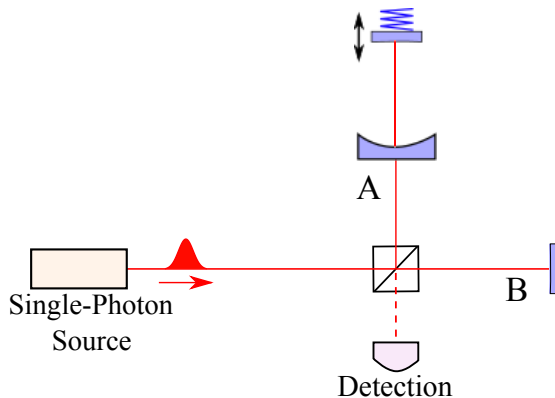


Figure 4.6: (color online) The sample device which uses single photon to prepare mechanical oscillator quantum state. Here the the detuning phase for the mirror on the east arm is adjusted such that the promptly reflected photon will come out from west port, with 0 probability coming out from south port.

To proceed, we further adjust the detuning phase  $\varphi$  in Eq. (4.57) such that at the dark port, the promptly reflected wave from the front mirror of cavity A exactly cancels the promptly reflected wave from the mirror B. In this case, having a photon emerging from our detection port (Fig. 4.6) automatically indicates that the photon has entered the cavity and interacted with the mirror; Eq. (4.57) or the conditional quantum state of the mechanical oscillator (unnormalized) is given by:

$$|\psi(t)\rangle_m = \frac{1}{2} \int_0^t dt' g_p(t, t') \hat{O}(t - t') |\phi_0(t')\rangle \quad (4.74)$$

with

$$g_p(t, t') = \gamma e^{-\gamma/2(t-t')} F(-t'). \quad (4.75)$$

As  $g_p(t, t')$  is related to the input photon wave function  $F(x)$ , by modifying input photon wave function, we can therefore engineer the conditioning mechanical oscillator quantum state  $|\psi(t)\rangle_m$ . Even if there is a finite probability that the photon will come out through the west arm or the bright port, once we detect a photon at time  $t$  at the dark port, we know that it must come from arm A and it also has stayed in the cavity A for a certain amount of time.

#### 4.4.2 Preparation of a Single Displaced-Fock State

First of all, we notice that when different in-coming photon wave function  $F$ 's are used, if we keep conditioning over the *same* photon arrival time  $t$ , the conditional quantum states we obtain for the mechanical oscillator will depend linearly on  $F$ . In other words, if  $F_1$  allows us to prepare  $|\phi_1\rangle$ , and  $F_2$  allows us to prepare  $|\phi_2\rangle$ , then injecting a new photon with a superimposed wavefunction  $F = \alpha_1 F_1 + \alpha_2 F_2$  will allow us to prepare  $\alpha_1 |\phi_1\rangle + \alpha_2 |\phi_2\rangle$ .

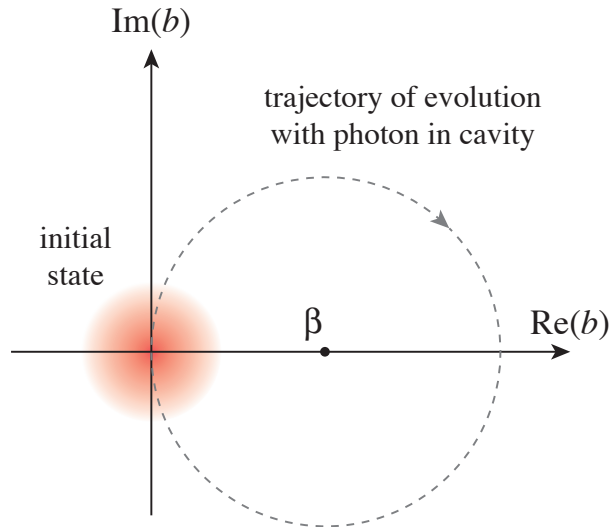


Figure 4.7: A sketch of the phase-space trajectory of the mechanical oscillator. The Wigner function of the initial state  $|0\rangle$  is represented by the shaded disk, the dot marked with  $\beta$  on the real axis is the new equilibrium position of the oscillator when the photon is in the cavity, while the dashed circle is the trajectory of the oscillator's Wigner function when the photon is inside the cavity. Detection of the out-going photon at  $t = 2n\pi/\omega_m$  corresponds to superimposing all mechanical-oscillator quantum states along the dashed trajectory, weighted by the photon's wave function.

This means we only need to show how members of a complete basis can be prepared, and we choose this to be

$$|\psi(t)\rangle_m = |\tilde{n}\rangle = \hat{D}(\beta)|n\rangle, \quad n = 0, 1, 2, \dots \quad (4.76)$$

These displaced Fock states are simply Fock states of the oscillator when the photon is inside the cavity, see Eq. (4.34).

Let us assume that the mechanical oscillator is initially prepared at its ground state. Before studying preparation of an arbitrary conditional quantum state for the mechanical oscillator, we first show that we can prepare a conditional state with an arbitrary quantum number  $n$ , by injecting a photon with the following wave function:

$$F(x) = \sqrt{\gamma} e^{(\gamma/2 - i\beta^2\omega_m + in\omega_m)x} \Theta(-x). \quad (4.77)$$

As we plug Eq.(4.77) into Eq.(4.74) we obtain the conditional quantum state of

$$|\psi(t)\rangle_m = \frac{\hat{D}(\beta)\gamma^{3/2}e^{-\frac{\gamma}{2}t + i\beta^2\tau}}{2\omega_m} \int_0^\tau d\tau' e^{-in\tau'} |-\beta e^{i(\tau' - \tau)}\rangle \quad (4.78)$$

with  $\tau \equiv \omega t$ . This is a coherent superposition coherent states, which in the complex amplitude domain all line up in a circle with radius  $\beta$  around the center located at complex amplitude equal

to  $\beta$ ; these states are parametrized mathematically by  $\hat{D}(\beta)|-\beta e^{i\phi}\rangle$ . These states are superposed with the same magnitude, but different phases, due to the decay rate of  $\gamma/2$  in the  $F$  chosen by Eq. (4.77). Obtaining such a state is understandable, as given the photon detection at  $t$ , the actually time  $t'$  for the photon staying inside the cavity is uncertain, and we have to sum up all the possible contributions from 0 to  $t$ . This situation is illustrated in Fig. 4.7.

One important feature in the above expression is that the integrand is a periodic function. If we denote

$$\tau \equiv \omega_m t = 2\pi N + \Delta\phi, \quad (4.79)$$

where  $N$  is some integer and  $\Delta\phi$  is the residual phase ranging from 0 to  $2\pi$ . In this way, the integral in Eq. (4.78) then becomes

$$\left[ N \int_0^{2\pi} + \int_0^{\Delta\phi} \right] d\phi e^{-in\phi} |-\beta e^{i\phi}\rangle. \quad (4.80)$$

In the limit of  $N \gg 1$ , when the photon arrives at the photodetector with a delay large compared to the oscillator's oscillation period, the first term in Eq. (4.80) always dominates. This means we obtain the same conditional state if we restrict  $\tau$  around an integer multiple of  $2\pi$ , or make sure it is large enough. This leads to the interesting effect that in the asymptotic limit of  $\tau \rightarrow +\infty$ , the conditional state will be independent from  $\tau$ . In practice, however, although the integral (4.80) increases with  $N$ , the exponential decay factor in Eq. (4.78) always favors simply choosing  $N = 1$ . It is straightforward to evaluate this conditional state; using

$$\int_0^{2\pi} d\phi e^{-in\phi} e^{i\phi \hat{a}^\dagger} |0\rangle = \frac{1}{n!} (\hat{a}^\dagger)^n |0\rangle, \quad (4.81)$$

we have

$$\begin{aligned} \int_0^{2\pi} d\phi e^{-in\phi} |-\beta e^{i\phi}\rangle &= \frac{2\pi (-\beta)^n e^{-\frac{\beta^2}{2}}}{\sqrt{n!}} |n\rangle \\ &= 2\pi |n\rangle \langle n | -\beta \rangle, \end{aligned} \quad (4.82)$$

which means

$$|\psi\rangle_{\text{m}} = \frac{\pi \gamma^{3/2} e^{-\frac{\pi\gamma}{\omega_m}} e^{2\pi i \beta^2}}{\omega_m} \frac{(-\beta)^n e^{-\frac{\beta^2}{2}}}{\sqrt{n!}} |\tilde{n}\rangle. \quad (4.83)$$

This is indeed proportional to  $|\tilde{n}\rangle$ , as promised. Here we have used

$$\langle -\beta | n \rangle = \frac{(-\beta)^n e^{-\beta^2/2}}{\sqrt{n!}}. \quad (4.84)$$

Since the probability for the returning photon to arrive at precisely  $2\pi/\omega_m$  is zero, we must allow an interval around this target, which on the one hand provides us with a nonzero probability, but on the other hand makes the conditional state imprecise. If we require the actual conditional state

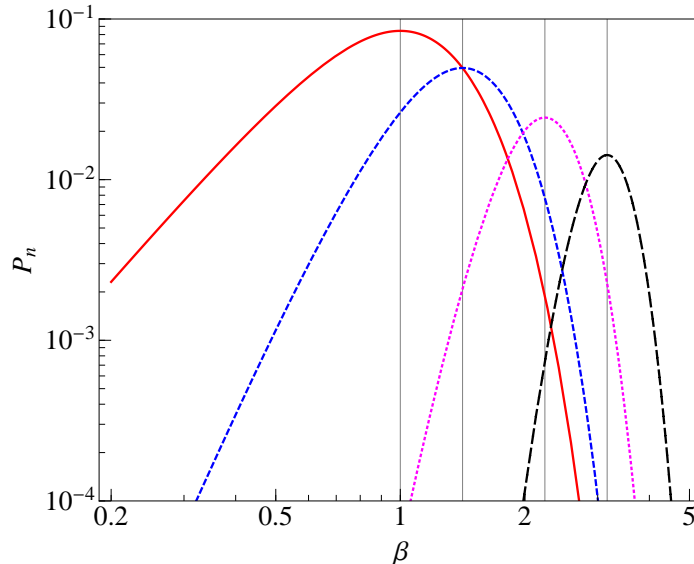


Figure 4.8: Probability for obtaining displaced Fock states  $|\tilde{1}\rangle$  (red solid),  $|\tilde{2}\rangle$  (blue dashed),  $|\tilde{5}\rangle$  (magenta dotted) and  $|\tilde{10}\rangle$  (black dash-dotted), a range of  $\beta$  and minimum state overlap of  $1 - \epsilon$ . Vertical gridlines are drawn for  $\beta = 1, \sqrt{2}, \sqrt{5}$  and  $\sqrt{10}$ ; these are the locations where maxima of  $P_{1,2,5,10}$  are reached.

to have a high overlap with the target state (or high fidelity),

$$\frac{|\langle \psi | \tilde{n} \rangle|}{\sqrt{\langle \psi | \psi \rangle}} \geq 1 - \epsilon \quad (4.85)$$

then, by perturbing the integration upper bound of Eq. (4.82), we obtain the following requirement on the allowed photon arrival time

$$|\tau - 2\pi| \leq \Delta\tau \equiv \sqrt{8\pi^2\epsilon} \frac{|\langle -\beta | n \rangle|}{\sqrt{1 - |\langle -\beta | n \rangle|^2}}, \quad (4.86)$$

which, for each trial of the experiment, would happen with a probability of

$$\begin{aligned} P &= |\langle \psi | \psi \rangle|^2 \frac{2\Delta\tau}{\omega_m} \\ &= 2\sqrt{8\epsilon} \left( \frac{\pi\gamma}{\omega_m} \right)^3 e^{-\frac{2\pi\gamma}{\omega_m}} \frac{|\langle -\beta | n \rangle|^3}{\sqrt{1 - |\langle -\beta | n \rangle|^2}}. \end{aligned} \quad (4.87)$$

And this would be the probability with which we can create a conditional state with overlap at least  $1 - \epsilon$  with the target.

From Eq. (4.87), we further notice that we should fix

$$\gamma/\omega_m = 3/(2\pi) \quad (4.88)$$

in order to obtain a maximized success probability of

$$P_n = \sqrt{8\epsilon} \frac{27}{4e^3} \frac{|\langle -\beta|n\rangle|^3}{\sqrt{1 - |\langle -\beta|n\rangle|^2}}. \quad (4.89)$$

For each  $n$ , the maximum of  $P_n$  is reached at  $\beta = \sqrt{n}$ . In Fig. 4.9, we plot  $P_n$  for a range of  $\beta$ , for  $\epsilon = 0.1$ , or a state overlap of  $\geq 90\%$ . We can see that the probability of producing  $|\tilde{n}\rangle$  decreases rather quickly as  $n$  increases.

This dependence (4.89) on  $\beta$  comes from two sources, which we can understand better by going to the phase-space reference frame centered at the equilibrium position of the oscillator when the photon is inside the cavity. In this reference frame, the complex amplitude of the coherent states being superimposed are located on a circle with distance  $\beta$  away from the center, while the target we would like to prepare is simply the Fock state  $|n\rangle$ . Although the photon's wave function selects out an oscillator state proportional to  $|n\rangle$ , this post-selection does not improve the intrinsic overlap between all those that participate the superposition, which is actually proportional to

$$|\langle -\beta e^{i\phi}|n\rangle|^2 = |\langle -\beta|n\rangle|^2. \quad (4.90)$$

This explains the dependence of  ${}_m\langle\psi|\psi\rangle_m$  on beta. The other factor of dependence on  $\beta$  is that when the target state has a very low overlap with the individual members  $|\beta e^{i\phi}\rangle$  of the superposition, the requirement on the accuracy of photon arrival time, or  $\Delta\tau$ , increases, as shown in Eq. (4.86).

### 4.4.3 Preparation of an Arbitrary State

Since the displaced number states forms a complete basis we can expand any target state as

$$|\psi_{\text{tg}}\rangle = \sum_{n=0}^{+\infty} c_n |\tilde{n}\rangle, \quad \sum_{n=0}^{+\infty} |c_n|^2 = 1. \quad (4.91)$$

Since a linear combination of  $F$ s leads to a linear combination of conditional states, we simply need to apply the result of the last subsection and have

$$F(x) = \frac{\sqrt{\gamma} e^{(\gamma/2 - i\beta^2\omega_m)x}}{Z} \sum_{n=0}^{+\infty} \tilde{c}_n e^{in\omega_m x} \quad (4.92)$$

with

$$Z \equiv \left[ \sum_{j,k=0}^{+\infty} \frac{\tilde{c}_j \tilde{c}_k^*}{1 + i(j-k)\frac{\omega_m}{\gamma}} \right]^{1/2}, \quad (4.93)$$

$$\tilde{c}_n \equiv \frac{c_n}{\langle -\beta|n\rangle} = \sqrt{n!} (-\beta)^n e^{\beta^2/2} c_n. \quad (4.94)$$

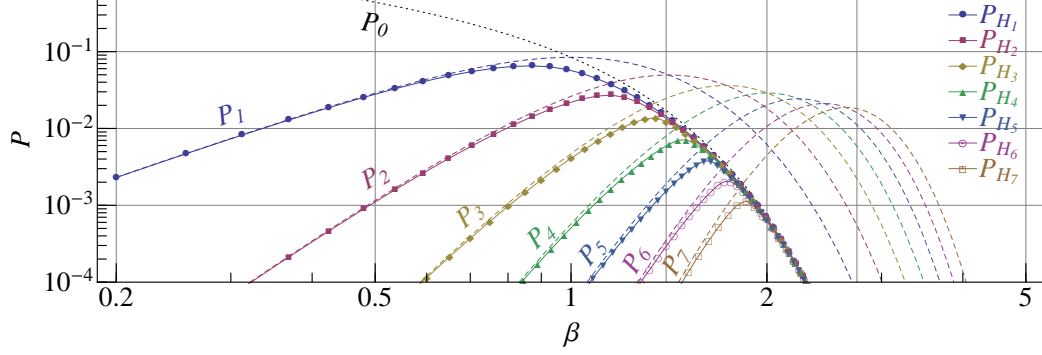


Figure 4.9: Minimum success probability for states in Hilbert spaces  $\mathcal{H}_{1,2,\dots,7}$  (solid curves with markers), together with success probability for producing single displaced Fock states,  $P_{0,1,2,\dots,7}$  (dashed curves without markers). Fidelity is fixed at 10%. Note that  $P_0$  would become greater than 1 at low values of  $\beta$ —but in this case our approximation in obtaining  $\Delta\tau$  breaks down.

This is an additional periodic modulation (with period  $2\pi/\omega_m$ ) of the photon's wave function. We caution that in order for the summation in Eq. (4.92) to converge, if  $c_n$  does not go to zero for all  $n \geq N$ , then it must decay very fast when  $n \rightarrow +\infty$ , due to the presence of the  $\sqrt{n!}$  factor (which grows faster than  $\beta^{-n}$ ).

As in the previous subsection, we obtain the conditional state at  $\tau \equiv \omega_m t = 2\pi, 4\pi, \dots$ , as well as any  $\tau$  that is substantially large. Again, let us consider  $\tau = 2\pi$ , this gives the conditional state of

$$|\psi\rangle_m = \frac{\pi\gamma^{3/2} e^{-\frac{\pi\gamma}{\omega_m}} e^{2\pi i\beta^2}}{\omega_m Z} |\psi_{\text{tg}}\rangle. \quad (4.95)$$

We can use the same approach as the previous subsection to evaluate the probability with which this conditional state is achieved with a high overlap. For a minimum overlap of  $1 - \epsilon$ , we require

$$|2\pi - \tau| \leq \Delta\tau = \frac{\sqrt{8\pi\epsilon}}{\left| \sum_{m=0}^{+\infty} \tilde{c}_m \right| \sqrt{1 - |\langle -\beta | \psi_{\text{tg}} \rangle|^2}}. \quad (4.96)$$

Note that this  $\Delta\tau$  diverges if  $\sum_{m=0}^{+\infty} \tilde{c}_m = 0$ , because in this case the overlap does not vary at  $O[(\tau - 2\pi)^2]$  order. Assuming the target state to be generic, then the probability for obtaining this state is then

$$P_{|\psi\rangle} = 2\sqrt{8\epsilon} \frac{\left(\frac{\pi\gamma}{\omega_m}\right)^3 e^{-\frac{2\pi\gamma}{\omega_m}} \left[1 - \left|\sum_{n=0}^{+\infty} \langle -\beta | n \rangle^2 \tilde{c}_n\right|^2\right]^{-1/2}}{\left|\sum_{m=0}^{+\infty} \tilde{c}_m\right| \sum_{j,k=0}^{+\infty} \frac{\tilde{c}_j \tilde{c}_k^*}{1 + i \frac{(j-k)\omega_m}{\gamma}}}. \quad (4.97)$$

Here the choice of  $\gamma/\omega_m$  depends on the target quantum state, but if we assume this dependence is

weaker than the pre-factor, and continue to use Eq. (4.88), then we obtain

$$P_{|\psi\rangle} = \frac{27}{e^3} \sqrt{\frac{\epsilon}{2}} \frac{\left[1 - \left|\sum_{n=0}^{+\infty} \langle -\beta|n\rangle^2 \tilde{c}_n\right|^2\right]^{-1/2}}{\left|\sum_{m=0}^{+\infty} \tilde{c}_m\right| \sum_{j,k=0}^{+\infty} \frac{\tilde{c}_j \tilde{c}_k^*}{1 + \frac{2\pi i(j-k)}{3}}}. \quad (4.98)$$

As it turns out,  $P_{|\psi\rangle}$  depends on the detail of  $|\psi\rangle$ —even if we only try to create a combination of  $|\tilde{0}\rangle$  and  $|\tilde{1}\rangle$ , the combination coefficients would lead to very different success probabilities. In order to provide a concrete measure of the ability of our state-preparation scheme, we have chosen to compute the minimum success probabilities of creating all the states in the mechanical oscillator’s Hilbert subspaces spanned by the lowest displaced Fock states, e.g.,  $\mathcal{H}_1 \equiv \text{Sp}\{|\tilde{0}\rangle, |\tilde{1}\rangle\}$ ,  $\mathcal{H}_2 \equiv \text{Sp}\{|\tilde{0}\rangle, |\tilde{1}\rangle, |\tilde{2}\rangle\}$ , etc. We define

$$P_{\mathcal{H}_j} = \min_{|\psi\rangle \in \mathcal{H}_j} P_{|\psi\rangle}, \quad \mathcal{H}_j = \left\{ \sum_{l=0}^j \alpha_l |\tilde{l}\rangle : \alpha_l \in \mathbb{C} \right\}. \quad (4.99)$$

In Fig. 4.9, we plot  $P_{\mathcal{H}_1}, P_{\mathcal{H}_2}, \dots, P_{\mathcal{H}_7}$  as functions of  $\beta$  (in solid purple curves). Because  $\mathcal{H}_1 \subset \mathcal{H}_2 \subset \dots \subset \mathcal{H}_7$ , it is increasingly difficult to create all states in  $\mathcal{H}_j$  with higher values of  $j$ , and therefore  $P_{\mathcal{H}_1} \geq P_{\mathcal{H}_2} \geq \dots \geq P_{\mathcal{H}_7}$ , namely our success probability decreases globally when  $j$  increases. In fact, as we overlay the single-Fock-state success probabilities  $P_0, P_1, \dots, P_5$ , we also discover that for any  $P_{\mathcal{H}_j}(\beta)$ , it asymptotes to  $P_0$  at higher  $\beta$ , and to  $P_j$  at lower  $\beta$ ; moreover, the transition between these two asymptotic regions are brief, and the  $P_{\mathcal{H}_j}(\beta)$  curves do not lie much below the minimum of  $P_0$  and  $P_j$ .

This asymptotic behavior can be understood from the behavior of  $P_n$ , the success probability for single (displaced) Fock states. For smaller  $\beta$ , it is much more difficult to prepare a higher Fock state, therefore, if  $\beta$  is sufficiently small, the difficulty of preparing  $\mathcal{H}_j$  is dominated by the preparation of  $|\tilde{j}\rangle$ , the single most difficult state in the space to prepare—and therefore  $P_{\mathcal{H}_j}$  agrees with  $P_j$ . Vice versa, for sufficiently large  $\beta$ , the difficulty of preparing  $\mathcal{H}_j$  lies in the preparation of  $|\tilde{0}\rangle$ , and therefore  $P_{\mathcal{H}_j}$  would agree with  $P_0$ . The fast transition between the two extremes indicates that when trying to prepare states in  $\mathcal{H}_j$ , the difficulty either lies in  $|\tilde{0}\rangle$ , or in  $|\tilde{j}\rangle$ , and only for a small region of  $\beta$  the two difficulties might compete with each other—while none of the intermediate states contribute to the difficulty of state preparation. This is consistent with the relative locations of the  $P_n$  curves in Fig. 4.9: (i) for any  $\beta$ ,  $P_{1,2,\dots,j-1}$  are always much greater than the minimum of  $P_0$  and  $P_j$ , and (ii) as we move away from the  $\beta$  at which  $P_0$  and  $P_j$  crosses each other, their discrepancy increases quickly.

As a matter of practicality, we see that if we choose  $\beta \approx 0.87$  the probability of achieving, with an overlap (or fidelity) above 90%, any superposition of  $|\tilde{0}\rangle$  and  $|\tilde{1}\rangle$  (i.e., any member of the subspace  $\mathcal{H}_1$ ) is guaranteed to be above 6.3%. On the other end, with a probability of at least 0.1%, we can

produce all states in the 8-dimensional subspace of  $\mathcal{H}_7$ .

## 4.5 Practical Considerations

In order to realize such a state-preparation scheme, we need to fulfill the following three requirements. The *first* requirement is that the series in Eq. (4.92) be converging. This can be satisfied if  $\beta \geq 1$ . To see what this means, we restore all the physical units:

$$\beta = \frac{k/(2\omega_m)}{\sqrt{\hbar m \omega_m/2}} = \left[ \frac{\hbar \omega_0}{c} \right] \sqrt{\frac{2}{\hbar m \omega_m}} \left[ 2\omega_m \frac{L}{c} \right]^{-1}. \quad (4.100)$$

It characterizes the momentum kick of photon  $\hbar \omega_0/c$  to the oscillator during one oscillation period compared to the ground-state momentum uncertainty  $\sqrt{\hbar m \omega_m/2}$ . The momentum kick from the photon needs to be big enough to substantially change the mirror state. The *second* requirement is that cavity bandwidth be smaller than the mechanical frequency

$$\gamma < \omega_m. \quad (4.101)$$

This is because we need to wait at least several oscillation periods to approach the asymptotic state, and the photon should be long enough such that we have a finite probability for detecting photon at  $t > \omega_m^{-1}$ .

Combining the above two conditions, we obtain the following relation

$$\frac{\lambda}{\mathcal{F}} < \sqrt{\frac{\hbar}{2m\omega_m}} \quad (4.102)$$

where  $\lambda$  is the optical wavelength of the photon,  $\mathcal{F}$  is the cavity finesse. This means the cavity linear dynamical range must be less than the zero point uncertainty to realize the optomechanical nonlinearity. An alternative scheme has been proposed to make it more achievable experimentally [16].

The *third* requirement is that the thermal decoherence effect be small within one mechanical oscillation period, namely [cf. also Eq. (5) in Ref. [7]]:

$$Q > \frac{kT_E}{\hbar\omega_m}, \quad (4.103)$$

where  $Q$  is the mechanical quality factor of the oscillator and  $T_E$  is the environmental temperature. These three requirements can be achieved experimentally, e.g., the current setups shown in Refs. [3, 4] and the one proposed in Ref. [6].

Finally, we require the capability of generating a single photon with an arbitrary wave

function with duration comparable to the mechanical oscillation frequency of the photon. This is possible with cavity QED systems, as has been discussed by Ref. [17–19].

## 4.6 Conclusions

We have presented an exact solution to the open quantum dynamics of an single-photon interferometer with a movable mirror. Since the photon number is preserved, we have been able to write the total wave function of photon as three components: incoming photon, inside-cavity photon and out-going photon. We analyzed the details of how the photon exchanges between the cavity mode and the external continuous field.

We studied the fringe visibility of the interferometer in a specific case by injecting a single photon with exponentially decaying profile and with the movable mirror initially prepared at the ground state. This scheme has been proposed by Ref. [7] to explore decoherence of a macroscopic oscillator, although in that proposal the photon has been assumed to start off from inside the cavity. In the limit when the photon pulse is short (or  $a \gg \gamma$ ), we did recover the result of Ref. [7], although our result deviates significantly when  $a$  becomes comparable to  $\gamma$ . We believe this is experimentally relevant, because in the case  $a \gg \gamma$ , the probability for the photon to exit from the detection port is very small, and therefore the experiment may suffer significantly from imperfections.

We have also studied the use of such nonlinear optomechanical interactions to prepare the mechanical oscillator into an arbitrary quantum state—similar to the proposal of Ref. [12], although not having to require that the photon to start off from within the cavity. To realize this, we require that: (i) the optomechanical cavity must be working in the nonlinearity regime [i.e., the cavity’s spatial line width must be less than the oscillator’s zero-point position fluctuation, see discussions above Eq. (4.102)], (ii) the cavity’s frequency width must be less than the mechanical oscillator’s angular frequency, (iii) the thermal decoherence time must be less than several times the mirror’s period of oscillation, and (iv) we must be able to engineer the single-photon wave function arbitrarily, at a time scale comparable to the mirror’s oscillation period and with coherence time longer than the cavity storage time. Although we have shown mathematically that all quantum states whose expansion coefficients in the displaced Fock states  $|\tilde{n}\rangle$  drop sufficiently fast as  $n \rightarrow +\infty$  can be prepared by modulating the wave function of the incoming photon and conditioning over the arrival time of the returning photon, in practice we will be confined to the superposition of a handful of nearby displaced Fock states.

## Bibliography

- [1] Review articles by T. J. Kippenberg, and K. J. Vahala, *Science* **321**, 1172 (2008), and by F. Marquardt, and S. M. Girvin, *Physics* **2**, 40 (2009).
- [2] A. D. O'Connell, M. Hofheinz, M. Ansmann, R. C. Bialczak, M. Lenander, E. Lucero, M. Neeley, D. Sank, H. Wang, M. Weides, J. Wenner, John M. Martinis, and A. N. Cleland, *Nature* **464**, 697 (2010).
- [3] J. D. Teufel, T. Donner, Dale Li, J. W. Harlow, M. S. Allman, K. Cicak, A. J. Sirois, J. D. Whittaker, K. W. Lehnert, and R. W. Simmonds, *Nature* **475**, 359 (2011).
- [4] A. H. Safavi-Naeini, J. Chan, J. T. Hill, T. P. M. Alegre, A. Krause, and O. Painter, arXiv:1108.4680 [quant-ph].
- [5] S. Gupta, K.L. Moore, K.W. Murch, and D.M. Stamper-Kurn, *Phys. Rev. Lett.* **99**, 213601 (2007).
- [6] J.D. Thompson, B.M. Zwickl, A.M. Jayich, F. Marquardt, S.M. Girvin and J.G.E. Harris, *Nature* **452**, 72 (2008).
- [7] W. Marshall, C. Simon, R. Penrose, and D. Bouwmeester, *Phys. Rev. Lett.* **91**, 130401 (2003).
- [8] D. Kleckner, I. Pikovski, E. Jeffrey, L. Ament, E. Eliel, J. Brink, and D. Bouwmeester, *New J. Phys.* **10**, 095020 (2008).
- [9] R. Penrose, *Gen. Rel. Grav.* **28** 581 (1996); *Phil. Trans. R. Soc. Lond. A* **356** 1927; *The Road to Reality: A Complete Guide to the Laws of the Universe*, Alfred A. Knopf, (2005).
- [10] P. Rabl, *Phys. Rev. Lett.* **107**, 063601 (2011).
- [11] A. Nunnenkamp, K. Børkje, and S. M. Girvin, *Phys. Rev. Lett.* **107**, 063602 (2011).
- [12] S. Bose, K. Jacobs, and P. L. Knight, *Phys. Rev. A* **56**, 4175 (1997).
- [13] A. Bassi, E. Ippoliti, S. L. Adler, *Phys. Rev. Lett.* **94**, 030401 (2005).
- [14] U. Akram, N. Kiesel, M. Aspelmeyer and G. J. Milburn., *New J. Phys.* **12**, 083030 (2010).
- [15] A. Nunnenkamp, K. Børkje, J. G. E. Harris, and S. M. Girvin, *Phys. Rev. A* **82**, 021806 (2010).
- [16] F. Y. Khalili, S. Danilishin, H. Miao, H. Muller-Ebhardt, H. Yang, and Y. Chen, *Phys. Rev. Lett.* **105**, 070403 (2010).
- [17] C. K. Law, and H. J. Kimble, *Journal of Modern Optics*, **44**, 2067 (1997).

- [18] J. McKeever, A. Boca, A. D. Boozer, R. Miller, J. R. Buck, A. Kuzmich, and H. J. Kimble, *Science* **303**, 1992 (2004).
- [19] M. Keller, B. Lange, K. Hayasaka, W. Lange, and H. Walther, *Nature (London)* **431**, 1075 (2004).